

CARDIFF UNIVERSITY

High Power Semiconductor Lasers

by

Stella N. Elliott

A thesis submitted in partial fulfilment for the
degree of Doctor of Philosophy

in the
School of Physics and Astronomy

May 2010

UMI Number: U516897

All rights reserved

INFORMATION TO ALL USERS

The quality of this reproduction is dependent upon the quality of the copy submitted.

In the unlikely event that the author did not send a complete manuscript and there are missing pages, these will be noted. Also, if material had to be removed, a note will indicate the deletion.



UMI U516897

Published by ProQuest LLC 2013. Copyright in the Dissertation held by the Author.
Microform Edition © ProQuest LLC.

All rights reserved. This work is protected against
unauthorized copying under Title 17, United States Code.



ProQuest LLC
789 East Eisenhower Parkway
P.O. Box 1346
Ann Arbor, MI 48106-1346

DECLARATION

This work has not previously been accepted in substance for any degree and is not concurrently submitted in candidature for any degree.

Signed *Stella Fleet* (candidate) Date .. *28 May 2010*

STATEMENT 1

This thesis is being submitted in partial fulfillment of the requirements for the degree of (insert MCh, MD, MPhil, PhD etc, as appropriate)

Signed *Stella Fleet* (candidate) Date *28 May 2010*

STATEMENT 2

This thesis is the result of my own independent work/investigation, except where otherwise stated. Other sources are acknowledged by explicit references.

Signed *Stella Fleet* (candidate) Date .. *28 May 2010*

STATEMENT 3

I hereby give consent for my thesis, if accepted, to be available for photocopying and for inter-library loan, and for the title and summary to be made available to outside organisations.

Signed *Stella Fleet* (candidate) Date .. *28 May 2010*

Summary of thesis

High power semiconductor lasers

Stella Elliott 28 May 2010

In this work I have investigated ways of improving the delivery of power from a semiconductor laser. Using red and near infra-red emitting quantum well and quantum dot based devices I have modelled the nearfield and farfield intensities and distribution in various waveguide structures. I explored their effects on the on both the coupling efficiency of the beam into applications and the propensity of the design to undergo catastrophic optical mirror damage, a remaining limit to the achievement of high powers. A mode-expanded structure was confirmed by measurement to have both a narrow farfield and high confinement factor, leading to low threshold current, in contrast to other designs.

I compared the effect of various factors on the power density at catastrophic damage and found the greatest effect from the current pulse length and dot or well nature of the active region, for the first time in the AlGaInP material system. At short pulse length the quantum dot devices did not fail by mirror damage, achieving higher powers than quantum well lasers, and then proved by electron microscopy and photocurrent spectroscopy to have failed by a different process.

I observed the loss of optical power at catastrophic optical mirror damage in real time, applying single, very high current pulses, observing differences in the behaviour of quantum dot, which showed little or no facet damage, and quantum well devices, which showed large amounts of damage, with a resolution of tens of nanoseconds compared to microseconds in the literature. I proposed an explanation for the time taken for the power level to drop in terms of the energy required to melt the observed quantity of damaged material.

There must be a beginning of any great matter, but the
continuing unto the end until it be thoroughly finished yields the
true glory

(Letter from Sir Francis Drake to Sir Francis Walsingham, from
off Cape Sagres, Portugal, 17 May 1587)

I would like to express my thanks to the many people, too numerous to mention, who helped me achieve this step. In particular I would like to thank my supervisor, Prof. Peter Smowton, who provided exactly the right advice at the right time to encourage or restrain my efforts. I am grateful in particular, that he made it possible for me to continue the process during a period of illness, when the options on offer would probably have prevented any further progress.

I am privileged to have met Dr Jens Tomm, and had the opportunity to work with his excellent facilities and wonderfully friendly colleagues and staff at Max-Born-Institut, Berlin, and Dr Ute Zeimer at Ferdinand-Braun-Institut. Jens' experience and insights into my field of work and friendly encouragement with my ideas have been most valued.

None of this work would have been possible without countless devices, most of which were destined for immediate death, fabricated, not only by Karen Barnett, but by the skills of Dr Gareth Edwards and Sam Shutts. Prof Peter Blood's advice on points of theory was invaluable. Many people in our warm and friendly group gave assistance.

Work of this type is not possible without the support of such people as Glyn Summers, whose excellent construction of pieces of equipment made certain results possible, Rhodri Baker, Steven Baker, who would provide a spectral source at a moments notice, Rob Tucker, whose pulse generators surpass all others, the prompt help of Malcolm Anderson and the computing support staff, the Office staff and all others whose background contribution is essential.

I would like to thank the tightly knit team of doctors and nurses in the National Health Service in Cardiff and their excellent treatment, which enabled me to continue my studies.

Friends and family made remaining sane possible, offering encouragement, advice and support. Finally, I must not forget my husband, Dr Martin Elliott, who, after encouraging me to start my PhD in the first place, has waited patiently for the long hours I have been in the lab and the weeks I have been away, and makes a good cup of tea!

Financial Assistance

I am most grateful for the financial assistance provided by EPSRC and IQE (Europe) Ltd in the form of an Industrial CASE studentship, and to IQE for providing the wafers on which a large part of this work was based. The European Union BRIGHTER project provided financial support for periods of work in Berlin.

Thanks

This thesis was produced using LaTeX

I would like to thank those who spend long hours producing free software and documentation to accompany it. Altruism is not dead!

Publications in refereed journals

1. S. N. Elliott, P. M. Smowton and G Berry, "Optimisation of high power AlGaInP laser diodes for optical storage applications" IEE Proceedings-Optoelectronics **153** pp 321-325 2006
2. S. N. Elliott, P. M. Smowton, M. Ziegler, J. W. Tomm, and U. Zeimer "Time resolved studies of catastrophic optical mirror damage in red-emitting laser diodes", J. of Appl. Phys., **107** 123116 (2010)
3. M. Ziegler, M. Hempel, H. E. Larsen, J. W. Tomm, P. E. Andersen, S. Clausen, S. N. Elliott, and T. Elsaesser, "Physical limits of semiconductor laser operation: A time-resolved analysis of catastrophic optical damage". Appl. Phys. Lett. **97**, 021110 (2010)

Publications in conference proceedings (non-refereed)

4. S. N. Elliott, P. M Smowton, G. T. Edwards, A.B. Krysa, and G. Berry, "Higher catastrophic optical mirror damage power density level at facet from quantum dot material" IEEE 21st International Semiconductor Laser Conference, 14-18 Sept 2008 (Conference digest) Pages:137 – 138
5. P. M. Smowton, M. Al-Ghamdi, S. N. Elliott, G. Edwards, P. Blood and A.B Krysa, "InP / AlGaInP short wavelength quantum dot lasers" IEEE 21st International Semiconductor Laser Conference, 14-18 Sept 2008 (Conference digest) Pages:31 - 32
6. S. N. Elliott, P. M. Smowton, G. T. Edwards, G. Berry and A. B. Krysa "Higher power density limit at COMD in GaInP/AlGaInP in quantum dots than in wells" Proc. SPIE, Vol. **7230**, 72300X (2009);

Presented talks

7. SIOE 2007, April 2-4, Cardiff, U.K. Stella N. Elliott, Peter M. Smowton and Graham Berry "Growth-variation-tolerant, mode-expanded AlGaInP laser diodes"
8. SIOE 2008, March31-April 2, Cardiff, U.K. Stella N. Elliott, Peter M. Smowton and Graham Berry "Catastrophic Optical Mirror Damage in AlGaInP laser diodes" SIOE 2008, March31-April 2, Cardiff, U.K.
9. UK Semiconductors 2008 Sheffield July 2, 3 Stella N. Elliott, Peter M. Smowton, Gareth T. Edwards, Andrey B. Krysa and Graham Berry "COMD in AlGaInP Quantum Well and Quantum Dot Laser Diodes"
10. ISLC Sept 2008 The 21st IEEE International Semiconductor Laser Conference 14-18 September 2008, Sorrento, Italy Stella N. Elliott, Peter M. Smowton, Gareth T. Edwards, Andrey B. Krysa, and Graham Berry, "Higher catastrophic optical mirror damage power density level at facet from quantum dot material"
11. Photonics West 24-29 January 2009 Novel In-Plane Semiconductor Lasers VIII Stella N. Elliott, Peter M. Smowton, and Gareth T. Edwards, Graham Berry and Andrey B. Krysa "Higher power density limit at COMD in GaInP/AlGaInP in quantum dots than in wells"
12. SIOE 2010, March 29-31, Cardiff, U.K. Stella N. Elliott, Peter M. Smowton, Mathias Ziegler and Jens W. Tomm "Time resolved studies of catastrophic optical mirror damage in red/NIR laser diodes"

Presented posters

13. SIOE 2006, March 10-12, Cardiff, U.K. Stella N. Elliott, Peter M. Smowton and Graham Berry "Improvement of high power AlGaInP laser diodes"
14. CMMP 2006, April 20 - 21, 2006, University of Exeter, UK. Stella N. Elliott, Peter M. Smowton and Graham "Optimization of high power AlGaInP laser diodes"
15. Photon 08: 26-29 August 2008 Edinburgh Conference Centre, Heriot-Watt University, UK Stella N. Elliott, Peter M. Smowton G Edwards, G. Berry and A. B. Krysa, "Comparison of catastrophic optical mirror damage in quantum dots and wells in GaInP/AlGaInP"

Contents

1	Introduction	1
1.1	Introduction	1
2	Theory and experimental details	4
2.1	Introduction and background to catastrophic optical mirror damage	4
2.2	Pulse length, conductivity and COMD power level	7
2.3	Sample preparation and characterisation of devices	8
2.3.1	Measuring current-voltage and light-current characteristics: IVLT	10
2.3.2	The farfield apparatus and measurements	11
2.3.3	Spectrometer	12
2.3.4	Power measurement with the integrating sphere	14
2.3.5	Measurements of voltage drops	14
2.4	Background theory for the multisection technique, facet temperature measurements and PC/EPVS	15
2.4.1	Stimulated emission, spontaneous emission and absorption	15
2.4.1.1	Occupation probabilities	16
2.4.1.2	The high energy Boltzmann tail of the spontaneous emission	17
2.5	The multisection technique: measurement of gain and absorption	18
2.6	Edge photovoltage, photocurrent and laser beam induced current measurements	19
2.6.1	Transition energies	20
2.6.2	EPVS	21
2.6.3	Factors affecting the size of the signal	21
2.6.4	Photocurrent and laser beam induced current	24
2.7	Facet temperature measurements	25
2.7.1	Contributions to facet temperature rise	26
2.8	Bandgap shift with heating	26
2.9	Theory and modelling of waveguides, nearfields and farfields	27
2.10	Amendments to standard technique in Berlin to measure the time to COMD	28
3	Design and properties of structures used	30
3.1	Introduction	30
3.2	Quantum well structures	32
3.3	Quantum dot structures	36
3.4	Performance of QW structures	37
3.4.1	Threshold current density as a function of temperature for Zn and Mg doped samples	37

3.4.2	Comparison of threshold characteristics of the mode expanded and standard DVD designs	38
3.4.3	Edge photovoltage spectroscopy (EPVS)	40
3.4.4	Farfield measurements	41
3.4.5	Summary of characterisation of the expanded mode design	42
3.5	Modelling of the stability of the mode expanded design	42
3.5.1	Large optical cavity - modelling a basic waveguide for optimal performance	42
3.5.2	Modelling of the narrow farfield and very narrow farfield mode expanded structures	45
3.6	Comparison of modelling and measurements of the mode expanded design . . .	49
3.7	Susceptibility to catastrophic optical mirror damage	57
3.8	Conclusions and other work	60
4	Catastrophic degradation: power density limits and mechanisms in QD and QW based devices	62
4.1	Introduction	62
4.2	The power density at the facet at catastrophic damage	64
4.2.1	Structures and devices used	64
4.2.2	Details of measurements	65
4.2.2.1	Average power over cycle	65
4.2.2.2	Accurate measurement of duty cycle to determine peak power	66
4.2.2.3	Area of beam at facet	67
4.2.3	Factors affecting the power density limit at COMD	69
4.3	Facet temperature rise	71
4.3.1	Measurement of facet temperature	71
4.3.2	Determination of bulk heating	75
4.3.3	Measurement of temperature from top window emission	81
4.4	Optical and electron microscopy of damaged devices	84
4.4.1	Optical microscopy of facets of devices taken to catastrophic optical damage	84
4.4.2	Electron microscopy	85
4.4.3	Cathodoluminescence	88
4.5	Photocurrent and LBIC measurements	89
4.5.1	Photocurrent studies on 1000 ns, single pulse devices	89
4.5.2	Photocurrent studies on aged devices	90
4.5.3	LBIC on single pulse devices	92
4.6	Discussion	92
4.6.1	Summary of evidence	92
4.6.2	The proposed explanation	96
4.6.3	Discussion	96
5	Time resolved studies of COMD in quantum well based devices	98
5.1	Introduction	98
5.2	Sample and experimental details	99
5.2.1	Choice of wafer	99
5.2.2	Device mounting and initial characterisation	99
5.2.3	Experimental setup for time resolved measurements	100

5.3	Experimental results - time to COMD and facet damage	101
5.3.1	Light pulses and time to COMD	101
5.3.2	Area of facet damage	102
5.4	Time to COMD: explanation in terms of a straightforward thermal model	104
5.4.1	The COMD process	104
5.4.2	Melting point curve	105
5.4.3	Comparison between COMD and a melting point curve	106
5.4.4	The model for the explanation of the limiting time to COMD	106
5.4.5	Calculation of time to COMD and comparison of calculated and measured values	106
5.5	Discussion of results and wider applicability	108
5.5.1	The COMD process	109
5.5.2	The thermal model	109
5.5.2.1	Estimate of volume	109
5.5.2.2	Values of specific heat and latent heat	112
5.5.2.3	Comparison of time to COMD behaviour for other devices	113
5.5.3	Wider applicability: other device dimensions, material systems	113
5.5.4	Increase of time resolution	114
5.6	Summary and conclusions	114
6	Summary, conclusions and suggestions for future work	116
6.1	Summary of main conclusions	116
6.2	Suggestions for future work	118
	Bibliography	119

Chapter 1

Introduction

1.1 Introduction

In this thesis I describe my investigations into high power semiconductor lasers, which offer significant advantages over solid state lasers in terms of cost, size and portability, and thus find many applications in medicine, industry and commerce.

Many aspects of laser performance have to be improved to increase the power available, including increasing efficiency and eliminating degradation and failure mechanisms and much has been achieved. Broad area single emitters have reached power levels of 16 W continuous-wave (cw), for a 1060 nm emitting quantum well laser with 74% conversion efficiency of electrical power in to laser power out (wallplug) [1]. Quantum dot lasers have also achieved high powers: 6 W cw in InAs-GaAs self-assembled structures with an efficiency of 58% [2]. The lasing wavelength in quantum dot based structures can be tuned by adjusting growth conditions and dot size. The structures have therefore potentially a much wider range of available wavelengths. Very low threshold current densities: 10.4 A/cm² [3] have been achieved. Higher power levels can be achieved by combining rows of single emitters into bars, giving 50 W from a 970 nm bar with 73% power conversion efficiency [4]. Stacking the bars can give 3.23 kW at a wavelength of 940 nm [5] in a unit weighing 29 kg.

One limit on powers achievable this way is set by the power supply and cooling system, which has to remove waste heat. With maximum efficiencies of about 75% achieved and kilowatts of power several hundred Watts must be dissipated. A bulky power supply and cooling system affect the portability although the device itself may be only half a millimetre wide by perhaps 4 mm long and one tenth of a millimeter thick.

As well as increasing the efficiency by such measures as reducing carrier leakage, nonradiative recombination and scattering loss [6], the amount of power that can be coupled into the application, via an optical fibre for example, can be increased by reducing beam divergence [5]. In a quantum well laser the waveguide is designed to confine the light to give a high intensity at the quantum wells. The result of this confinement is a beam that diverges widely in the direction perpendicular to the epitaxial layers, perhaps as much as forty-five degrees full width at half maximum intensity. Confinement of light parallel to the layers, a function of the type of device manufactured from the wafer, is always much less, typically less than ten degrees. The resulting highly astigmatic beam is technologically more difficult and expensive to use than a circular beam, requiring more expensive optics, for example. Ideally, the waveguide would be altered to reduce the beam divergence without reducing the confinement at the quantum wells, causing an increase in threshold current, which is a problem with many waveguide designs for a less divergent beam.

One aspect of my work deals with improvements in waveguide design to narrow the beam and make fuller use of the emitted power of the laser. Using a structure with *mode expansion* layers, a narrow farfield was achieved while maintaining a low threshold current, in contrast to some previous designs. I carried out exploratory modelling work on this design, and also characterised several growths of this wafer to assess the robustness of the design in a manufacturing environment.

When improvements in efficiency and output coupling have been gained, degradation, both long term and sudden, must be addressed. A laser mirror is susceptible to damage due to the surface properties (*dangling bonds*), intrinsically different to bulk properties, produced by cleaving, and can fail in a permanent and abrupt way by sustaining damage at the mirror: catastrophic optical mirror damage (COMD). Many processes can be used to prevent facet damage, including *passivation* of the surface for example with hydrogen or ZnS [7], the E2 process [8], various measures to prevent radiation being absorbed by the surface layer, such as *non-absorbing mirrors* (NAMs), produced by disordering or chemically changing the structure to increase the bandgap [9], or special contacts which prevent surface currents on the facet (*non-injection mirror* (NIM)) [10]. These processes require extra steps in the manufacture and can be time consuming and expensive and are often proprietary processes.

The second aspect of my work used the expanded mode design and several other structures in a study of the factors that affect the catastrophic damage power density limit, such as pulse length, spotsize and the nature of the active region. I then made measurements of facet temperature rise and used photocurrent and a range of microscopic techniques to explore the physical reasons for some of these differences.

The timescale of COMD has been thought to be of the order of hundreds of nanoseconds, but has not been directly observed on this timescale, instead being inferred from measurements on

the order of microseconds. I continued my investigation of COMD, observing the occurrence of COMD in real time on a timescale of tens of nanoseconds compared to the microsecond timescales in previous work described in the literature.

The main results are presented in Chapter 3, which deals with the results of modelling and characterisation of the narrow farfield structure and discusses details of structures used later, chapter 4, which presents a comparison of factors that affect the power density limit at the facet at COMD, including a comparison with structures with a quantum dot based active region and chapter 5, in which I present the results of the time resolved measurements.

In the next chapter I describe the process of catastrophic damage as described in the literature and present background theory for the experimental results, describing the apparatus and measurements made. Some of these techniques are standard procedures in the laboratory here but I designed and assembled some additional equipment, which I describe more fully.

In the final chapter I summarise my main results and make suggestions for future work.

Chapter 2

Theory and experimental details

2.1 Introduction and background to catastrophic optical mirror damage

If the power output of a laser is measured at constant current, or, alternatively, the current required to maintain a given power output is monitored, it will be found that the power decreases (or the current increases) with time. This degradation of performance can be temporary due to temperature increase (thermal rollover) or permanent. Permanent damage can take place on a long or medium timescale [11] or occur suddenly, in catastrophic optical mirror damage (COMD).

The generally accepted sequence of events during COMD involves [12–16] non-radiative recombination of carriers at the facet causing heating and reduction of the band gap of the facet material, followed by the reabsorption of optical power [17] which causes the temperature to rise relatively slowly up to a critical temperature rise measured at the facet [18] of 120-140 K. At this point thermal runaway occurs, the temperature rises on a timescale of the order of nanoseconds [12] to the melting point. Thermal runaway has not been directly observed as no experimental methods exist to measure facet temperatures on this short timescale. Temperatures have been measured using various techniques, but values averaged over the time and spatial area of the measurement are found and peak values must be inferred [19]. The temperature rise has been extensively modelled. Henry and co-workers [12] used an analytical method [20] for a temperature rise in a 1-D semi-infinite medium, with a characteristic temperature of 21.4 K governing the exponential rise in the absorption coefficient of the material at the facet. The value of 21.4 K is sometimes quoted as the critical temperature rise [16]. (Much further modelling has used analytical or numerical methods to extend the analysis to a 3-D multilayer situation [21–23], but will not be discussed here.) So that measures can be taken to reduce facet heating and increase laser lifetime, identification of the heating mechanism is important and there

are many possible mechanisms and ways of preventing them. A cleaved surface disrupts the distribution of electrons around the atoms, giving rise to *dangling bonds*, which occur at such high densities they form a band in the middle of the band gap [24]. Recombination due to this mechanism and due to oxidation or other defects on the surface can be prevented by passivation and coating of the facet [7]. Reabsorption can be reduced by the use of non-absorbing mirrors [9]. Another potential contribution is thought to be due to surface currents on the facet. Special contacts that leave an uncontacted and therefore unpumped margin between the top contact and the facet have been found to reduce the rate of temperature rise at the facet in InGaAs/AlGaAs lasers, but did not materially change the power level at COMD [25]. The same study compared similarly performing lasers with quantum well and quantum dot active regions in this material system and found a lower temperature rise as a function of current on the facets of the quantum dot based devices. When a certain temperature has been reached portions of the facet are generally thought to melt [12, 26, 27] sometimes with extruded molten material visible at the facet [15, 28, 29]. The process at the facet, rather than being simple melting, may actually involve dissociation of the group V element leaving a region rich in group III elements [30] which would have a much lower melting point than bulk III-V crystal material. There is insufficient existing experimental evidence to distinguish between melting of a GaIn rich mix or GaInP/AlGaInP eutectic alloy, both in terms of the composition of the surface after damage and of the precise temperature reached. Following the damage at the facet a track of molten material propagates through the active region [12, 14, 15, 26, 27, 30, 31]. Laser light is absorbed at the interface between the molten region and adjacent material, where the temperature is raised and bandgap reduced, causing that layer of material to melt. This process is repeated and thus the molten region propagates through the active region [13] and immediately surrounding waveguide region only. Re-absorption of optical power in the cladding layers may require too high a temperature increase. The leading edge of the molten region can be seen as a bright electroluminescent spot in suitably prepared samples [31]. The molten material resolidifies into a polycrystalline, highly defective non-luminescent region [30, 31] which in subsequent examination by transmission electron microscopy (TEM) for example, is seen as a dark line propagating back from the facet [13, 15, 32] (catastrophic dark line or CDL) which sometimes splits into several branches. This has been observed in a variety of material systems [14, 15, 31, 33] and also in the 650 nm emitting GaInP/AlGaInP system [32]. Eventually so much material is damaged that further lasing is prevented at that injection current. However, the destruction of a quantity of active region material merely raises the threshold current. If the current is turned up lasing can recommence [33]. The increase in damage to the device continues as long as the current is supplied and not too much of the active region has been destroyed. The initial facet damage and propagation of the molten region are two separate processes. Pulsed measurements can cause a periodic variation in the appearance of the molten region if current pulses are applied after the initial damage [15]. The speed of the propagating molten region has been measured to be between 1 m/s and 20 m/s [14, 15, 19, 33, 34] and a measurement is made as part of this work. The process of initial

relatively slow facet temperature rise, followed by thermal runaway, facet melting, propagation of dark lines and drop of lasing power takes place on a timescale of the order of hundreds of nanoseconds. The timescale of measurement has been reduced to microseconds [19, 34] and to tens of nanoseconds in this work, and has since been reduced further.

Slow degradation causes a buildup of defects which eventually leads to COD, with a shorter time until failure at higher operating powers and temperatures. This provides a means for accelerated life testing on a shorter timescale than the tens of thousands of hours a commercial device typically lasts, by raising the operating temperature. The rate at which failure is found to occur can be described by an Arrhenius type analysis [35, 36] which describes the time to failure in the form of a rate equation:

$$\frac{1}{t_{COMD}} = const \exp(-E_a/kT) \quad (2.1)$$

where t_{COMD} is the time to COMD, k and T are Boltzmann's constant and the absolute temperature and E_a is an activation energy. The activation energy found by this process was a phenomenological quantity and was not attributed to any one particular process, as in a chemical rate equation. In spite of this the technique can be used to relate failure times at different temperatures enabling accelerated life testing to be carried out. The physical processes have more recently been considered in the context of aging models that related defect types to activation energies [37]. Proper application of this technique to COMD would require specific knowledge of the defects involved.

I did not use this analysis in the time studies, but developed a theory that related the time to COMD to the energy required to melt a quantity of active region material.

In the rest of this chapter I will give a brief account of basic sample processing, characterisation and the measurement of optical power. I will then discuss the multisection technique, which enables measurements of gain and absorption in absolute units, and, if a calibration process is carried out, enables a determination of spontaneous emission in absolute units for the whole device. The absorption of light by a laser diode with the generation of a photocurrent or photovoltage is the basis for three more techniques used in this work: edge photovoltage spectroscopy (EPVS), which was carried out on apparatus that I built, and photocurrent spectroscopy (PC) and laser beam induced current (LBIC) carried out on existing apparatus in Berlin. I then describe the measurement of facet temperature. An important part of my project was to model and accurately measure farfield intensities for structures designed in this lab. I designed and built an apparatus to do this to the required accuracy at large angles. I finally describe some other techniques and any amendments I made, which included an adaptation to increase the time resolution of time to COMD measurements from microseconds to tens of nanoseconds.

2.2 Pulse length, conductivity and COMD power level

Starting with the diffusion equations governing the transfer of heat, and using Henry's result from Carslaw and Jaeger [20] it is possible to get some simple insights into factors that affect the COMD power density limit.

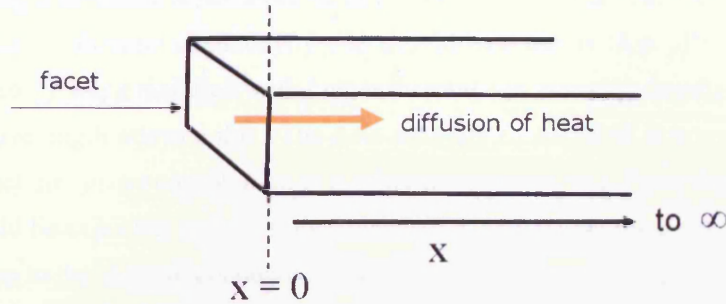


FIGURE 2.1: Laser device modelled as a 1-D semi-infinite solid with heat generated over the surface at $x = 0$ and able to diffuse into the interior of the device

Assuming the laser can be treated as a one dimensional semi-infinite solid with heat supplied uniformly across the plane of the facet and only lost by conduction into the interior, and applying boundary conditions to the diffusion equations for 1-D semi-infinite solid, a solution of the following form is found:

$$\Delta T = 2 \frac{F}{K} \left[\left(\frac{\kappa t}{\pi} \right)^{1/2} \exp \left(-\frac{x^2}{4\kappa t} \right) - \frac{1}{2} x \operatorname{erfc} \left(\frac{x}{2(\kappa t)^{1/2}} \right) \right] \quad (2.2)$$

where ΔT is the temperature rise, K is the thermal conductivity, F is the rate of input of heat at the facet ($=K\Delta T/\Delta x$ where x is the distance from the facet) κ is the thermal diffusivity ($K/(\rho c_p)$, ρ is the density, c_p is the specific heat at constant pressure), t is time and erfc is the complementary error function.

If x is set to zero (at the facet)

$$\Delta T = 2 \frac{F}{K} \left(\frac{\kappa t}{\pi} \right)^{1/2} \quad (2.3)$$

Rearranging this and replacing κ with $K/(\rho c_p)$ it can be seen that for a fixed temperature rise ΔT , the power at COMD, F depends on the following factors:

$$F \propto \frac{1}{t^{1/2}} \quad (2.4)$$

and

$$F \propto (K\rho c_p)^{1/2} \quad (2.5)$$

If t is taken as the pulse length in equation 2.4, the power density at COMD should be inversely proportional to the square root of the pulse length. This is for a 1-D situation, however, valid when $\sqrt{(\kappa t)}$, which I calculated to be $2 \mu\text{m}$ for this material, is much smaller than the dimensions of the device. For a realistic device the heat will diffuse away in three dimensions at the edges of the quantum wells, improving cooling, but boundaries between layers will add further resistivity, giving a different dependence of power on pulse length. The COMD power density also depends on the thermal conductivity and should increase as $(K\rho c_p)^{1/2}$ so improvements would be gained by using materials with higher thermal conductivity, density and specific heat, if choice of wavelength allowed this. The hole mobility in AlGaInP is known to be low [38], which will affect the carrier contribution to the thermal conductivity. From this a greater thermal resistivity would be expected in the p-doped quaternary layers than the n-doped layers. The lattice contribution to the thermal conductivity, which is the more important contribution in lightly doped semiconductors [39], of GaInP decreases by an order of magnitude from the values for the binaries GaP and InP due to the effect of disordering in the alloy [40]. Addition of Al to form the quaternary AlGaInP, however, has a relatively small effect [41] due to the large difference in molecular masses between AlP and GaP or InP. The cladding layers are highly doped (10^{18} or 10^{19} for these structures), which would tend to increase the thermal conductivity, however this is offset by the cladding layer thicknesses, which are much greater than those of the intrinsic layers (figure 3.2). Thermal conductivity must be carefully taken into account when designing the structure.

2.3 Sample preparation and characterisation of devices

Careful preparation and characterisation of devices is essential to obtain good quality results.

The method of mounting has a profound effect on the performance of high power devices [42–44] with p-side down mounting to reduce the distance between the active region and the heat sink being the norm. In addition careful choice of solder and submount, allowing for differences in thermal expansion, and sophisticated cooling, with the heat sink mounted on a thermoelectric cooler, which in turn is mounted on a water cooled microchannel plate controlled by a temperature controller, are required. The distance heat can diffuse during the time a 1000 ns pulse lasts ($\sqrt{(\kappa t)}$, $2 \mu\text{m}$) is far less than the sample dimensions. For pulsed measurements a much simpler type of mounting is sufficient, and is essential if large numbers of devices are to be used, in a COMD experiment, for example.

Oxide isolated stripe lasers are processed in-house from structures grown on n-doped substrates oriented 10° towards the [111] direction to prevent ordered growth in the alloy. I examined each batch of devices under the microscope, selecting only devices with smooth, well adhering gold

contacts and flat facets. I mounted the devices on copper blocks on transistor headers using conductive epoxy (figure 2.2).

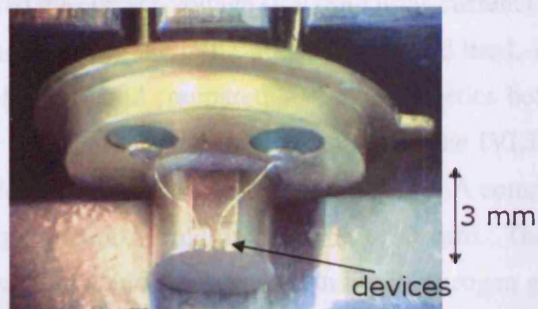


FIGURE 2.2: A p-side up mounted pair of $320\ \mu\text{m}$ lasers on a copper block on a transistor header, with one wire to each device.

The structural details of the devices are shown in figure 2.3. Also shown are details of the multisection devices used in gain measurements. These are non-lasing test structures where lasing is prevented by having unpumped sections at the rear, and either by cleaving perpendicular to the off-axis direction so that the facets were not parallel to each other, or by deliberately damaging the rear facet.

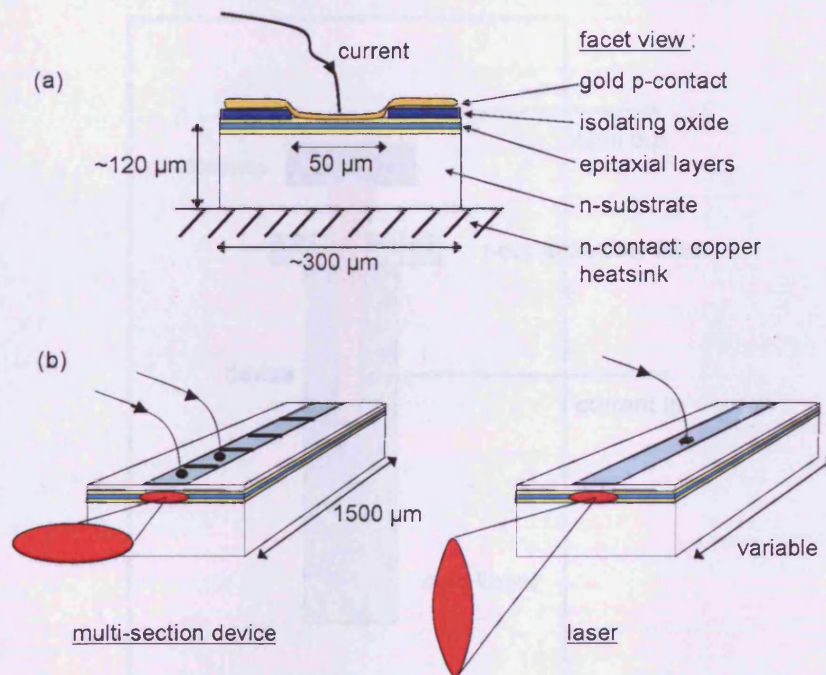


FIGURE 2.3: Oxide isolated stripe lasers produced in-house. (a) Cross-section of both types of device. Current is applied to a central metallised stripe in the p-side with a $50\ \mu\text{m}$ wide contact region defined by oxidised isolated areas. Gain guiding then confines the optical mode beneath this stripe. The n return path is via the copper heat sink. Lasing devices of varying lengths were produced by cleaving. In the (non-lasing) multi-section devices the contact stripe is segmented into $300\ \mu\text{m}$ lengths. (b) Schematic of the non-lasing multi-section and laser devices, showing the difference in the contact arrangements and also the difference in the shapes of the farfield, with wide divergence of the farfield perpendicular to the epitaxial layers in the laser.

2.3.1 Measuring current-voltage and light-current characteristics: IVLT

After mounting I measured the current-voltage (I-V) and light-current (L-I) characteristics of the devices at room temperature, using the IVLT apparatus. I used the L-I characteristics to obtain the threshold currents of lasers, and compared I-V characteristics between lasers, or between sections in multisection devices to ensure uniform quality. The IVLT apparatus could also be used to measure threshold current as a function of temperature. A computer was used for control and data acquisition using a PC30AT multipurpose A to D card. The device was placed in a cryostat with a cold finger that could be immersed in liquid nitrogen giving a working range of 180 K to 400 K. The temperature was monitored using a calibrated diode and current applied to a heater in the cryostat to control the temperature. Current was supplied by a pulse generator with a potential divider driven by a stepper motor and current (I), voltage (V) and light (L) were measured using a boxcar which output data to the computer. Subroutines controlled temperature change, ramping up of current with measurement of I, V and L at each temperature. Later I wrote subroutines that dovetailed into the existing program to control and acquire data from the farfield apparatus I constructed. I obtained the threshold currents manually using the intersection of a tangent to the L-I characteristic.

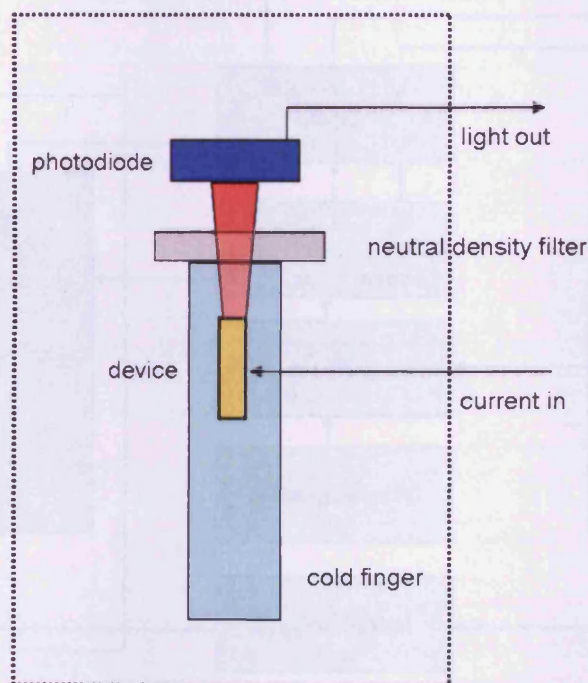


FIGURE 2.4: Schematic of the IVLT cryostat. The setup shown replaces the part of the farfield apparatus enclosed by dotted lines in figure 2.5. The same control and data acquisition is used for each

2.3.2 The farfield apparatus and measurements

I designed and built a system for measuring farfields with the device mounted on a rotating turntable. Some setups use a stationary device with the slit traversing the farfield, but this was not sufficiently sensitive for the low intensity light at large angles, important in this work. The apparatus was designed by me, constructed by Mr G. Summers in the workshop and assembled by me. I wrote a software routine to set the current, rotate the turntable and measure the light in real time for lining up purposes (so that the system could also be used with infra-red emitting lasers) and then measure light as a function of position over a specified number of steps and output this information as a data file. The system works with the existing IVLT setup, using the same current and light measurement for consistency, and saves data in the same form as existing routines, thus forming an additional generally available technique. The position of the device is set with an xyz translation stage with tilt in two directions provided by a mirror mount. A rotation stage enables the device to be rotated so that both lateral and vertical farfields can be measured. The sample holder is mounted on a turntable driven by a computer controlled stepper motor. The part enclosed in dashed lines is interchangeable with the IVLT system.

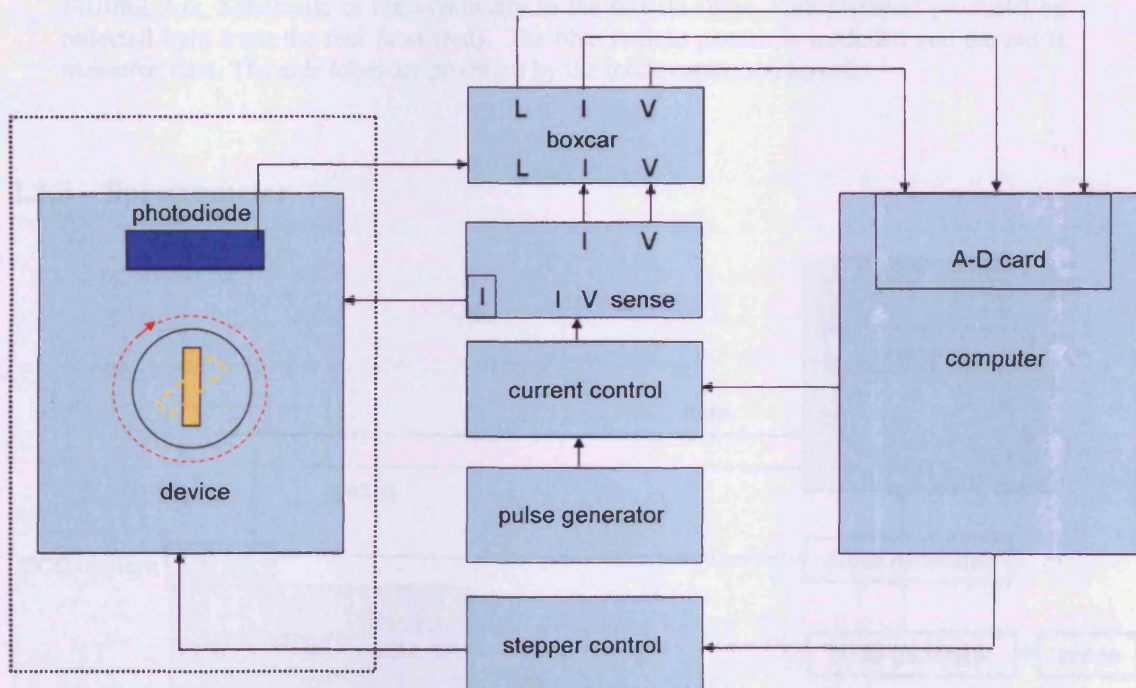


FIGURE 2.5: Schematic of the farfield system. The position of the device is completely adjustable. It is mounted on a turntable driven by a computer controlled stepper motor. The computer also sets and measures the current, and records light and position as the turntable rotates. The part enclosed in dashed lines can be replaced by IVLT system

The farfield system was sensitive enough to measure very small side lobes at large angles, and also to detect light from the rear facet which, reflected off the header, added to the signal from

the front facet on one side of the farfield, giving an asymmetric plot. (Figure 2.6). This was eliminated from data by painting the header behind the rear facet black.

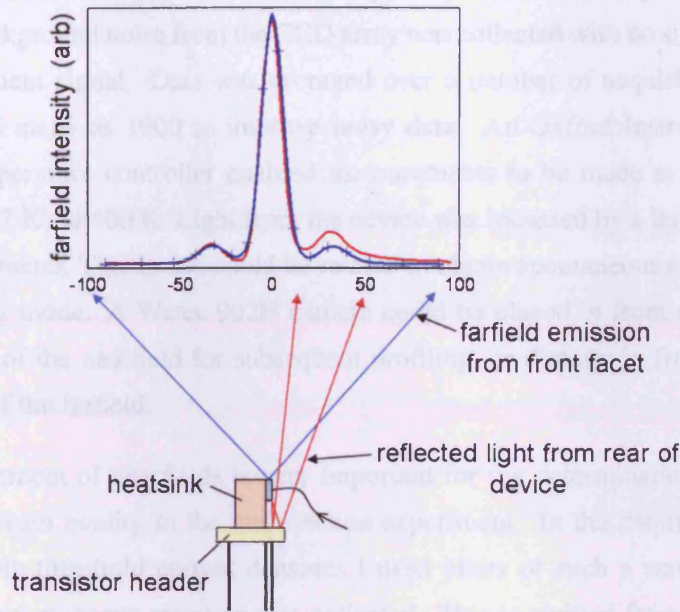


FIGURE 2.6: Schematic of the asymmetry in the farfield (blue, with markers) produced by reflected light from the rear facet (red). The blue farfield pattern is modelled and the red is measured data. The side lobes are produced by the mode expansion layers.

2.3.3 Spectrometer

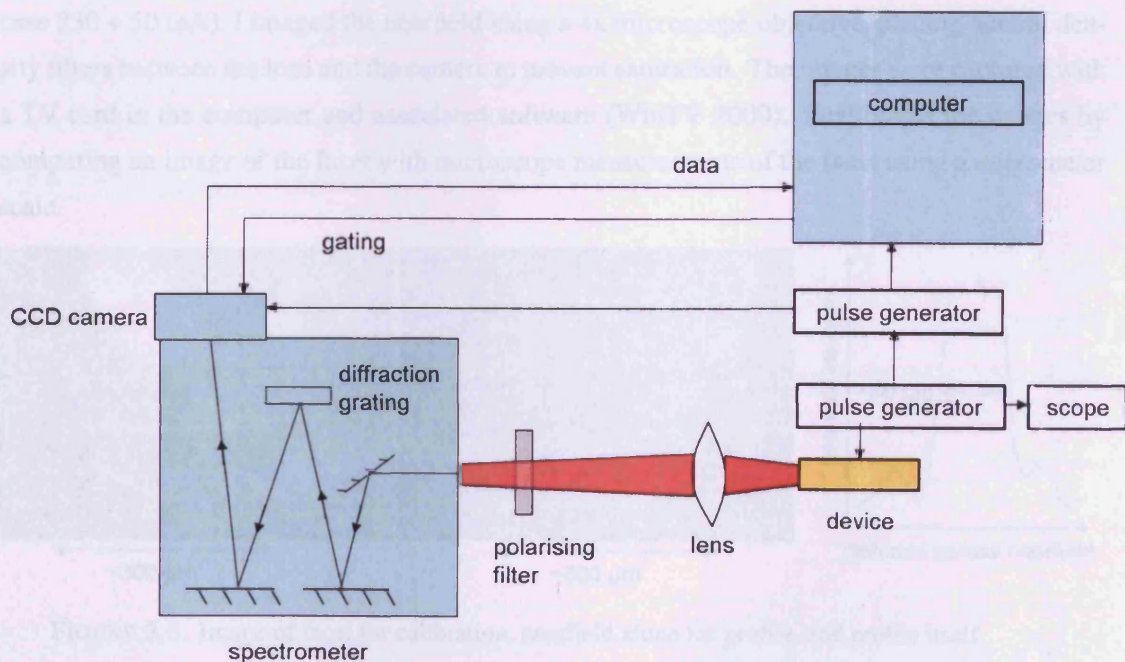


FIGURE 2.7: Schematic of the spectrometer system

The spectrometer setup consisted of an Oriel 74050 grating spectrometer and an Andor CCD array with a gated image intensifier at the output. The complete system used proprietary software for data acquisition, the current, from an in-house pulse generator (built by Mr R. Tucker) being set manually. Background noise from the CCD array was collected with no signal and subtracted from any subsequent signal. Data was averaged over a number of acquisitions, usually 100, but sometimes as many as 1000 to improve noisy data. An Oxford Instruments MicrostatN cryostat and temperature controller enabled measurements to be made at temperatures from liquid nitrogen (77 K) to 400 K. Light from the device was focussed by a lens onto the entrance slit of the spectrometer. The device could be rotated to obtain spontaneous emission at an angle to the main lasing mode. A Watec 902H camera could be placed in front of the spectrometer to obtain images of the nearfield for subsequent profiling, or directly in front of the device to image a portion of the farfield.

Accurate measurement of nearfields is very important for the determination of power density at the facet and beam quality in the multisection experiment. In the determination of current spreading to obtain threshold current densities I used filters of such a wavelength that as far as possible only spontaneous emission was collected. This is emitted from the location of the carriers, enabling the measurement of current spreading. The beam of amplified spontaneous emission, guided light which was narrowed by gain-guiding, would underestimate the current width.

An example of a nearfield image captured with a Watec 902 ccd camera is given in figure 2.8. Typical conditions are pulsed current (400 ns at 1 kHz) at about 50 mA above threshold (in this case 230 + 50 mA). I imaged the nearfield using a 4x microscope objective, placing neutral density filters between the lens and the camera to prevent saturation. The images were captured with a TV card in the computer and associated software (WinTV 2000). I calibrated the images by comparing an image of the facet with microscope measurements of the facet using a micrometer scale.

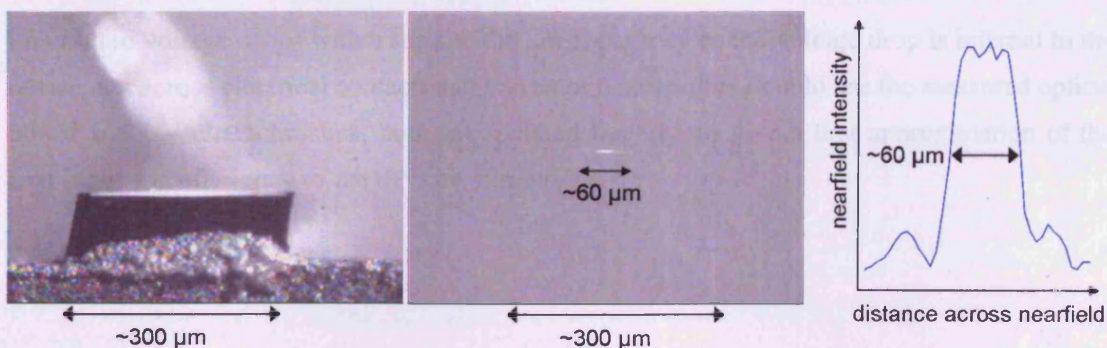


FIGURE 2.8: Image of facet for calibration, nearfield alone for profile, and profile itself

Further examples of nearfield profiles are given in chapter 4.

2.3.4 Power measurement with the integrating sphere

An integrating sphere is designed to collect all the power emitted by the laser. The laser light is multiply scattered off the white, rough surface of the interior of the entrance sphere to give uniform illumination across the surface. A known fraction of the light passes through the aperture to the second sphere where it is scattered again. A fraction is then collected by the photodiode.

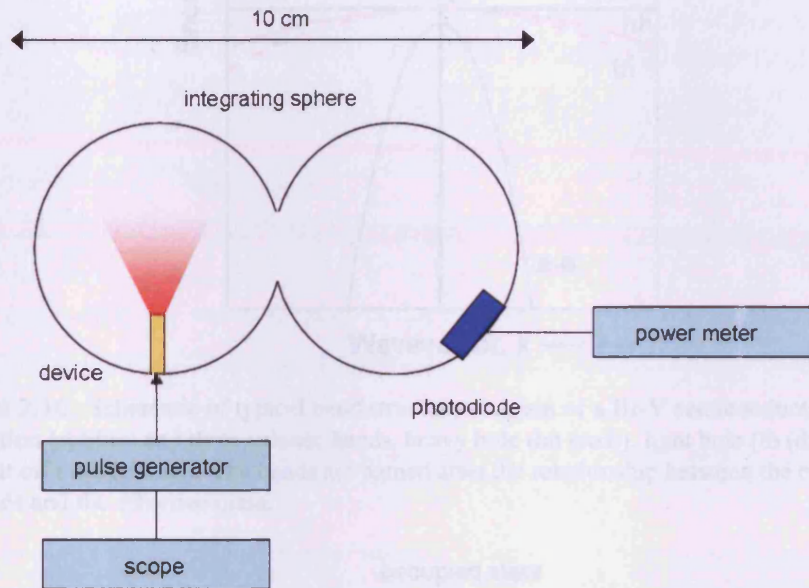


FIGURE 2.9: Schematic of the integrating sphere. Light emitted from the device undergoes repeated random scattering from the white, rough surface, producing uniform illumination over the interior surface of the sphere. A known fraction, based on the ratio of surface area to aperture size, passes to the second sphere where the same scattering occurs followed by absorption of a known fraction by the detector.

2.3.5 Measurements of voltage drops

I measured voltage drops which showed the large majority of the voltage drop is internal to the device, not across electrical contacts and transistor header, thus I could use the measured optical power and I-V characteristics, both extrapolated linearly, to give a first approximation of the heat input and efficiency of the devices, if required.

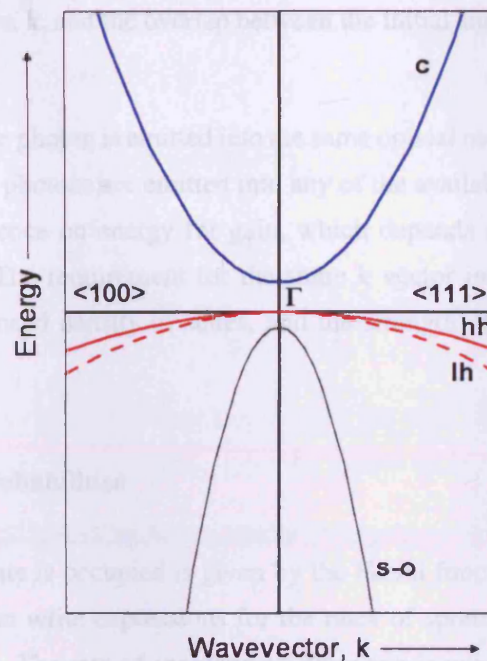


FIGURE 2.10: Schematic of typical band structure diagram of a III-V semiconductor showing conduction (c, blue) and three valence bands, heavy hole (hh (red)), light hole (lh (dashed red)) and split off (s-o (black)). The bands are named after the relationship between the curvature of the bands and the effective mass.

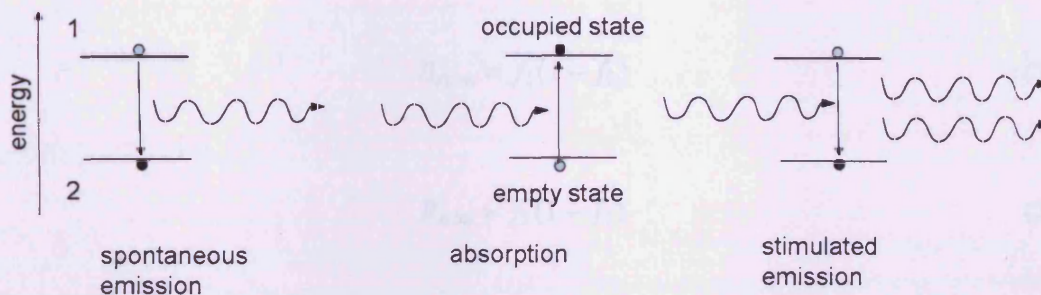


FIGURE 2.11: Schematic of emission and absorption processes between two levels. In emission an electron passes from a higher energy level (1) to a lower one (2) with the emission of a photon of energy equal to the difference between the two levels. This process can be spontaneous or stimulated by a photon. In absorption the energy of a photon is absorbed and the electron passes from a lower to a higher energy state.

2.4 Background theory for the multisection technique, facet temperature measurements and PC/EPVS

2.4.1 Stimulated emission, spontaneous emission and absorption

The rate of transition of carriers from one state to another is affected by three factors: the density of photon modes available, the probability of finding a pair of states, one filled and one empty,

with the same wave vector, k , and the overlap between the initial and final states and the strength of the transition.

In stimulated emission the photon is emitted into the same optical mode as the perturbing photon. In spontaneous emission photons are emitted into any of the available modes in the cavity. This gives a different dependence on energy for gain, which depends on stimulated emission, and spontaneous emission. The requirement for the same k vector in the initial and final state is accounted for in the reduced density of states, and the strength of the transition in the matrix elements.

2.4.1.1 Occupation probabilities

The probability that a state is occupied is given by the Fermi function, f , and that it is not occupied, by $1 - f$. We can write expressions for the rates of spontaneous emission, stimulated emission and absorption. The rate of spontaneous emission is proportional to Einstein's A coefficient and the probability (f_1) of finding an electron in the conduction band, the upper state, multiplied by the probability of finding an empty state in the valence band ($1 - f_2$), with similar expressions for absorption and stimulated emission, which depend on Einstein's B coefficient.

$$R_{spon} \propto f_1(1 - f_2) \quad (2.6)$$

$$R_{stim} \propto f_1(1 - f_2) \quad (2.7)$$

$$R_{abs} \propto f_2(1 - f_1) \quad (2.8)$$

and

$$f = \frac{1}{1 + \exp[(E - E_f)/kT]} \quad (2.9)$$

where E is the photon energy, E_f is the Fermi energy, k is Boltzmann's constant and T is the absolute temperature.

The gain depends on the difference between the rates of stimulated emission and absorption

$$g \propto f_1(1 - f_2) - f_2(1 - f_1) = (f_1 - f_2) \quad (2.10)$$

The usual equations for the rate of spontaneous emission (R_{spon}) and gain (g) are [45]

$$R_{spon} = h\nu \frac{e^2 n}{\pi m_o^2 \epsilon_o \hbar^2 c^3} |M_{ave}|^2 \rho_{red} f_1 (1 - f_2) \quad (2.11)$$

$$g = \frac{1}{h\nu} \frac{\pi e^2 \hbar}{\epsilon_o 2 m_o c n} |M_T|^2 \rho_{red} (f_1 - f_2) \quad (2.12)$$

where $h\nu$ is the photon energy, e is the electronic charge, n is the refractive index, m_o is the rest mass of the electron, ϵ_o is the permittivity and c is the speed of light in free space. ρ_{red} is the reduced density of states and $|M_T|$ and $|M_{ave}|$ are the matrix elements.

At high energies, when the upper levels are almost empty, $f_1 \rightarrow 0$ and $f_2 \rightarrow 1$. Using equation 2.8

$$f_2(1 - f_1) \rightarrow f_2 \quad (2.13)$$

giving for R_{abs}

$$R_{abs} \propto f_2 \quad (2.14)$$

similarly

$$g \propto -f_2 \propto -R_{abs} \quad (2.15)$$

2.4.1.2 The high energy Boltzmann tail of the spontaneous emission

Using equation 2.15 and dividing equation 2.11 by equation 2.12

$$R_{spon} \propto R_{abs} (h\nu)^2 \frac{f_1(1 - f_2)}{f_1 - f_2} \quad (2.16)$$

If the assumption is made that the system is in equilibrium, that is

$$E_{f1} = E_{f2} = E_f \quad (2.17)$$

equation 2.16 reduces to

$$R_{spont} \propto R_{abs}(h\nu)^2 \exp \left[\frac{-(E_1 - E_2)}{kT} \right] \quad (2.18)$$

which is the result used for the facet temperature measurements [28].

2.5 The multisection technique: measurement of gain and absorption

The multisection technique, or segmented contact method [46] enables measurements of modal gain and absorption in absolute units, by measuring the amplified spontaneous emission from different lengths of specially fabricated non-lasing test structures (figure 2.3). By considering the emission in a region where complete population inversion is achieved the spontaneous emission can also be obtained in absolute units. I used this technique to obtain the gain and absorption curves used in this work.

The total spontaneous emission intensity I_{spont} emitted from an element of thickness Δx passing a distance x along the active region and amplified by a net modal gain of $G - \alpha_i$

$$I(x) = \beta I_{spont} \exp[(G - \alpha_i)x] \Delta x \quad (2.19)$$

where β is the fraction of the total spontaneous emission coupled into the waveguide

If this light is amplified over a distance l the total emission is obtained by integrating equation 2.19 with respect to x from 0 to L . If this is done for two lengths, L and $2L$ the following result for net modal gain, $G - \alpha_i$ can be obtained analytically:

$$G - \alpha_i = \frac{1}{L} \ln \left[\frac{I_{meas}(2L)}{I_{meas}(L)} - 1 \right] \quad (2.20)$$

where $I_{meas}(L)$ is the measured intensity for a pumped length of L .

Using the specially prepared device, which has five contactable sections of length $300 \mu\text{m}$ (L), the first section is pumped (L) and then the first two sections ($2L$) at the same current density. The amplified spontaneous emission (ASE) for light of one polarisation is collected as a function of wavelength by the spectrometer (figure 2.7) and equation 2.20 is used to obtain the net modal gain as a function of wavelength.

For the net modal absorption $A - \alpha_i$ a similar result is found:

$$A - \alpha_i = \frac{1}{L} \ln \left[\frac{I_{meas}(1)}{I_{meas}(2)} \right] \quad (2.21)$$

where $I_{meas}(1)$ and $I_{meas}(2)$ are the ASE spectra for the front section and the second section. An example of gain and absorption spectra is shown in figure 2.12, plotted as a function of energy rather than wavelength. The value of α_i is given by the flat region below 1.83 eV, and at higher energies, where $G - \alpha_i$ is equal to $-\alpha_i$ and G is zero, the quasi Fermi level can be obtained (1.94 eV).

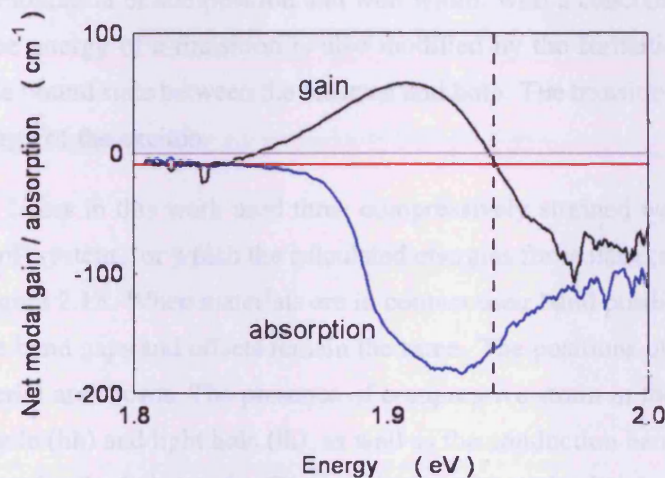


FIGURE 2.12: An example of net modal gain (for a pumping current of 300 mA/section) and absorption spectra for the mode expanded structure used in this work, measured using the multi-section method. The gain (black curve) and absorption (blue curve) meet in the band gap (region below 1.83 eV) giving a value for the scattering loss, α_i (red line), of 9 cm^{-1} . At the transparency point, where the modal gain is zero, the quasi Fermi level separation can be obtained (1.94 eV, dotted line)

2.6 Edge photovoltage, photocurrent and laser beam induced current measurements

Edge photovoltage (EPVS) photocurrent (PC) and laser beam induced current (LBIC) measurements are all obtained when the edge surface of the structure is illuminated by a light source with an intense continuous spectrum (or laser in LBIC), light is absorbed, generating electron-hole pairs. If these are in a region of the structure where a potential gradient exists the carriers will be separated and produce a photocurrent, otherwise they simply recombine. The number of carriers that can be excited depends on the density of states, which, in ideal materials, is a delta function for quantum dots, flat (for one sub-band) for quantum wells and proportional to the square root of the energy for bulk material [24].

2.6.1 Transition energies

The energy of transitions can be calculated using the band gaps and electron affinities of the constituent materials, or by using Model Solid Theory [47], which calculates the band structure and aligns the valence band edges on an absolute energy scale, thus giving the band offsets between materials when they come in contact, as in an epitaxial structure. In both cases the effect of strain and quantum confinement must also be included. Strain is introduced when the composition is changed to give the band gap required for the chosen laser wavelength, which depends on the combination of composition and well width, with a concomitant change in lattice parameter. The energy of a transition is also modified by the formation of an exciton, a hydrogen-atom-like bound state between the electron and hole. The transition energy is reduced by the binding energy of the exciton.

The quantum well lasers in this work used three compressively strained wells and were fabricated in the AlGaInP system, for which the calculated energies for isolated materials are shown schematically in figure 2.13. When materials are in contact their band positions shift relative to one another but the band gaps and offsets remain the same. The positions of the band edges for bulk, isolated material are shown. The presence of compressive strain in the quantum well has caused the heavy hole (hh) and light hole (lh), as well as the conduction band (c) edges to shift, to a different degree for the hole bands. The transitions c-hh and c-lh are shown between the energy levels in the quantum well.

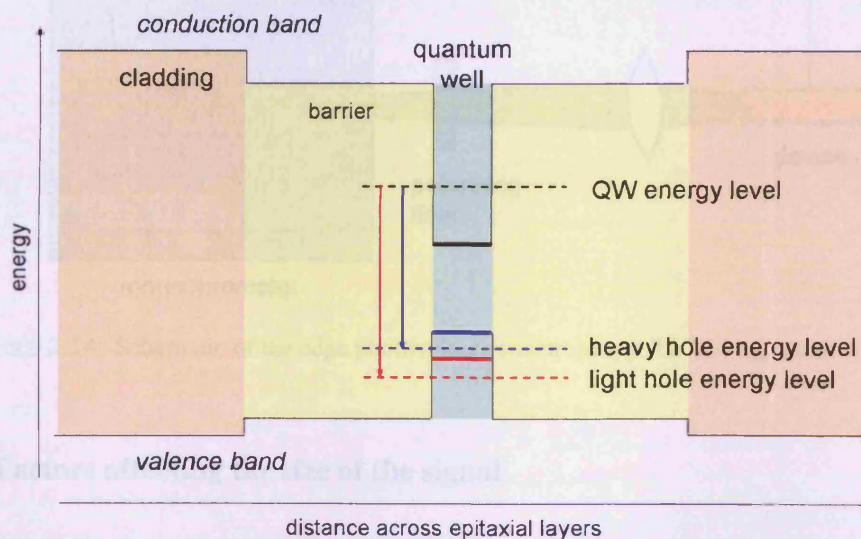


FIGURE 2.13: Schematic of a typical laser structure with one quantum well, showing the band positions in the cladding, barrier and quantum well epitaxial layers for isolated materials. The absolute levels shift when materials are in contact but the bandgaps and offsets remain the same. In a strained quantum well the light and heavy hole band edges (solid lines) have different energies. I compared the calculated transition energies for the barrier material and the conduction to light hole and conduction to heavy hole in the quantum well with EPVS measurements.

2.6.2 EPVS

I based the design of the edge photovoltage spectroscopy (EPVS) system used in these measurements on an existing setup, using similar equipment and some mechanical components made by Mr G. Summers in the workshop. I assembled the system, shown schematically in figure 2.14 and calibrated the wavelength using spectral line sources. This system is used primarily to check transition energies and so the magnitude of the signal is only important in as far as clear transition energies can be identified. Measurement factors that affect the size of the signal include the variation of the intensity of illuminating light as a function of wavelength, response of the diffraction grating and other components. It would be possible to measure the system response and correct for the absolute size of the signal using a calibrated lamp if required. Addition of a preamplifier would enable photocurrent measurements to be made.

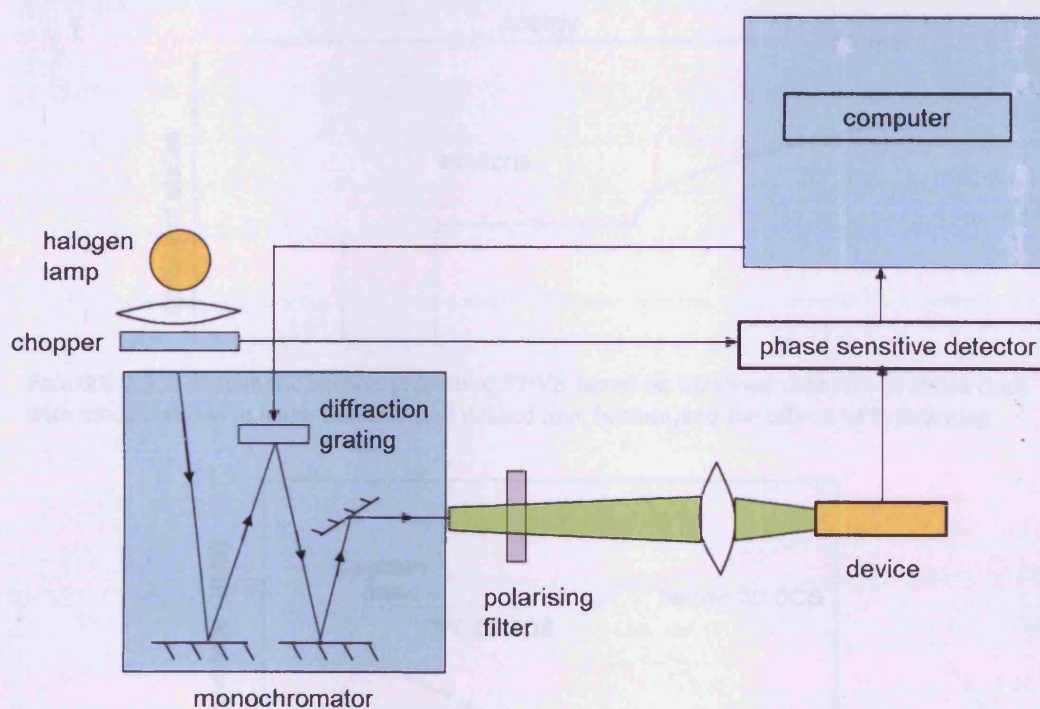


FIGURE 2.14: Schematic of the edge photovoltage spectroscopy (EPVS) apparatus

2.6.3 Factors affecting the size of the signal

The amplitude of the signal depends on whether the system is used in photovoltaic mode (EPVS), where the signal is proportional to the logarithm of the number of carriers collected or photoamperic (PC) mode where the response is linear. Depending on the orientation of the polarising filter the absorption spectrum of both c-hh and c-lh transitions can be observed (TE polarised) or the c-lh (TM) only. The spectra shown were all taken with TE polarisation.

An idealised absorption spectrum (figure 2.15 top) depends on the density of states for the bulk, QW or QD regions of the structure. This is modified by the presence of exciton peaks and broadening, both due to thermal effects and inhomogeneities in factors such as well widths, composition or dot size. The position and separation of the exciton peaks gives information about the composition and well width if the peaks are sufficiently well resolved.

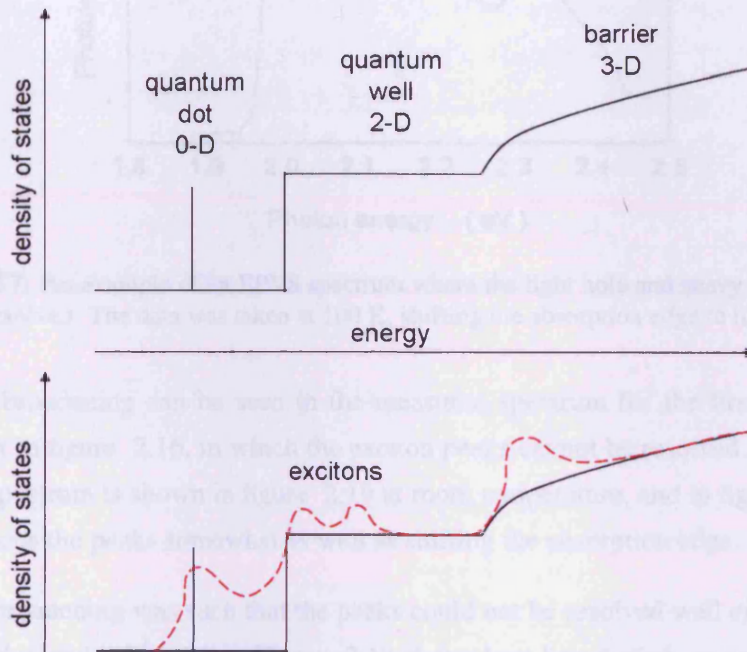


FIGURE 2.15: Schematic showing idealised EPVS based on idealised densities of states (top) with modifications to show excitons (red dashed line, bottom) and the effects of broadening

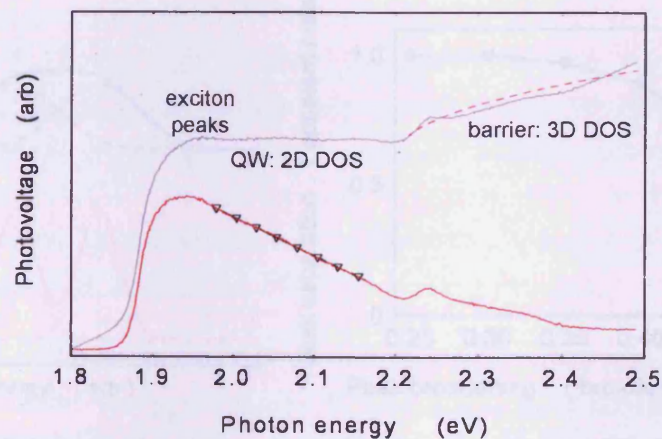


FIGURE 2.16: An example of a measured EPVS spectrum (red) for the mode expanded wafer. In comparison with figure 2.15 there are no 0-D states and the exciton peaks are unresolved. In addition the amplitude decreases gradually as energy increases due to the response of the measurement system. The black line shows the data scaled up with a line function (black points) to give a flat region in the quantum well 2-D region, indicating what an idealised spectrum would look like and showing a flat region where the facet temperature measurements were made

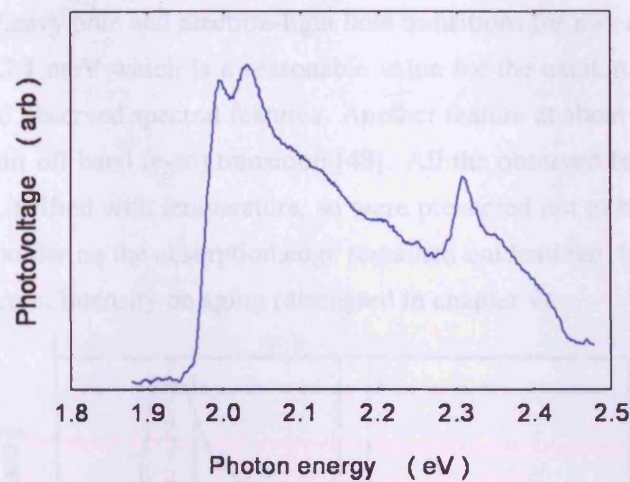


FIGURE 2.17: An example of an EPVS spectrum where the light hole and heavy hole exciton peaks are resolved. The data was taken at 100 K, shifting the absorption edge to higher energy

The effects of broadening can be seen in the measured spectrum for the first growth mode-expanded wafer in figure 2.16, in which the exciton peaks cannot be resolved at all. The third growth wafer spectrum is shown in figure 2.19 at room temperature, and in figure 2.17 at 100 K, which sharpens the peaks somewhat as well as shifting the absorption edge.

The degree of broadening was such that the peaks could not be resolved well enough for Gaussian fits to yield useful information. Figure 2.18 shows how broadening, as well as increasing the uncertainty of the position, apparently shifts peaks closer together.

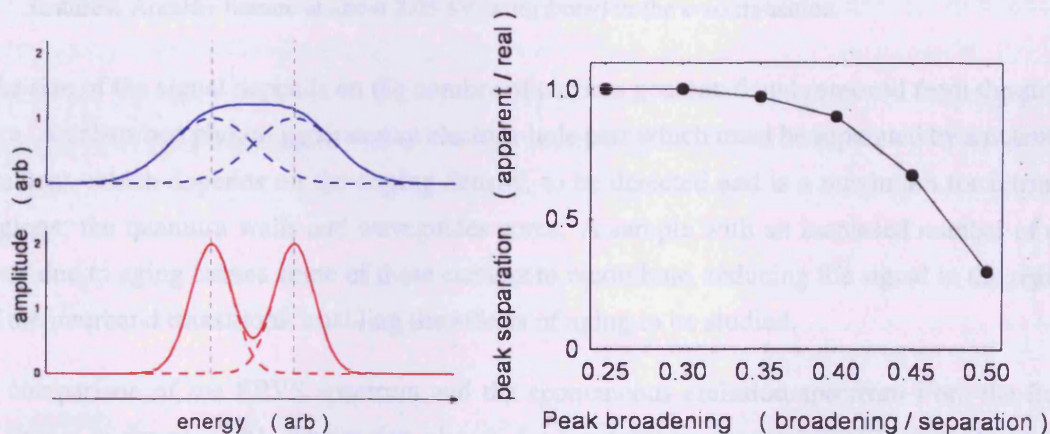


FIGURE 2.18: Schematic of exciton peaks modelled by Gaussians, showing how the degree of broadening, as well as preventing resolution of peaks, apparently shifts peaks closer together. Left upper: Gaussians with a separation of two arbitrary units and a broadening of one unit (blue dotted lines) and their sum (solid line). Left lower: Gaussians with the same integrated area and central positions, but only half a unit broadening (same scale, red lines). Right: variation of apparent separation with broadening. This effect prevents accurate determination of quantum well strain and composition by measurement of e-hh and e-lh peak separation.

The calculated transitions are shown on a room temperature spectrum used to identify the spectral features (figure 2.19). The spectrum, for the third growth mode expanded wafer, shows

calculated electron-heavy hole and electron-light hole transitions for $n=1$ and $n=2$. These were rigidly shifted by 23.4 meV which is a reasonable value for the exciton binding energy, and then corresponded to observed spectral features. Another feature at about 2.05 eV is attributed to the electron to split off band (e-so) transition [48]. All the observed features, together with the absorption edge, shifted with temperature, so were presumed not to be artifacts due to the system. A slight shoulder on the absorption edge remained unidentified, but a showed a strong decrease in photocurrent intensity on aging (discussed in chapter 4).

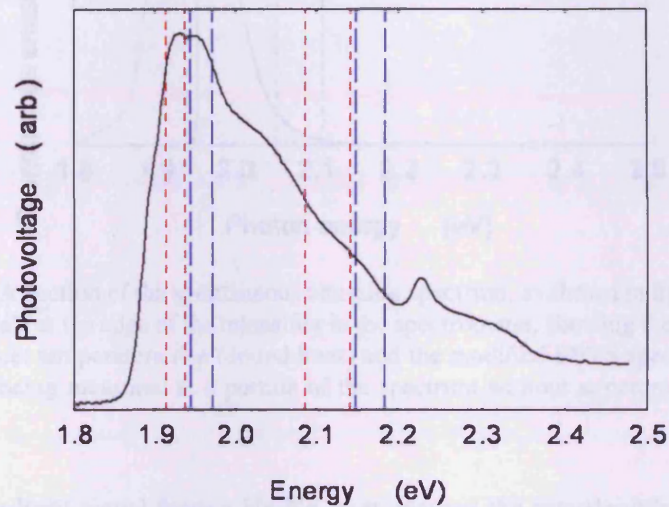


FIGURE 2.19: A spectrum for the third growth mode expanded wafer showing calculated electron-heavy hole (red dotted lines) and electron-light hole transitions (blue dashed lines) for $n=1$ (centred at 1.93 eV) and $n=2$ (centred at 2.15 eV) which correspond to observed spectral features. Another feature at about 2.05 eV is attributed to the e-so transition.

The size of the signal depends on the number of carriers generated and removed from the structure. An absorbed photon generates an electron-hole pair which must be separated by a potential gradient, which depends on the doping density, to be detected and is a maximum for intrinsic regions: the quantum wells and waveguides cores. A sample with an increased number of defects due to aging causes some of these carriers to recombine, reducing the signal in the region of the interband transitions, enabling the effects of aging to be studied.

A comparison of the EPVS spectrum and the spontaneous emission spectrum from the facet is shown in figure 2.20. The region chosen for temperature measurement is away from any structure due to interband transitions.

2.6.4 Photocurrent and laser beam induced current

The photocurrent (PC) measurements were carried out (by Mr R. Giri) on an existing setup at MBI, Berlin [49], using a Bruker IFS 66v/s Fourier Transform spectrometer with a halogen white light source, using a pre-amplifier to take data in photocurrent rather than photovoltage

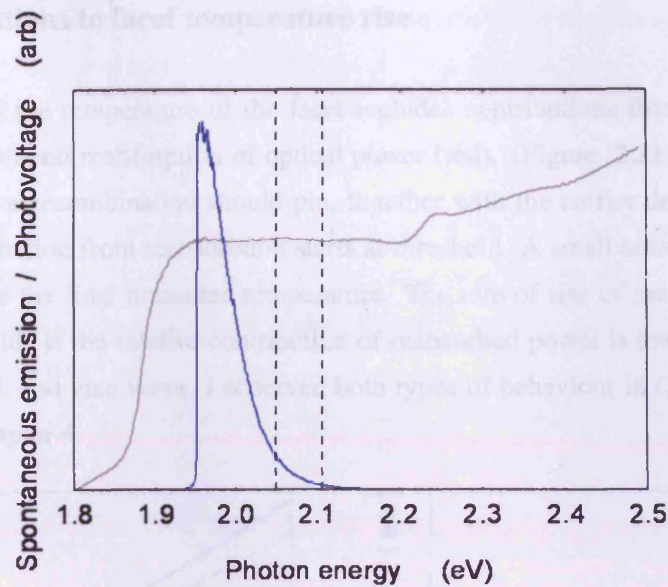


FIGURE 2.20: A section of the spontaneous emission spectrum, as shown in figure 4.10, (with a cutoff at 1.95 eV at the edge of the intensifier in the spectrometer, showing the region sampled to determine facet temperature rise (dotted lines) and the modified EPVS spectrum. The facet temperature is being measured in a portion of the spectrum without structure, as required by the theory.

mode. A reference light signal from a He-Ne laser ensures the wavelength calibration has not changed and can be seen as a spike in the spectra shown in chapter 4. The key difference between PC and laser beam induced current (LBIC) is that the PC uses a spread of wavelengths at a fixed sample position to get a spectrum, whereas the LBIC setup incorporates a translation stage and uses a laser at fixed wavelength, giving amplitude as a function of position across the facet of the device. Different laser wavelengths can be chosen to give a different penetration depth into the device, and this was used in the determination of damage depth in QD and QW devices, as will be discussed later. The LBIC measurements were carried out by Ms S. Schwirzke-Schaaf.

2.7 Facet temperature measurements

Catastrophic optical mirror damage is triggered when the facet temperature reaches a critical value and thermal runaway takes place. The effectiveness of measures to prevent facet temperature rise need to be assessed by measuring the rate of facet temperature rise with current. I measured the facet temperature rise for QW and QD devices and describe these results in chapter 4.

2.7.1 Contributions to facet temperature rise

A measurement of the temperature of the facet includes contributions from non-radiative recombination (black) and reabsorption of optical power (red). (Figure 2.21). The contribution due to non-radiative recombination should pin, together with the carrier density, at threshold, whereas the contribution from reabsorption starts at threshold. A small amount of bulk heating adds to this to give the final measured temperature. The rate of rise of measured temperature changes at threshold. If the relative contribution of reabsorbed power is low the slope will decrease at threshold, and vice versa. I observed both types of behaviour in QW devices, as will be discussed in chapter 4.

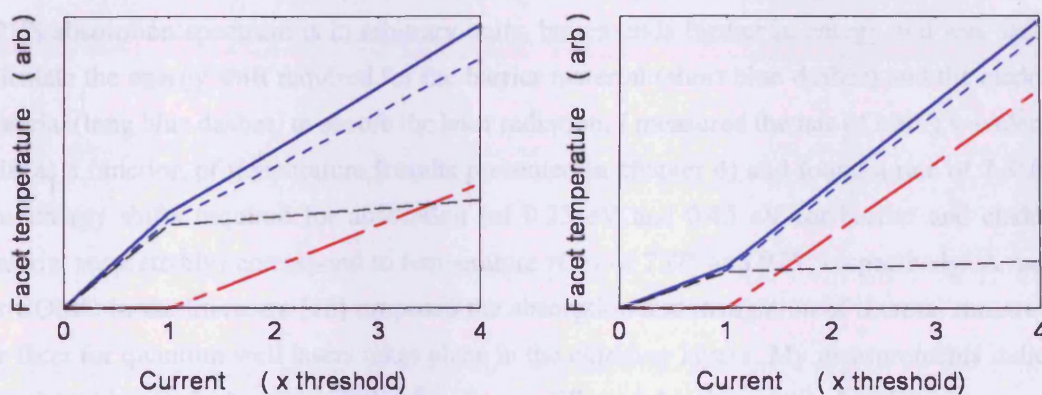


FIGURE 2.21: The major contributions to measured facet temperature come from non-radiative recombination (black dashed line) and reabsorption of optical power (red dot dash line), which combine to give the blue dotted line. A small amount of bulk heating adds to this to give the final measured temperature. (Solid blue line). If the relative contribution of reabsorbed power (red dot dash) is low the slope will decrease at threshold (left hand graph), if higher, the slope will increase (right hand graph). The contribution due to non-radiative recombination should pin, together with the carrier density, at threshold, whereas the contribution from reabsorption starts at threshold

Several methods such as the microRaman, thermography and thermorelectance methods, all with various advantages and disadvantages in terms of probe beam size and heating, temperature and time resolution and penetration depth have been used to measure the temperature of laser facets [50]. An advantage of the method that uses the high energy Boltzmann tail of the spontaneous emission spectrum is that no probe laser is used, which adds the artifact of an extra temperature rise to the measurements: the device is performing completely normally.

2.8 Bandgap shift with heating

When the temperature increases the bandgap decreases, causing a shift in absorption edge and lasing wavelength. I used measurements of lasing wavelength as a function of temperature to confirm a low bulk temperature rise during facet temperature measurements, and present these

results in chapter 4. The shift in absorption edge with temperature, together with measurements of the absorption spectrum at room temperature, can be used to predict a value of the absorption of heated facet material, necessary for consideration of the depth of heated material contributing to the facet temperature determination.

The reabsorption of optical radiation is exacerbated by the rise in facet temperature which leads to a shift in the absorption edge and a concomitant increase in the absorption constant, α . Figure 2.22 shows gain and absorption measured in absolute units using the multisection method for the structures used in this work at a current density of 20 kA/cm^2 (approximately twice threshold), and an EPVS absorption spectrum. The lasing wavelength at room temperature is indicated by the vertical red lines. The spectra shift to lower energies as the temperature is raised. The EPVS absorption spectrum is in arbitrary units, but extends further in energy and was used to calculate the energy shift required for the barrier material (short blue dashes) and the cladding material (long blue dashes) to absorb the laser radiation. I measured the rate of lasing wavelength shift as a function of temperature (results presented in chapter 4) and found a rate of $7.8^\circ/\text{nm}$. The energy shifts required for absorption (of 0.33 eV and 0.45 eV for barrier and cladding material respectively) correspond to temperature rises of 757° and 975° respectively. A model for COMD in the literature [16] proposed the absorption and instigation of thermal runaway at the facet for quantum well lasers takes place in the *cladding* layers. My measurements indicate that absorption in the barrier and cladding layers will not take place until after thermal runaway.

The gain curve gives the temperature range for which the QW facet material is non absorbing, with a positive gain. Using the same argument as above the maximum temperature rise necessary for the quantum wells to become absorbing is 117° , assuming there is no carrier depletion due to other processes, such as non-radiative recombination. This value agrees with the measured temperature rise before thermal runaway of $120\text{-}140^\circ \text{ C}$ for AlGaAs lasers [18].

2.9 Theory and modelling of waveguides, nearfields and farfields

Modelling of waveguides is based on the theory for a 3 slab waveguide. Maxwell's equations, with boundary conditions at the interfaces between the layers are solved in a similar process to that used for a quantum well [51].

This process was extended to many layers in the software I used for the modelling (originally written by Dr. G. Berry [52] and modified subsequently). The software uses the transfer function method to model the nearfield, outputting nearfield (amplitude or intensity) as a function of position and confinement factors within each layer. This output is then Fourier transformed to obtain the farfield as a function of angle [24]. The nearfield profiles depend on the refractive index and thickness of the layers and the wavelength of the laser radiation.

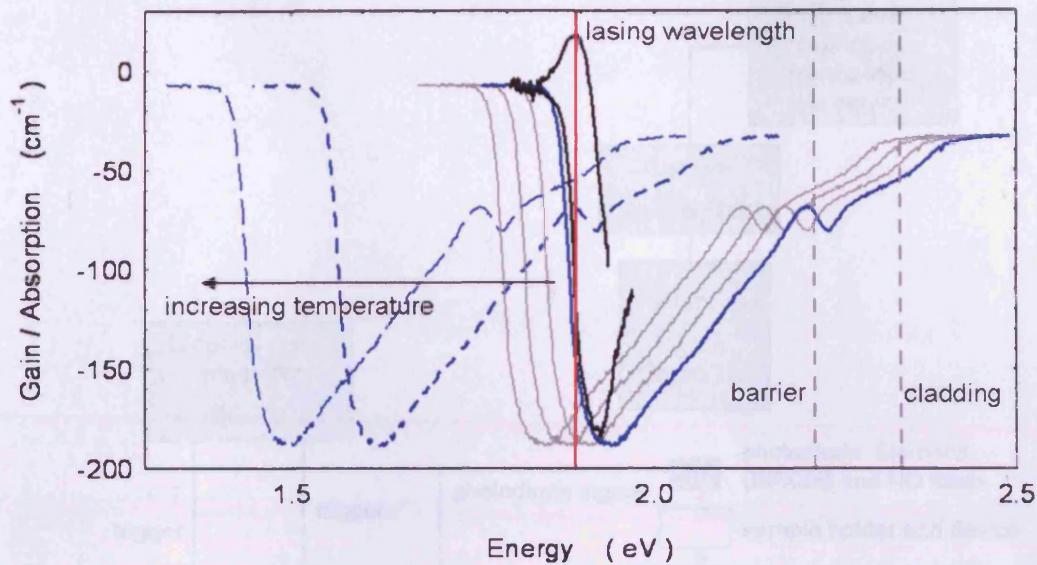


FIGURE 2.22: Shift of absorption required to cause absorption of lasing radiation in the barrier or cladding material at the facet. The EPVS absorption spectrum (arbitrary units, blue) is compared with the calibrated gain and absorption curves (as shown in figure 2.12) but extends over a larger energy range. The solid red line (1.893 eV) indicates the energy of the lasing radiation emitted from the room temperature interior of the device. The energies corresponding to the barrier and cladding material bandgaps (2.22 and 2.34 eV respectively) are indicated by dotted lines. The spectra shift to lower energies as the temperature is raised. The dashed blue lines show the energy shift required for the barrier material (short dashes) and the cladding material (long dashes) to absorb the laser radiation.

It is generally found the light tends to be confined in regions of higher refractive index [53] which was evident in both modelling and measurements of the mode expanded structures to be discussed in chapter 3.

I used the values of confinement factors obtained from the software to calculate the spot size as a function of wavelength. The confinement factor, Γ , is the fraction of the intensity confined within each layer. The spot size, d/Γ , where d is the well thickness gives the width the light would occupy if the profile was square, with the height at maximum intensity. The FWHM or $1/e^2$ width of the calculated mode could equally well have been used to quantify the beam area at the facet, but I used spot size because this figure is widely used in the literature.

2.10 Amendments to standard technique in Berlin to measure the time to COMD

The standard setup in Berlin can be used to apply single, high current (35 A) pulses, using a Picolas (LDP-V 50-100V3) pulse generator to which devices are soldered directly, giving measured rise times of 6 ns. Thermal imaging and nearfield cameras carry out simultaneous imaging of the facet with a time resolution of 7 μ s, from which a time to COMD of 100-200 ns

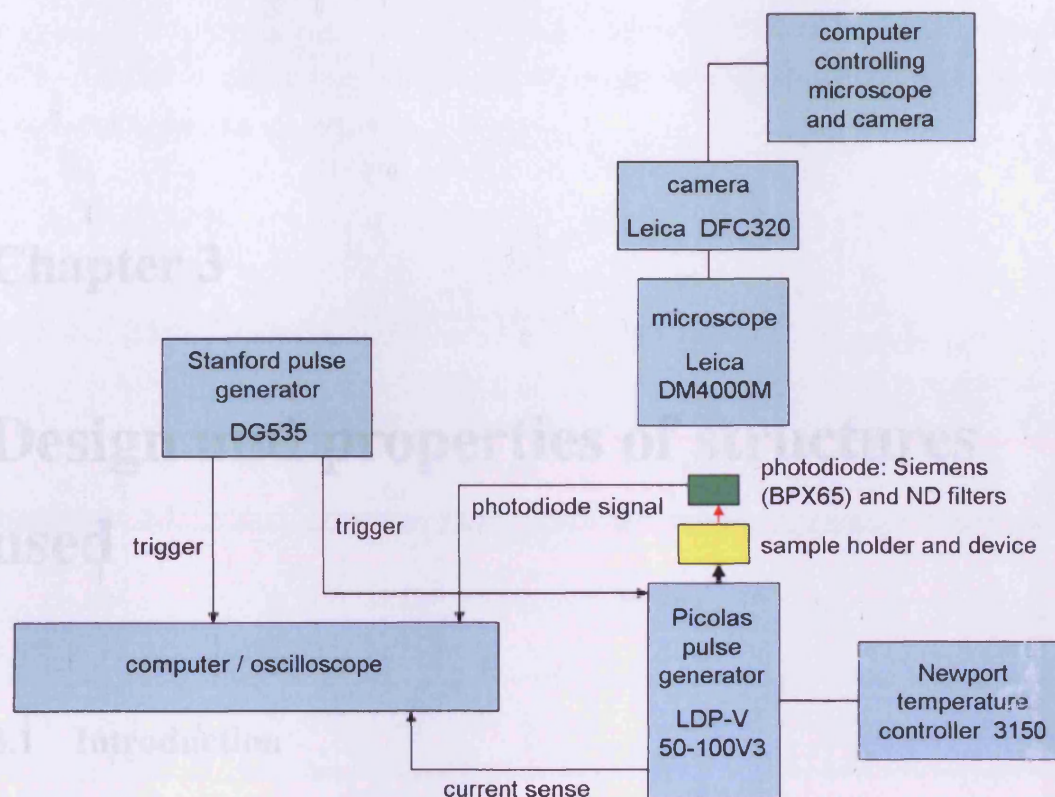


FIGURE 2.23: The experimental setup after amendment for higher time resolution

was inferred [19]. COMD is detected by the presence of thermal flashes or temperature spikes [54], at points on the facet, which are found to correlate in position with points of high intensity in the nearfield and dark line defects in subsequent cathodoluminescence (CL) analysis.

I amended this setup to increase the time resolution from the $7 \mu\text{s}$ used in thermal imaging to a measured $18 (\pm 2 \text{ ns})$ in this investigation, by using a photodiode (Siemens BPX65), in place of the thermal imaging and nearfield cameras, and monitored the light output. (Figure 2.23). The transistor headers were soldered directly to the output of the pulse generator which was mounted under a high quality Leica DM4000M optical microscope so that the nearfields and facets could be imaged (using a Leica DFC320 camera) without moving the device. The photodiode and neutral density filters, used to prevent saturation when the nearfields and light pulses were recorded, were inserted between the device and the microscope during the pulse. I recorded images of the nearfield before and after the current pulse and used these to measure the drop in output power and the area of the facet damage. The occurrence of COMD was confirmed by the permanent drop in light level sensed by the photodiode, the extreme reduction in nearfield intensity and the visible damage on the facets. In a supplementary investigation I subjected one device to repeated identical 10 A, 1000 ns pulses to provide additional confirmation of the permanent nature of the damage to the device after the first pulse.

The acquisition of data is described in Chapter 5, together with the results.

Chapter 3

Design and properties of structures used

3.1 Introduction

In this chapter I discuss the narrow farfield quantum well mode expanded structure designed for fast DVD RW applications by Prof. P. Smowton and grown by IQE Europe Ltd., for this PhD project, prior to its commencement.

The structure was designed to have an equally narrow farfield but a higher confinement factor than an existing design used as a comparator. A higher confinement factor should give a lower threshold current, which is an advantage for both the higher powers necessary for a faster write speed, and in portable, battery power applications, both commercially very important. A higher confinement factor, however, decreases the spot size, increasing the power density at the facet and potentially increasing the predisposition to catastrophic optical mirror damage (COMD), albeit at much higher powers than used in normal operation, which would decrease the lifetime of consumer electronics.

The mode expanded structure has a slightly more complex layer structure than the comparison design. A good design is stable with respect to small changes in layer thicknesses and compositions and can be manufactured reproducibly. I investigated this by modelling the effect of changes in layer thickness and composition, and by experimental characterisation of repeated growths.

In this chapter I discuss these main strands. Firstly I compare threshold current and farfield performance of the mode expanded structure and the more conventional design. I then describe

modelling of stability and characterisation of repeated growths. Some modelling of the susceptibility to COMD is also described in this chapter, but the full experimental investigation of this is described in the next chapter.

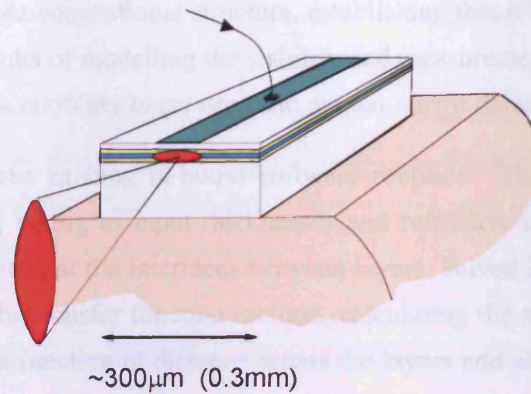


FIGURE 3.1: An oxide stripe laser showing a typical beam shape with a large vertical farfield

The strong confinement of the optical mode in the epitaxial layers leads to a wide divergence in the direction perpendicular to the layers (vertical). (Figure 3.1). The direction parallel to the layers (lateral) where the confinement depends on the structure used, for example ridge or gain-guided oxide isolated stripe in a broad area high power laser, tends to have a small divergence in the farfield of typically 6-8 degrees. This disparity, the astigmatism of the beam, provides challenges in applications and ideally the vertical divergence would be reduced to match the lateral divergence, producing a beam as close as possible to circular. To reduce the vertical farfield angle the nearfield width must be increased. This can be achieved in a variety of ways and many different designs have been proposed. The mode expanded structure works by the inclusion of extra high index layers in the otherwise low refractive index cladding layers which spread the optical mode further into the cladding layers, reducing the far field divergence. However, because the shape of the electric field amplitude is changed in a way which produces an insignificant change in the square of the amplitude at the centre of the waveguide, where the quantum wells are placed, this spreading of optical mode can be achieved with an almost imperceptible reduction in the optical intensity and hence minimal decrease in the optical confinement factor (Γ), in contrast to other designs. A reduction in Γ would result in increased threshold current density, exacerbating any heating problems and carrier loss, important at this wavelength. This process is effective because it is the optical intensity that determines the optical confinement factor whereas the amplitude determines the farfield distribution.

It has previously been shown that such a design can be used to reduce the vertical farfield divergence from 35 to 24 degrees [55] without changing the threshold current density. In the present structure the divergence is reduced to a value of about 18 degrees and another design was produced with a very narrow farfield of about 13 degrees.

In this chapter I describe the quantum well and, briefly, the quantum dot structures, which are the subject of a separate ongoing research program, therefore detailed consideration of these is outside the scope of this thesis. I will then compare the performance of the mode expanded design with that of a more conventional structure, establishing that it has equally good or superior characteristics. Results of modelling the stability and measurements to confirm this follow. Lastly I consider the susceptibility to catastrophic optical mirror damage (COMD).

In modelling I used three existing in-house software routines. The first solved for the optical waveguide modes, taking as input thicknesses and refractive indices of layers and, applying boundary conditions at the interfaces between layers, solved Maxwell's equations self-consistently using the transfer function method, calculating the nearfield distribution (amplitude or intensity) as a function of distance across the layers and also the confinement factor in each layer. The calculation is similar to that carried out for a 3-slab waveguide but with as many as 25 or more layers in a more complex structure. The second took the nearfield amplitude calculated by the optical mode solver and performed a Fourier transform to obtain the farfield. I used this software to model the effect of changing the thicknesses and compositions of the layers of the mode-expanded structure to explore how far the design could be pushed in terms of narrowing the farfield, and whether extreme designs led to instability that would result in a badly performing waveguide if standard manufacturing tolerances were not strictly applied. The third was a quantum well solver which used the thickness and composition of the quantum well layers to predict electron to light hole and electron to heavy hole transitions, necessary for the design of a quantum well based active region, and was used to check combinations of layer thickness and composition giving the same transition energy.

I examined the sensitivity of the farfield to potential variations in layer thickness and composition, establishing how big a farfield change would be caused by layer thickness and composition changes of the order of manufacturing tolerances. I then considered the effects of using either a symmetrical design or a design with mode expansion layers on one side only.

3.2 Quantum well structures

All the devices emitted in the red/NIR region and were fabricated in the InP/GaInP/AlGaInP material system. The two main QW structures used in the comparison of structures were a commercial design and our mode expanded design, chosen for their very different spot sizes: (0.51 μm and 0.37 μm) although both had the same narrow farfield of about 18° FWHM [56]. In the COMD studies the structure compared with the mode expanded design was a similar commercial DVD design, but with a step in the refractive index in the n-doped side, designed to pull the mode out of the p-doped region, but with similar confinement factor (0.54 m) and performance. The active regions of all three structures consisted of three 5 nm compressively strained

GaInP QWs separated by 5.5 nm $(\text{Al}_{0.5}\text{Ga}_{0.5})\text{InP}$ (lattice matched) barriers in $(\text{Al}_{0.7}\text{Ga}_{0.3})\text{InP}$ waveguides (figure 3.2) and were designed to produce TE polarised radiation. All structures emitted in the 650-660 nm band, depending on device length and pumping level. The refractive indices and bandgaps of the core and cladding layers are controlled by adjusting the percentage of aluminium according to the relations listed in reference [57] and standard compositions of $(\text{Al}_{0.50}\text{Ga}_{0.50})_{0.51}\text{In}_{0.49}\text{P}$ in the barriers / waveguide core and $(\text{Al}_{0.70}\text{Ga}_{0.30})_{0.51}\text{In}_{0.49}\text{P}$ for the cladding layers were used. The wafers were grown on (100) substrates angled 10° towards the [111] direction to prevent ordering in the AlGaInP layers. The comparator structure (12-45) was grown with two different p-dopants, Mg and Zn.

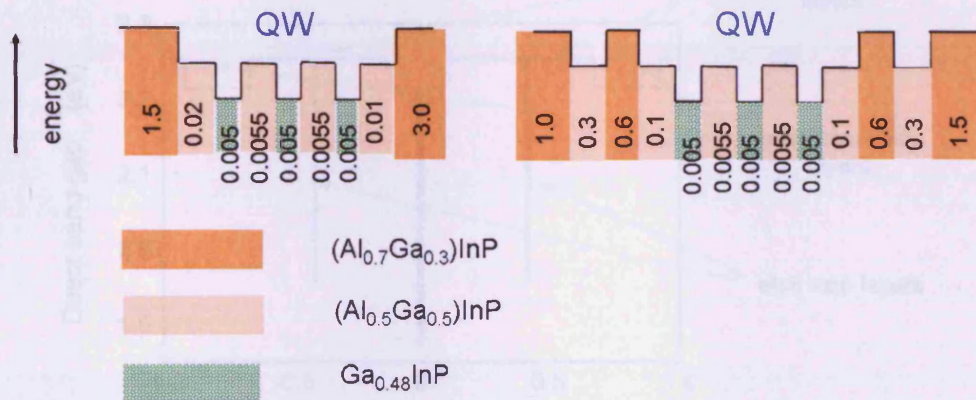


FIGURE 3.2: Schematic bandgap, layer thickness and composition of QW devices used in COMD experiments. Both these structures have three compressively strained GaInP QW with AlGaInP waveguides and barriers. Dimensions shown on the diagram are in μm . The left hand structure has a spot size of $0.541\mu\text{m}$ and the right hand one has a spot size of $0.373\mu\text{m}$. The structures operated at wavelengths of between 650 and 660 nm. The p-side is on the left of the figure

I calculated the refractive indices using the Modified Single Electron Oscillator [58] (MSEO) method and the direct band gap using the Model Solid Theory [47] for the narrow farfield mode expanded structure. (Figure 3.3). Model Solid Theory calculates the conduction and valence band edge positions of isolated materials on an absolute energy scale, taking the effects of strain into account. Our quantum well structures had compressively strained quantum wells. The lasing photon energy is a function of device length and internal loss, as well as being determined by the bandgap. The MSEO method enables refractive index to be calculated in terms of the photon energy and band gap, which is affected by composition.

The optical mode is confined by the waveguide structure which consists of a higher refractive index core in lower refractive index cladding layers. Recombination of carriers with the emission of photons takes place in the quantum wells which are at the centre of the waveguide, where the optical mode is a maximum. This, together with the width of the wells affect the value of confinement factor (Γ) and hence pumping requirement. In short wavelength AlGaInP-based lasers any increase in the optical gain requirement causes an increase in the temperature sensitivity of

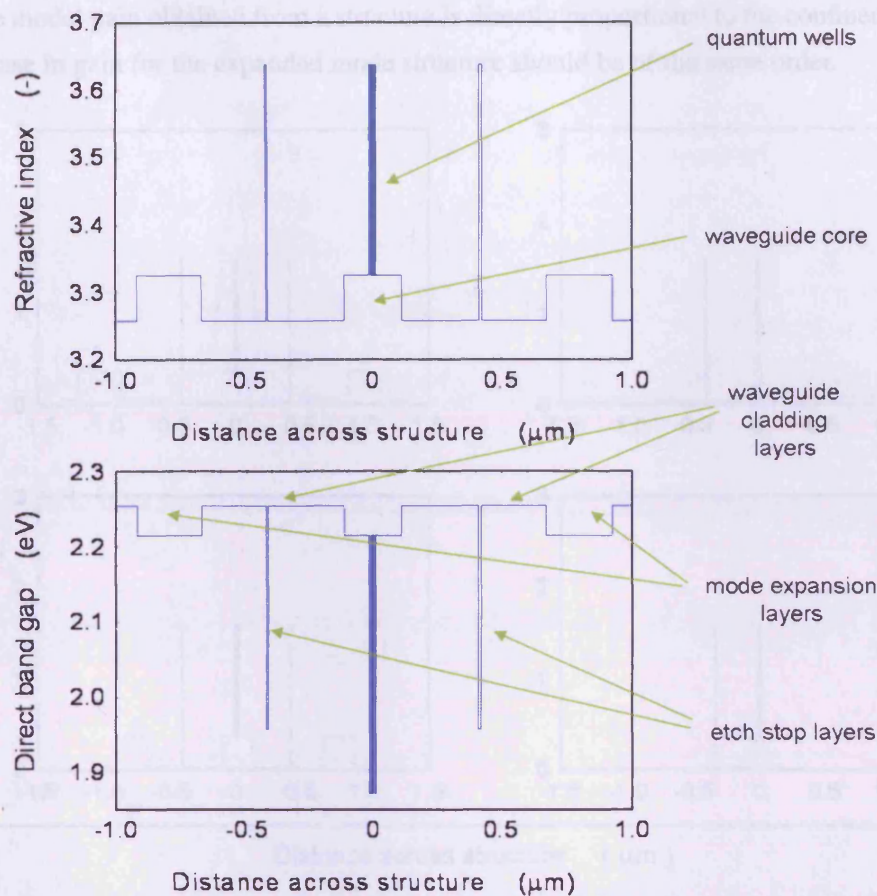


FIGURE 3.3: (top) Calculated refractive indices (using the MSEO method) and (bottom) calculated direct band gap (using model solid method) for the narrow farfield mode expanded structure. The main features of the structure are identified

threshold current, as well as an increase in the current itself, since the device must be pumped harder, which in turn leads to more heating and carrier leakage.

An extra feature in this structure (figure 3.3) is the mode expansion layers which are inserted in the low refractive index cladding layers. The optical mode is pulled out into these higher index layers, thus broadening the nearfield and narrowing the farfield. Also shown are the etch stop layers, a design requirement for commercial structures, and placed on both sides of the structure to maintain the symmetry and increase stability with respect to growth fluctuations. I found it necessary to include these in the modelling as the presence of these layers affected the profile of the optical mode slightly and resulted in visible effects at COMD.

In figure 3.4 the calculated normalised (total power across structure is equal to 1) profiles of the nearfield intensities are presented along with a schematic indication of the refractive indices of the epitaxial layers for both structures. The nearfield scales are the same for both structures: thus it may be seen that the intensity in the centre of the nearfield at the quantum wells in the expanded mode structure is greater than that of the comparator structure, by a factor of 1.34.

Since the modal gain obtained from a structure is directly proportional to the confinement factor the increase in gain for the expanded mode structure should be of the same order.

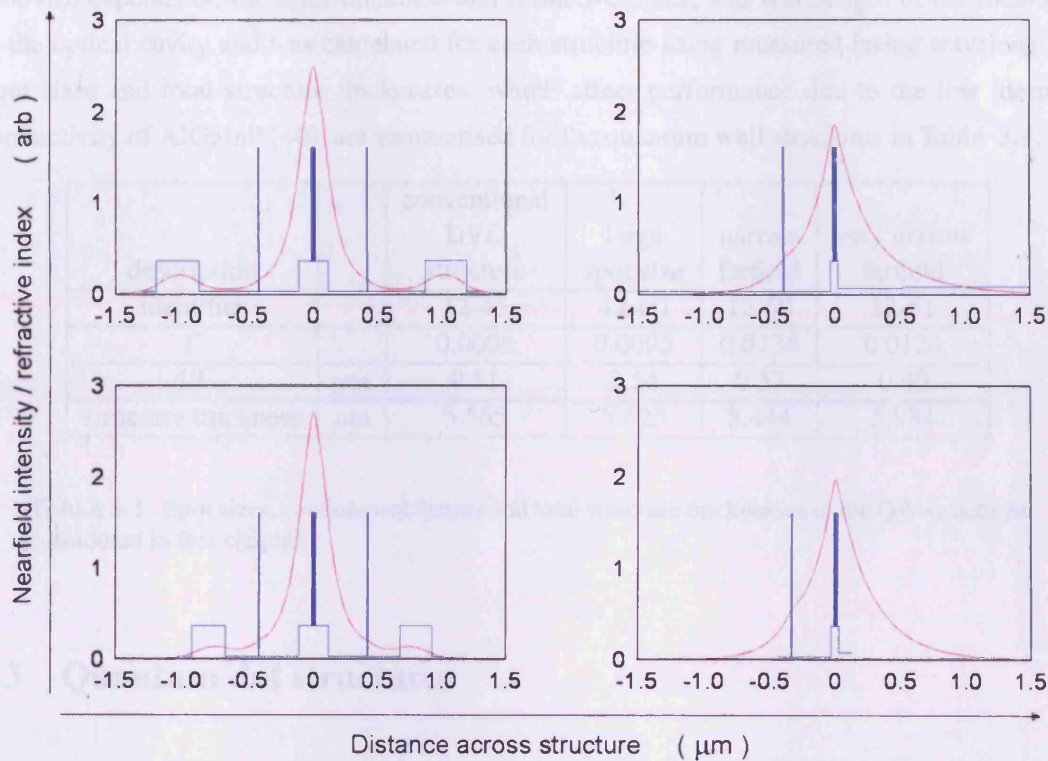


FIGURE 3.4: Calculated profiles of the nearfield intensities (normalised so that the area under the curve (total power) is unity) and schematic indication of the refractive indices of the epitaxial layer structure. The scales are the same for all diagrams. (left) The mode expanded structures: top: very narrow farfield and bottom: narrow farfield designs. (right) Comparison standard DVD designs for COMD studies (top) and DVD structure performance (bottom). The mode expanded structures clearly show a greater intensity at the quantum wells than the standard DVD designs.

The mode expansion layers spread the mode more widely in the structure into two side lobes. This concentration of optical energy in these layers, with a lower intensity region in the cladding layer between the mode expansion layer and the core, keeps the intensity and the confinement factor high at the quantum wells. These regions of higher amplitude transform into measurable lobes at the sides of the farfield. The large intensity within the confinement layers means that lasers must be designed carefully with etch stop layers being positioned according to the ridge width required.

The position and width of the mode expansion layers controls the width of the farfield. To obtain the very narrow farfield design the mode expansions layers were widened and moved further away from the core.

I calculated the spot size for each structure from the relation

$$\text{spotsize} = d/\Gamma \quad (3.1)$$

where d is the well width in μm and Γ is the confinement factor, which is defined for a given layer as the fraction of light intensity confined in that layer, and is calculated in the program. The spot size depends on the layer thickness and refractive index, and wavelength of the radiation in the optical cavity and was calculated for each structure using measured lasing wavelengths. Spot sizes and total structure thicknesses, which affect performance due to the low thermal conductivity of AlGaInP [40], are summarised for the quantum well structures in Table 3.1.

description		conventional DVD structure	large spot size	narrow farfield	very narrow farfield
identifier		12-45	12-60	12-50	12-51
Γ		0.0098	0.0093	0.0134	0.0124
d/Γ	μm	0.51	0.54	0.37	0.40
structure thickness	μm	5.565	5.625	5.444	5.984

TABLE 3.1: Spot sizes, confinement factors and total structure thicknesses of the QW structures considered in this chapter

3.3 Quantum dot structures

The QD structures consist of 5 layers of quantum dots formed from 2 or 2.5 monolayers of InP grown on 8 nm (2321), 16 nm (2522 and 2323) $(\text{Al}_{0.3}\text{Ga}_{0.7})_{0.51}\text{In}_{0.49}\text{P}$ barrier layers covered by 8 nm $\text{Ga}_{0.51}\text{In}_{0.49}\text{P}$ quantum wells. (Figure 3.5 and Table 3.2). The outer waveguide consists of AlInP except for the p-doped structure where the aluminium ratios in the core and outer waveguide layers were 30/70. The quantum dot structures all emitted between 711 nm and 735 nm. These are experimental structures, still in the process of development. The structural details have been included here for completeness: further discussion of these structures will take place in the next chapter.

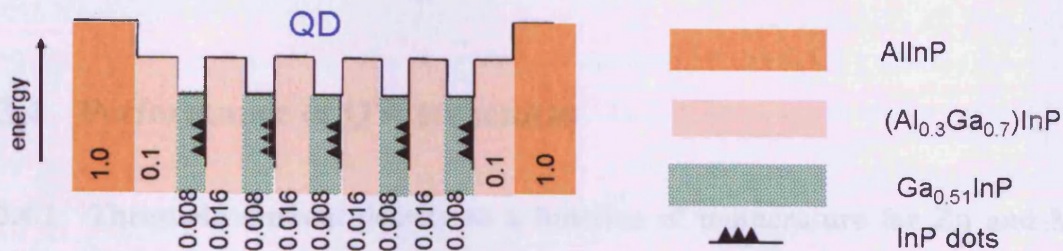


FIGURE 3.5: Schematic bandgap and layer thickness and composition of a typical QD structure, consisting of 5 layers of InP self assembled quantum dots in 8 nm GaInP quantum wells separated by 8 nm or 16 nm $\text{Al}_{0.3}\text{Ga}_{0.7}\text{InP}$ spacer layers, in AlInP cladding layers. Dimensions on the figure are in μm . The structures emitted between 711 and 735 nm.

identifier		2321	2323	2522
		8 nm spacer	16 nm spacer	16 nm spacer
growth temperature	K	750	730	710
no of monolayers		2	2	2.5
d/ Γ	μm	0.51	0.54	0.37
structure thickness	μm	5.565	5.625	5.444

TABLE 3.2: Spot sizes, growth details and total structure thicknesses of the QD structures considered in this chapter

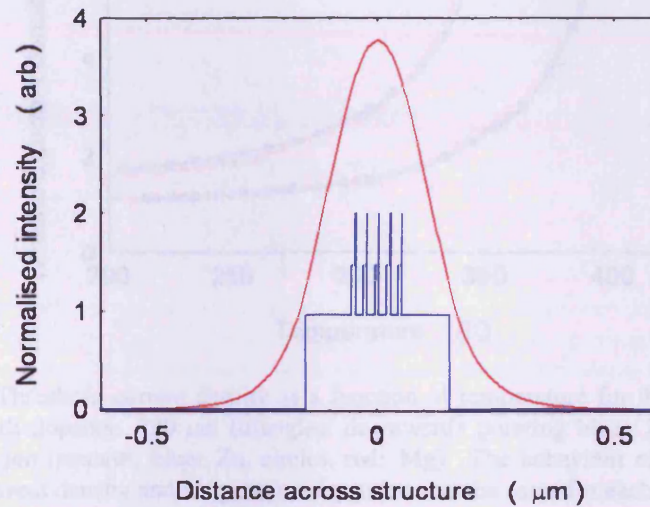


FIGURE 3.6: Calculated profile of the nearfield intensity for a QD structure (normalised so that the area under the curve (total power) is unity) and schematic indication of the refractive indices of the epitaxial layer structure. The vertical scale is higher, and the horizontal, narrower than figure 3.4 for the QW structure (figure 3.4). The intensities and confinement factors are higher than for the QW structures, leading to a narrower nearfield and wider farfield

The intensities and confinement factors are higher in these QD research structures than for the QW structures, leading to a narrower nearfield and wider farfield. (Figure 3.6). The farfield of these QD structures was about 45 degrees FWHM.

3.4 Performance of QW structures

3.4.1 Threshold current density as a function of temperature for Zn and Mg doped samples

I used laser data to examine the effect of using the different dopants on device performance, measuring threshold current density as a function of temperature using 50 μm wide, oxide isolated stripe lasers. The facets were as-cleaved. The devices were mounted n-side down on copper heat sinks attached to transistor headers and were operated pulsed at 1 kHz 0.04% duty

cycle to avoid self heating. Operating temperature was controlled in a cryostat and light-current characteristics were obtained between 200 K and 400 K. Examples of threshold current density as a function of temperature are plotted in figure 3.7 for one device each of lengths $320\ \mu\text{m}$ and $1000\ \mu\text{m}$ for both dopant types, out of 4 devices measured of each type and length.

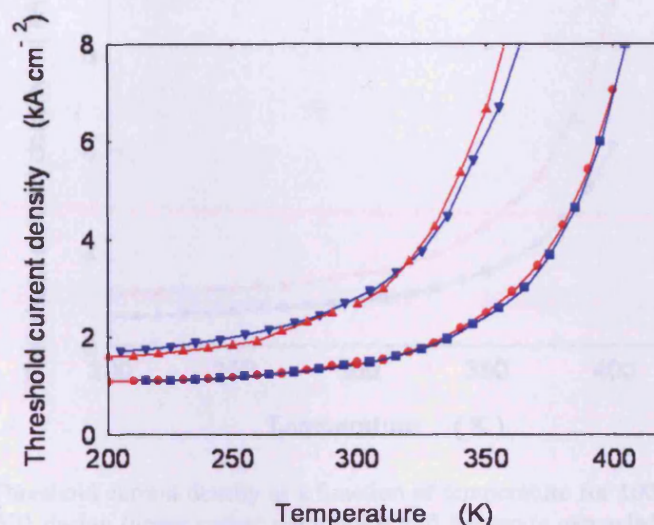


FIGURE 3.7: Threshold current density as a function of temperature for the standard DVD structure in both dopants: $320\ \mu\text{m}$ (triangles, downwards pointing blue: Zn, upwards red: Mg) and $1000\ \mu\text{m}$ (squares, blue: Zn, circles, red: Mg). The behaviour of both magnitude of threshold current density and temperature dependence is the same for each dopant

For both lengths of device the threshold current is identical, apart from slight experimental scatter, for the Zn and Mg doped structures over the whole temperature range, which was extended specially to 400 K for this measurement. The difference in dopant has not affected the performance even for the shorter devices operated up to high temperatures where a significant fraction of the recombination is likely to be due to thermally activated leakage, which is particularly sensitive to the p-doping. The temperature sensitivity can be characterised in terms of T_0 and I obtained a value of T_0 of about 86 K over the range $20\ ^\circ\text{C}$ to $70\ ^\circ\text{C}$ for $1000\ \mu\text{m}$ long devices with either Mg or Zn dopant. Having established that Mg or Zn doping can be used without any adverse affects Mg was used for a comparison of the standard and mode expanded structures. Both sets of devices lased at $649\ \text{nm}$ for $320\ \mu\text{m}$ devices, again confirming similar performance.

3.4.2 Comparison of threshold characteristics of the mode expanded and standard DVD designs

To compare the performance of the mode expanded and standard structures I again measured threshold current density as a function of temperature using oxide isolated stripe lasers. The threshold current density of $1000\ \mu\text{m}$ long devices is plotted as a function of temperature for the two structures in figure 3.8. The threshold current density for the mode expanded structure is

lower over the whole temperature range and is approximately 60% of the value of that of the standard commercial structure at 300 K.

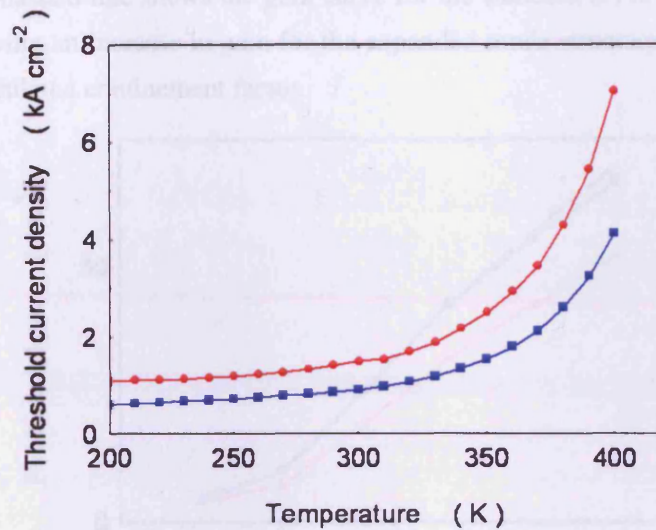


FIGURE 3.8: Threshold current density as a function of temperature for 1000 μm devices for the standard DVD design (upper curve: red circles) and the mode expanded structure (lower curve: blue squares). The threshold current density is significantly lower for the expanded mode design

I measured values of T_o over the range 20 °C to 70 °C for both structures, which showed an improvement for the expanded mode structure at short device lengths. (Table 3.3).

device length (μm)	320	1000
mode expanded structure: T_o (K)	65	88
standard structure: T_o (K)	51	86

TABLE 3.3: Values of T_o over the range 20°C to 70°C for the expanded mode structure and the standard structure for two lengths of device, showing improved performance for short devices which are more sensitive to thermal leakage

The improved performance of the mode expanded structure is consistent with the higher confinement factor which allows the threshold gain to be reached at a lower current density. Lower pump currents will reduce the carrier leakage, which is particularly sensitive to temperature in this material system, leading to the lower threshold current and higher T_o observed. I also measured lasing wavelengths and found these to be 649 nm for the commercial structure and 652 nm for the expanded mode structure for lasers of length 320 μm , at 1.05 times threshold current at 300 K, corresponding to a lower pumping requirement for the mode expanded structure. Lower carrier density or ΔE_f means less band filling and a longer operating wavelength.

I measured the modal gain of the two structures as a function of wavelength for a range of currents at 300 K using the multisection technique. The modelled value of the confinement factor was 1.34 times higher for the expanded mode structure. The peak gain is plotted as a

function of current density in figure 3.9 for the two structures. The upper curve shows gain as a function of current for the new expanded mode design and clearly shows much larger values of gain. The grey dashed line shows the gain curve for the standard DVD structure multiplied by 1.34, thus showing an increase in gain for the expanded mode structure consistent with the increase in the calculated confinement factor.

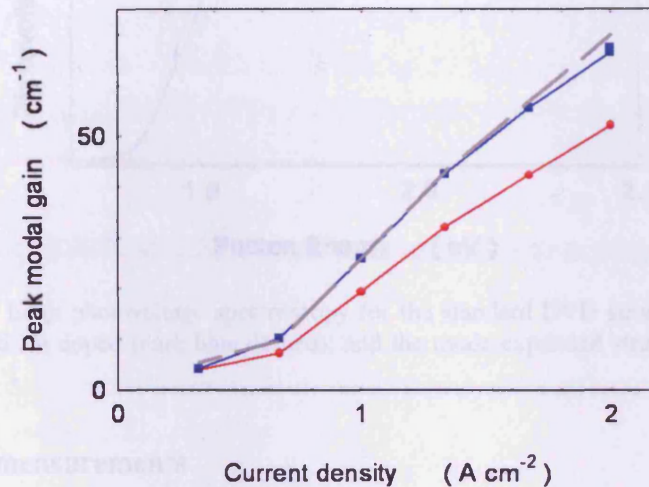


FIGURE 3.9: Modal gain as a function of pumping current density for the mode expanded structure (upper curve, blue squares) and the standard DVD structure (lower curve, red spots). The grey dashed line is the lower curve multiplied by 1.34, the ratio of the confinement factors

3.4.3 Edge photovoltage spectroscopy (EPVS)

Edge photovoltage spectroscopy (EPVS) can be used to check the layer thickness and composition of the quantum wells by relating the position and separation of the exciton peaks with transitions predicted using Model Solid Theory, taking into account material composition, strain and quantum effects. Differences between wafers in these properties could affect the values measured for comparison. For example a change in composition, reducing the bandgap and band offset, could be compensated for by a thinner QW, which would increase the thermal leakage out of the well, especially for short device lengths. This would affect the performance of the material at high temperatures. I measured spectra for the three wafers compared (Figure 3.10) and found broad similarity between the structures, although the positions of the exciton peaks could not be resolved with sufficient precision to provide information about well width and composition separately, as the same transition wavelength can be obtained with a range of combinations of well width and composition.

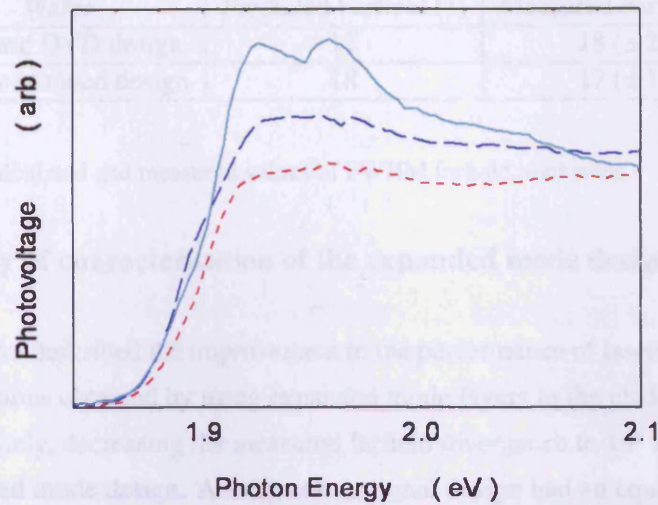


FIGURE 3.10: Edge photovoltage spectroscopy for the standard DVD structure: Mg doped (red dotted) and Zn doped (dark blue dashed), and the mode expanded structure (light blue, solid)

3.4.4 Farfield measurements

The farfield diverges most widely in the transverse direction, perpendicular to the growth plane, which is affected by the layer structure and therefore by the design of the wafer. I measured and calculated the farfield intensity distributions, which are shown in figure 3.11 and show good general agreement in terms of shape. The measured and calculated FWHM farfield intensities for the two structures are listed in table 3.4. There is good agreement between the calculated and measured values of the FWHM intensity.

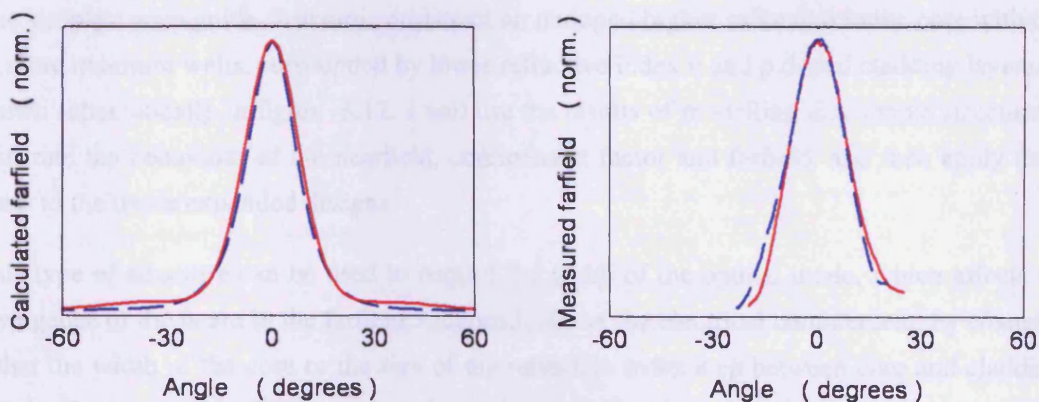


FIGURE 3.11: Calculated and measured farfield intensities for the standard DVD and mode expanded structures showing good agreement. These measurements were made using the standard technique of projection onto a flat screen which is not able to display features at low intensities such as the side-lobes. (An apparatus constructed later resolved this problem.)

Wafer	Predicted Farfield (°)	Measured Farfield (°)
Standard DVD design	17	18 (± 2)
Mode expanded design	18	17 (± 1)

TABLE 3.4: Calculated and measured values of FWHM farfield intensities

3.4.5 Summary of characterisation of the expanded mode design

In this section I have described the improvement in the performance of lasers designed for DVD read/write applications obtained by using expanded mode layers in the cladding layer to spread the mode more widely, decreasing the measured farfield divergence to 18° FWHM from 24° in a previous expanded mode design. A more conventional design had an equally narrow farfield, but achieved this at the expense of decreasing the confinement factor, which resulted in higher threshold currents. Having established the evidence for the improvements in the design I will now show how modelling predicts its stability with respect to variations in growth parameters and will confirm these calculations with measurements.

3.5 Modelling of the stability of the mode expanded design

3.5.1 Large optical cavity - modelling a basic waveguide for optimal performance

Many different designs of waveguide have been tried for reducing the farfield divergence of separate confinement double heterostructure (SCDH) quantum well lasers and the efforts continue. The simplest waveguide structure consists of an undoped higher refractive index core with one or more quantum wells, surrounded by lower refractive index n and p doped cladding layers, as shown schematically in figure 3.12. I will use the results of modelling this simple structure to illustrate the behaviour of the nearfield, confinement factor and farfield, and then apply these ideas to the mode expanded designs.

This type of structure can be used to control the width of the optical mode, which affects the divergence of the beam in the farfield, independently of the electrical confinement, by changing either the width of the core or the size of the refractive index step between core and cladding. Originally proposed by Lockwood et alia [59] and further discussed by Thompson et alia [60] in AlGaAs: the *Large Optical Cavity* (LOC) designs have been investigated for various material systems including AlGaInP [61, 62]. The layer widths and refractive indices affect the amplitude of the electric field of the optical mode across the epitaxial layers (the nearfield), the intensity of the radiation in the emitted beam as a function of angle (the farfield) and the fraction of the optical intensity, proportional to the square of the electric field amplitude, confined in the quantum wells (the confinement factor). To illustrate the relationship between the nearfield,

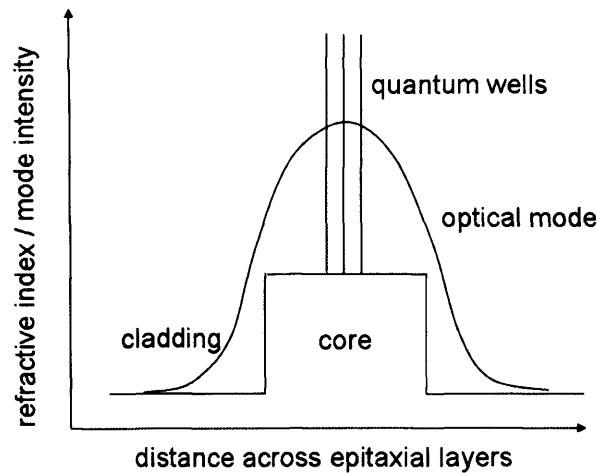


FIGURE 3.12: Basic SCDH laser structure showing the relative refractive indices of the layers (not to scale)

farfield and confinement factor in a simple structure I modelled these as a function of the width of the core, keeping the refractive index step constant (using values suitable for a 650 nm band emitter with $\text{Al}_{0.5}\text{GaInP}$ core and $\text{Al}_{0.7}\text{GaInP}$ cladding). (Figure 3.13). A feature that is built into the design of structures to be grown is the requirement that only the lowest order mode be present. When varying structures for modelling purposes this constraint was not imposed, but only the lowest order mode solution was considered.

As the core is widened the width of the optical mode, or nearfield, decreases and then widens again. The farfield and confinement factor correspondingly increase to a maximum and then decrease again. (Figure 3.14). Both a high confinement factor (in order to obtain lower threshold currents) and narrow farfield are required but these requirements cannot be satisfied simultaneously for this design. An advantage of the wide core is that the percentage of the optical mode extending into the doped cladding layers decreases rapidly as the core becomes wider, which has two beneficial effects: lower values of optical mode loss (α_i) caused by free carrier absorption [61] in the cladding layers and the potential for making the cladding layers thinner [62] due to the reduced penetration of the mode into the lower bandgap and therefore strongly absorbing GaAs cap. The thermal and electrical resistivities of p-doped AlGaInP are large so making these layers thinner reduces the thermal conductivity problems associated with high power lasers [62].

As can be seen from figure 3.14 the farfield width and confinement factor increase and decrease together so any laser made from this structure has the disadvantage of a widely diverging beam or a high threshold current. The peaks on the graphs are not quite at the same position, however, so if a laser could be made with core widths of between $0.1 \mu\text{m}$ and $0.13 \mu\text{m}$ (indicated by the grey lines) quite large confinement factors of 0.0134 to 0.0146 with farfields of 22 to 25 degrees respectively would be obtained. These properties are changing rapidly with respect to thickness at these core thicknesses, however, so a standard variation in manufacturing tolerances

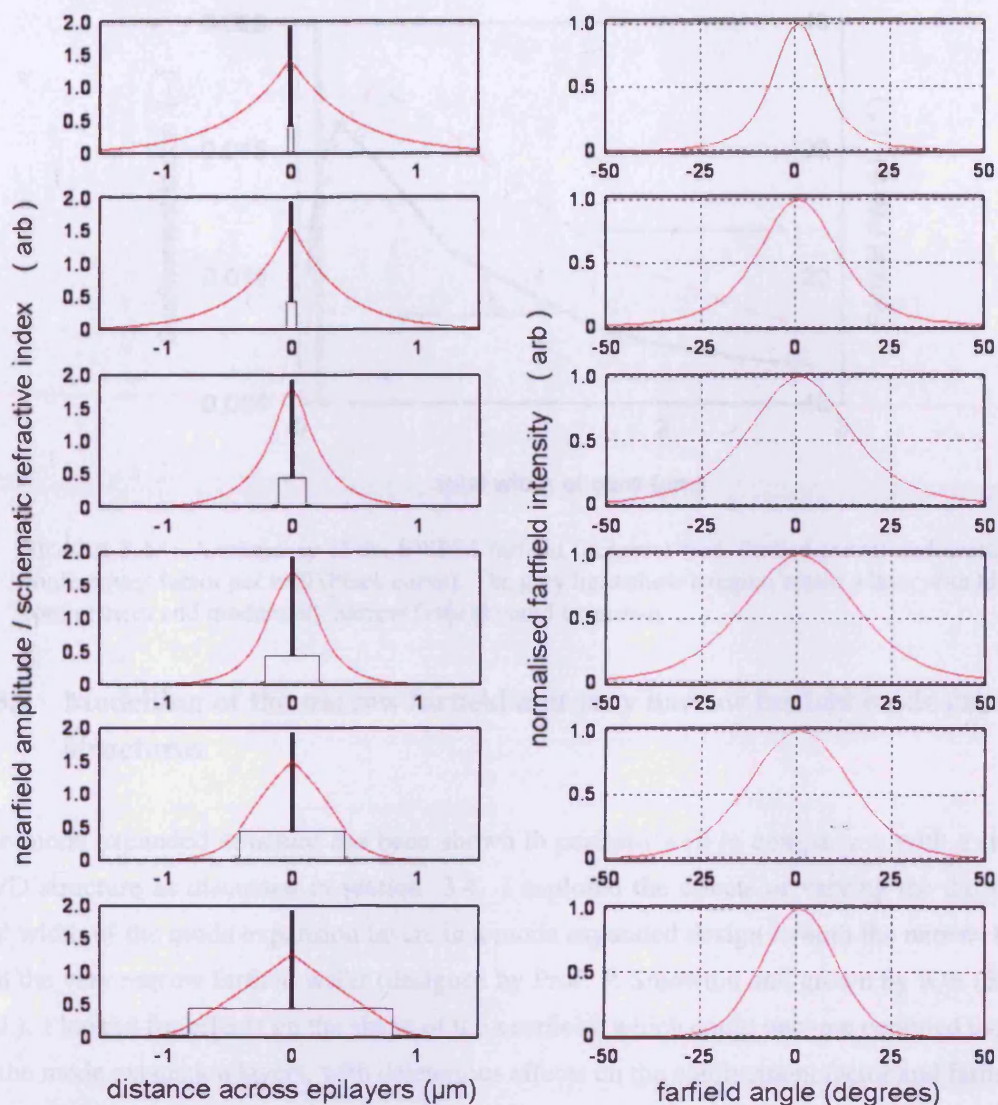


FIGURE 3.13: The nearfield amplitudes (left), with the waveguide shown schematically in black, and normalised farfield intensities (right) as the width of the core region increases from $0.046 \mu\text{m}$ to $1.626 \mu\text{m}$. As the core width increases the nearfield narrows, then widens again. The amplitude and confinement factor increase and then decrease and the farfield increases then decreases

would lead to a much greater variation in the properties of the manufactured laser than would be obtained if a much wider core had been used. A high power structure benefits from having thin layers so that thermal conductance is improved, but although the structure core is narrow, a narrow structure overall cannot be grown as the mode now extends widely outside the core into the cladding layers, which must be sufficiently wide to prevent appreciable penetration of the mode into the cap. These issues are now considered for the mode expanded structure.

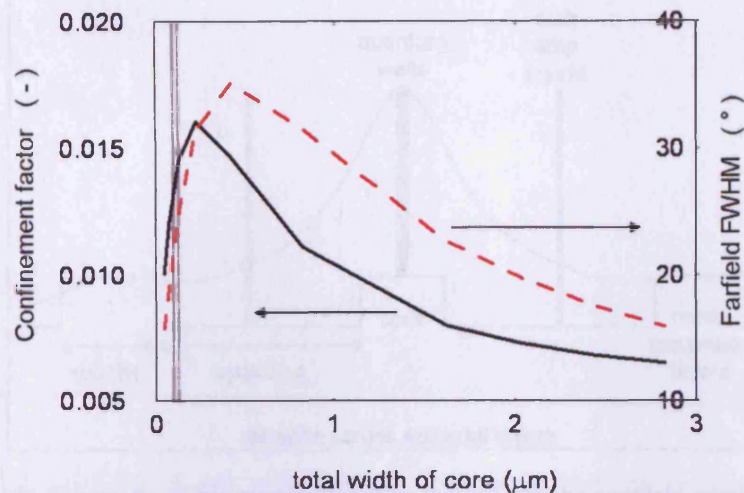


FIGURE 3.14: A summary of the FWHM farfield (degrees) (red, dashed curve) and average confinement factor per well (black curve). The grey lines show a region where a laser with high confinement and moderately narrow farfield could be grown

3.5.2 Modelling of the narrow farfield and very narrow farfield mode expanded structures

The mode expanded structure has been shown to perform well in comparison with a standard DVD structure as discussed in section 3.4. I explored the effects of varying the the spacing and width of the mode expansion layers in a mode expanded design in both the narrow farfield and the very narrow farfield wafer (designed by Prof. P. Smowton and grown by IQE (Europe) Ltd.). I looked for effects on the shape of the nearfield, which could become confined too much in the mode expansion layers, with deleterious effects on the confinement factor and farfield. To determine a point beyond which the design becomes more sensitive to small changes in growth conditions I used the rate of variation in the confinement factor and farfield (both FWHM and $1/e^2$, which includes most of the beam power). I then considered the effects of an asymmetric structure using a mode expansion layer on one side only. Finally I varied the layer thicknesses and aluminium percentages in both the narrow and very narrow farfield designs to simulate the effects of variability in growth conditions due to manufacturing tolerances.

The optical mode tends to be confined in layers of higher refractive index [53] as can be seen in figure 3.15. This results in pronounced lobes in the mode expansion layers (with a slight increase in the amplitude at the etch stop layers). In the narrow farfield structure the side lobes are pulled toward the core, slightly on one side of the mode expansion layer. This has the effect of pushing the lobes in the farfield out to greater angles. The nearfield intensities showing positions of the sidelobes in with respect to the mode expansion layers can be seen in figure 3.4.

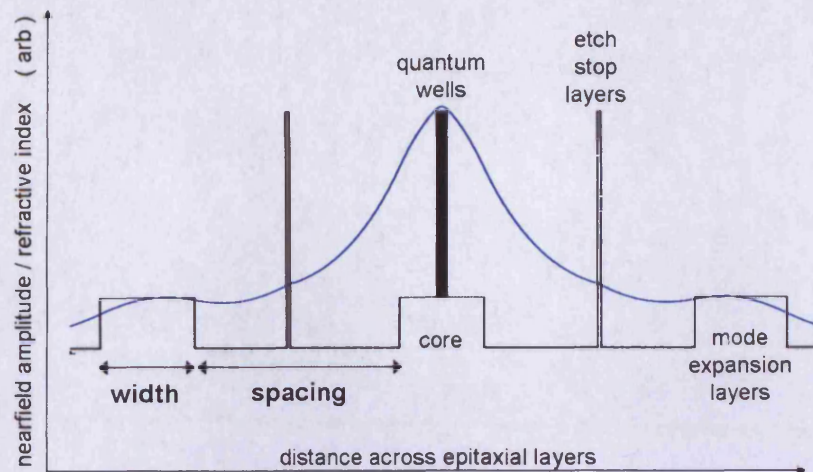


FIGURE 3.15: Schematic of Waveguide refractive indices and the nearfield amplitude for the narrow farfield structure showing definitions of the distances varied in modelling: width and spacing

In the very narrow farfield structure, the side-lobes in the nearfield have moved further from the core into the mode expansion layers, with the side lobes in the farfield at smaller angles (Figure 3.16). This is a consequence of the Fourier relationship between the nearfield and farfield.

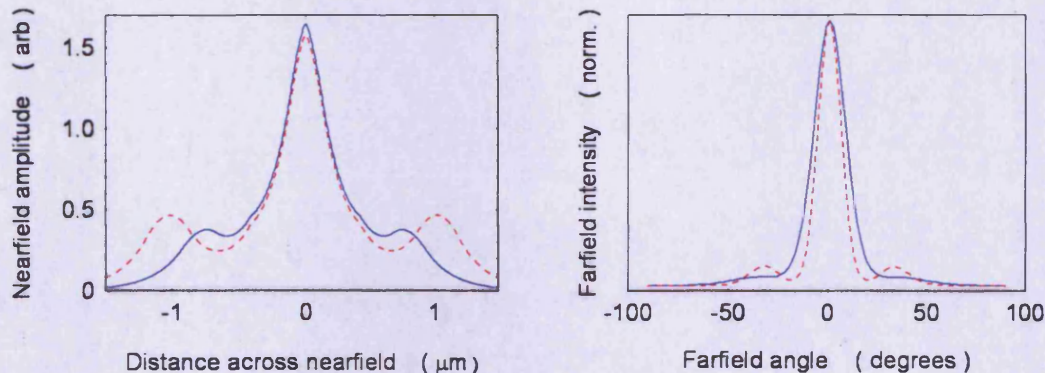


FIGURE 3.16: Calculated nearfields (left) and farfields (right) for the as-grown narrow farfield structure (blue curves) and very narrow farfield structure (red dashed curves). The Fourier relationship between the nearfield and farfield means a structure with more widely spaced lobes in the nearfield has a narrower farfield

I will now discuss the effects of varying the width of the mode expansion layers and the spacing between core and mode expansion layers on the mode shape, confinement factor and farfield, relating changes to the as-grown structures. (Table 3.5)

Taking the narrow farfield design as a starting point, I varied the spacing between the core and the 250 nm wide mode expansion layers. The structure as grown (shown by the vertical dashed line in figure 3.17) included etch stop layers for the purpose of manufacturing ridge waveguides in commercial applications. I found these made a significant difference to farfields and confinement factors and needed to be included in the modelling. The etch stop layers were kept

Wafer	thickness of mode expansion layer (nm)	position of mode expansion layer (nm)	predicted farfield ($^{\circ}$) FWHM ($1/e^2$)	confinement factor (-)
Narrow farfield	250	550	18.7 (33.7)	0.0134
Very narrow farfield	320	750	13.6 (23.3)	0.0124

TABLE 3.5: Positions and spacing of the mode expansion layers in the as-grown narrow farfield and very narrow farfield structures

at a constant distance from the core. The narrowest farfield that could be obtained by moving the mode expansion layers further from the core was 18.6° (FWHM) with a corresponding confinement factor of 0.0134. The amplitude of the nearfield side-lobes, and therefore their effectiveness at drawing the mode further from the core, decreased as their separation from the core increased. (Figure 3.17).

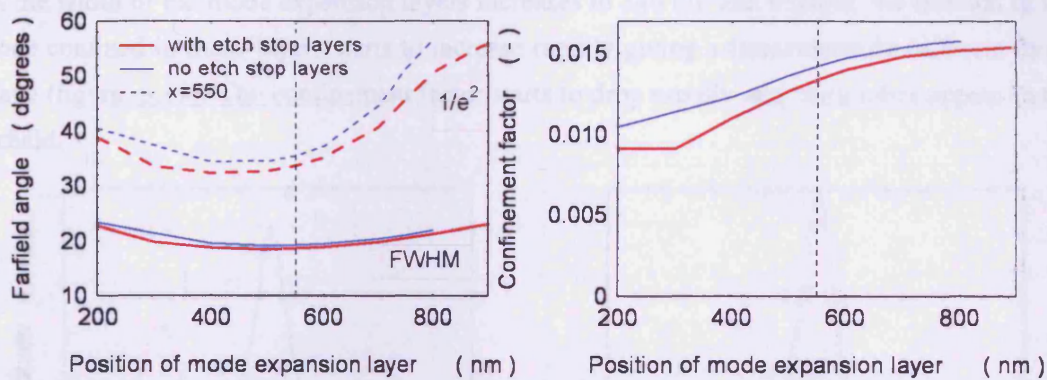


FIGURE 3.17: Comparison of the farfield FWHM and $1/e^2$ values (left) and the confinement factor (right) for the narrow farfield mode expanded structure, as a function of the spacing of a 250 nm wide mode expansion layer. The inclusion of the etch stop layer in the modelling makes a significant difference to the results.

To obtain a narrower farfield it was necessary to both increase the separation and increase the width of the mode expansion layer. Figure 3.18 shows the effect of varying the width of a mode expansion layer placed at 750 nm from the core in the very narrow farfield structure. The farfield angle decreased steadily until a width of about 340 nm and then started to increase again. The confinement factor remained high up to a 320 nm, but beyond this the confinement factor started to decrease rapidly with change in mode expansion layer thickness.

Figure 3.18 also illustrates the effect of using only one mode expansion layer, in an asymmetric structure. Not only were the farfields about five degrees wider, but also the design was less stable to variations: the confinement factor dropped more rapidly with respect to change in mode expansion layer width than in the symmetric structure.

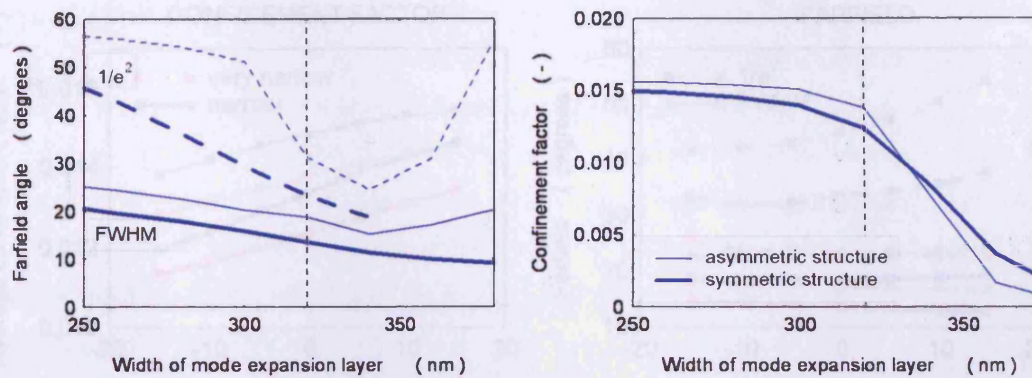


FIGURE 3.18: Comparison of the FWHM and $1/e^2$ farfields (left) and the confinement factor (right) for the very narrow farfield mode expanded structure (thick solid line), as a function of the thickness of a mode expansion layer placed 750 nm from the core. The data is repeated for an asymmetric structure with a mode expansion layer on one side only (thin lines). As well as a wider farfield the asymmetric structure shows lower stability than the symmetric structure with respect to variation of the mode expansion layer thickness

As the width of the mode expansion layers increases to 340 nm and beyond, the fraction of the mode confined in these layers starts to increase rapidly giving a fundamentally different mode shape (figure 3.19). The confinement factor starts to drop rapidly and extra lobes appear in the farfield.

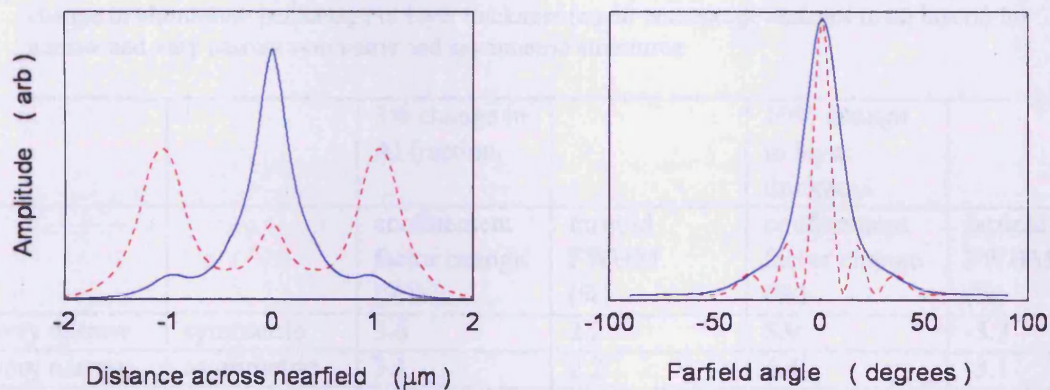


FIGURE 3.19: Examples of nearfield (left) and farfield (right) amplitudes for a 250 nm mode expansion layer (blue) and 380 nm mode expansion layer (red dashed) placed at 750 nm from the core. The amplitude and hence confinement factor at the wells drop rapidly as the confinement of the mode in the side-lobes increases at high mode expansion layer widths

I carried out a similar set of calculations for changes in the thickness of all layers, and changes in the aluminium percentages in all layers to simulate manufacturing tolerances. The results are given in figure 3.20 and summarised in table 3.6 for values typical of manufacturing tolerances.

I will now present the results of measurements on devices from repeated growths of the wafers over a period of a year and compare farfields, comparing these to the modelled values, threshold current (to compare confinement factors) between wafers and EPVS to confirm the compositions.

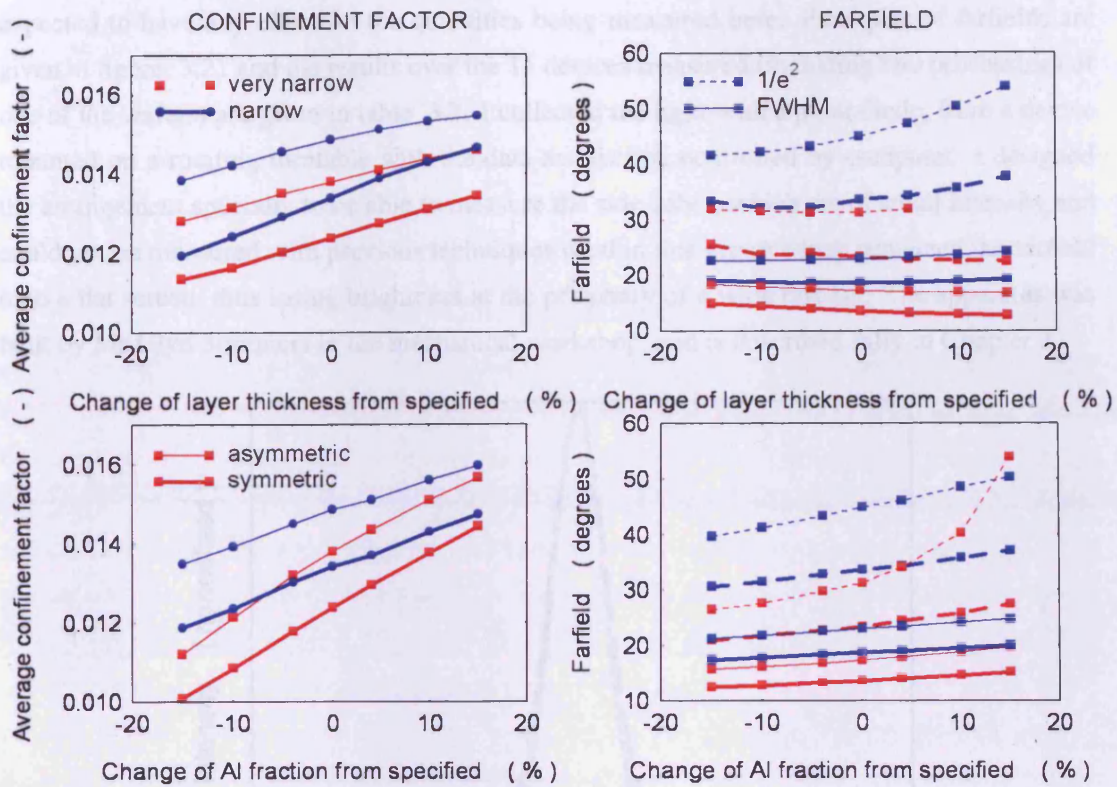


FIGURE 3.20: Change in FWHM and $1/e^2$ farfields and confinement factors as a functions of change in aluminium percentage or layer thickness (equal percentage changes in all layers) for narrow and very narrow symmetric and asymmetric structures

		3% change in Al fraction	10% change in layer thickness		
		confinement factor change (%)	farfield FWHM (%)	confinement factor change (%)	farfield FWHM (%)
very narrow	symmetric	3.6	2.2	5.9	-5.3
very narrow	asymmetric	3.1	2.2	4.4	-3.1
narrow	symmetric	1.9	1.3	7.0	0.4
narrow	asymmetric	0.3	1.5	3.7	2.3

TABLE 3.6: Values of percentage change in FWHM farfield and confinement factor for a 3% change in Al content in all layers or 10% change in layer thickness of all layers

3.6 Comparison of modelling and measurements of the mode expanded design

I measured the farfields at $1.2 \times$ threshold current for two devices each of two different lengths ($450 \mu\text{m}$ and $1000 \mu\text{m}$) from each of three narrow farfield wafers: two nominally identical (with Mg p dopant) and one with carbon as opposed to zinc doping in the cap layer, which is not

expected to have any effect on the quantities being measured here. Examples of farfields are given in figure 3.21 and the results over the 15 devices measured (including two processings of one of the wafers) are given in table 3.7. I collected the light with a photodiode, from a device mounted on a rotating turntable with the data acquisition controlled by computer. I designed the arrangement specially to be able to measure the side-lobes, which are of small intensity and could not be measured with previous techniques used in this group which projected the farfield onto a flat screen, thus losing brightness at the periphery of a wide farfield. The apparatus was built by Mr Glyn Summers in the mechanical workshop, and is described fully in Chapter 2.

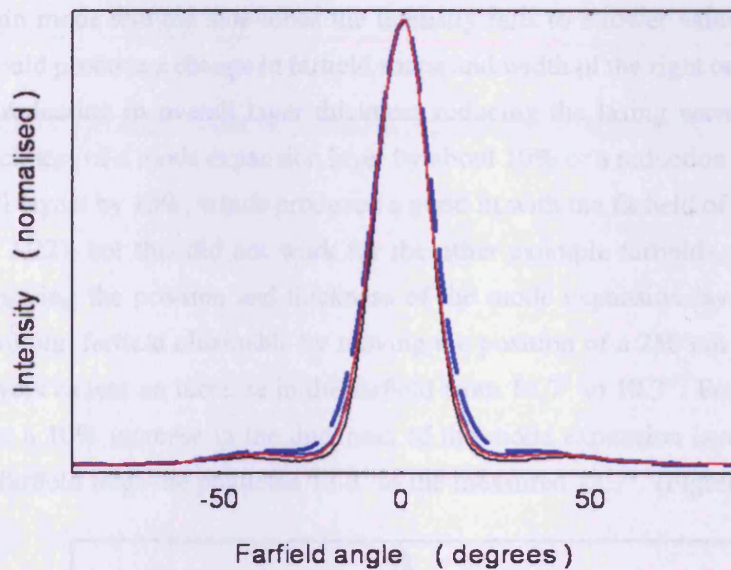


FIGURE 3.21: Examples of measured farfields of the narrow farfield structure for the three growths, from the 15 devices measured. The modelled farfield (thick blue dashed line) is broader than any of the measured farfields from three separate wafers

device length	1000 μm	450 μm	predicted
FWHM farfield	($^{\circ}$)	($^{\circ}$)	($^{\circ}$)
first growth, 1st processing	16.5 (\pm 0.03)	16.7 (\pm 0.06)	18.7
first growth, 2nd processing	17.1 (\pm 0.04)	17.9 (\pm 0.04)	18.7
second growth	17.4 (\pm 0.15)	17.5 (\pm 0.05)	18.7
third growth with C doped cap	17.4 (\pm 0.05)	17.0 (\pm 0.15)	18.7
device length	320 μm		
very narrow farfield FWHM	12.7 (\pm 0.09)		13.6

TABLE 3.7: Farfield measurements for the three growths of the narrow farfield structure measured over two device lengths at 1.2 x threshold current

There is a small amount of variability from device to device, from processing to processing and over the three wafers. There is no clear trend as a function of device length although shorter devices would need to be pumped harder. This would affect the lasing wavelength which affects the farfield, both directly and via the refractive index. For this reason all measurements for a

given length were made a fixed amount above the measured threshold for each device. The size of the experimental error (standard error in the mean) gives an indication of the quality of the measurement. I calculated the error over several measurements of the same device at the same orientation. A better measure of the error could be the variability between devices, separate realignments and processings. A value for the first growth narrow farfield would then be $17.2 (\pm 0.7)$ degrees. In terms of measured FWHM farfield there is agreement within error between the wafers, but all three are slightly smaller than the predicted farfield (18.7°), by about 1.5° .

As can be seen from figure 3.21, for the narrow farfield structure, the farfield is narrower, and between the main mode and the side-lobes the intensity falls to a lower value, than predicted. Changes that would produce a change in farfield shape and width of the right order of magnitude include a 10% reduction in overall layer thickness reducing the lasing wavelength by 5 nm, reducing the thickness of a mode expansion layer by about 10% or a reduction in the aluminium percentage of all layers by 15%, which produced a good fit with the farfield of the 12-50 second growth (figure 3.22), but this did not work for the other example farfields. From modelling summaries of varying the position and thickness of the mode expansion layers (figure 3.17) 18.7° is the minimum farfield obtainable by moving the position of a 250 nm layer. Removing the etch stop layers causes an increase in the farfield from 18.7° to 19.3° . For the very narrow farfield structure a 10% increase in the thickness of the mode expansion layers in produces a decrease in the farfield from the predicted 13.6° to the measured 12.7° . (Figure 3.23).

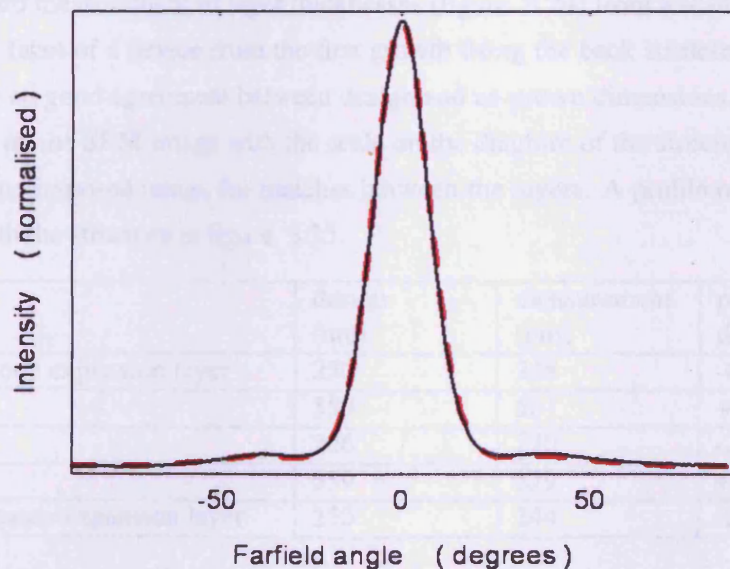


FIGURE 3.22: A reduction of 15% in aluminium composition in all layers produces a predicted farfield (red dashed) that agrees closely with a measured farfield from the second growth of the narrow farfield design (solid black)

These changes are at the furthest end of the manufacturing tolerance scale. Some variability in measured farfields is caused by changes in alignment or processing changes. Although some very good fits, for example figure 3.22, give confidence in the modelling method, the predicted

farfield width is stable to really quite large changes in parameters in this design. I will examine whether such large changes in the grown wafers could have occurred by using other types of measurement.

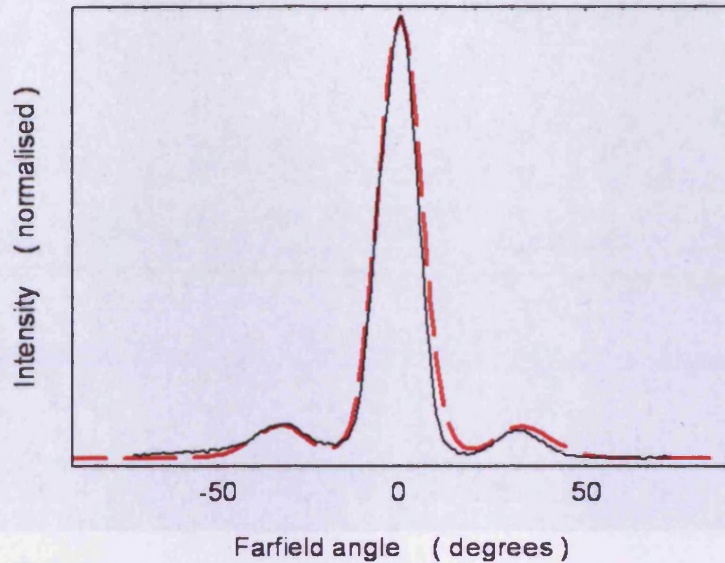


FIGURE 3.23: Measured (solid black) and modelled (red dashed) farfields for the very narrow farfield structure. The predicted and measured farfield (FWHM) were 13.6° and 12.7° respectively

A straightforward measurement of layer thicknesses (figure 3.24) from a scanning electron micrograph of the facet of a device from the first growth using the back scattered electron (BSE) technique, showed good agreement between design and as-grown dimensions. I matched accurately the scale on the SEM image with the scale on the diagram of the structure and looked on the resultant superimposed image for matches between the layers. A profile of the SEM image is compared with the structure in figure 3.25.

Layer	design (nm)	measurement (nm)	percentage difference
left hand mode expansion layer	250	248	-0.8%
spacing	559	561	+0.3%
core	226	220	-2.7%
spacing	559	579	+3.5%
right hand mode expansion layer	250	244	-2.4%

TABLE 3.8: Measurements from figure 3.25

Measurements of the profile taken from the SEM image (figure 3.24) given in table 3.8 show the percentage variation in layer thicknesses during growth is far smaller than would account for the difference in farfield. The three quantum wells were clearly visible and were used to align the centre of the structure, but their thicknesses could not be determined from this image.

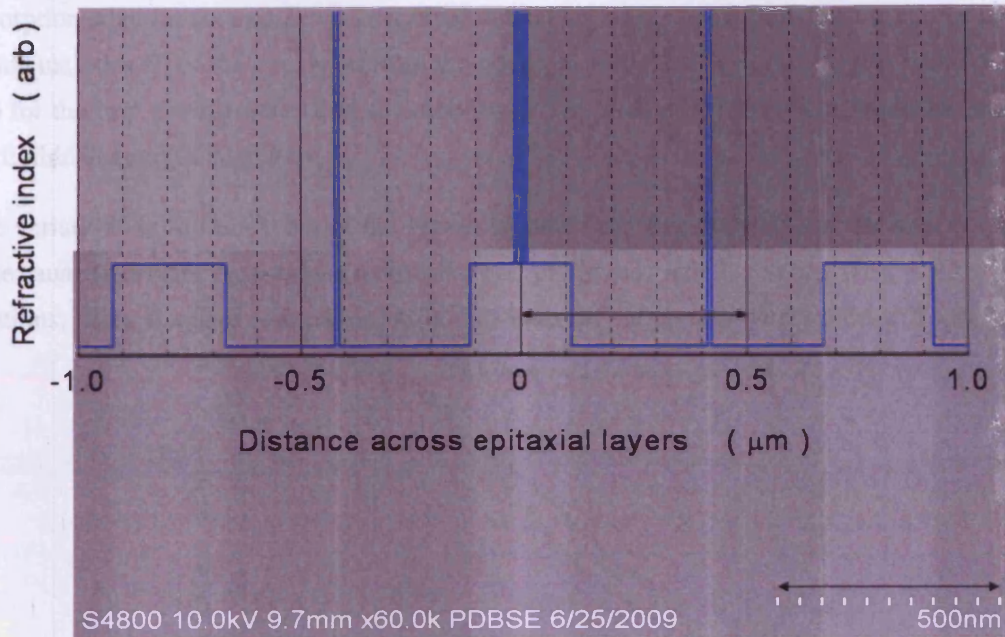


FIGURE 3.24: Scanning electron micrograph (SEM) of the facet of a device from the first growth using the back scattered electron (BSE) technique, accurately matched with a scale diagram of the structure, shows good agreement between design and as-grown dimensions as can be seen by arrows of equal length placed on each scale. The layers indicated in the structure can be clearly seen in the SEM image. (The SEM image was produced by Dr U. Zeimer of Ferdinand-Braun-Institut using an undamaged region of a device I had subjected to a high current pulse to study COMD)

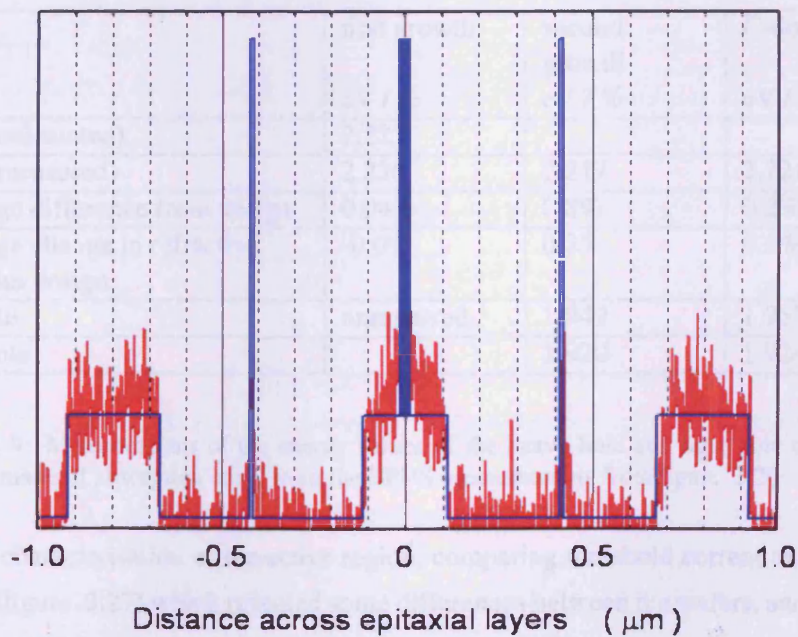


FIGURE 3.25: Profile of SEM image in figure 3.24 compared with structure

I used EPVS measurements to gain more information about the structure (figure 3.26). The absorption edge (at about 2.2 eV), measured at the half height of the step, for the barrier region, which includes all of the core apart from the quantum wells, has a slightly higher value of band gap for the first growth wafer than the other two. This will affect the refractive index, but to a negligible degree (table 3.9).

The variations in the thickness of the grown layers and refractive index of the core could not have caused the difference between observed and predicted farfields. I carried out further investigations, using standard techniques available within the group to look for other differences.

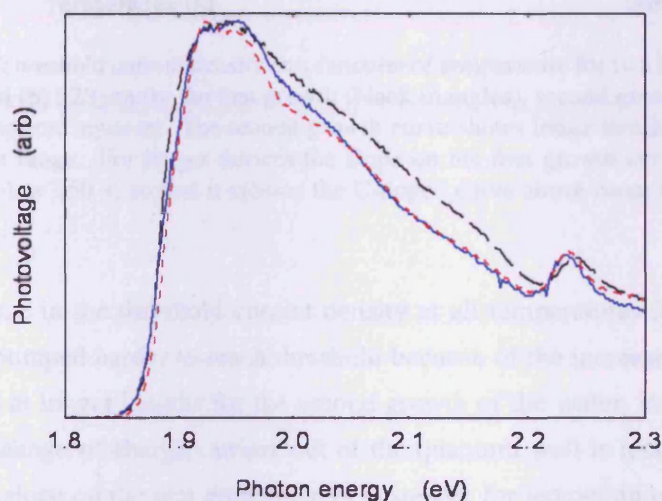


FIGURE 3.26: EPVS measurements of the three wafers (first growth black dashed, second growth blue solid and carbon doped cap red dotted)

	first growth eV / %	second growth eV / %	C-doped cap eV / %
Barrier (calculated)	2.225		
Barrier (measured)	2.226	2.217	2.221
percentage difference from design	0.04%	0.8%	0.2%
percentage change in refractive index from design	-0.0%	0.2%	0.1%
Light hole	unresolved	1.949	1.957
Heavy hole		1.920	1.924

TABLE 3.9: Measurements of the energy values of the heavy hole and light hole transitions and core material absorption edge, from the EPVS measurements from figure 3.26

I carried out characterisation of the active region, comparing threshold current as a function of temperature (figure 3.27) which revealed some differences between the wafers, and investigated these further with gain measurements.

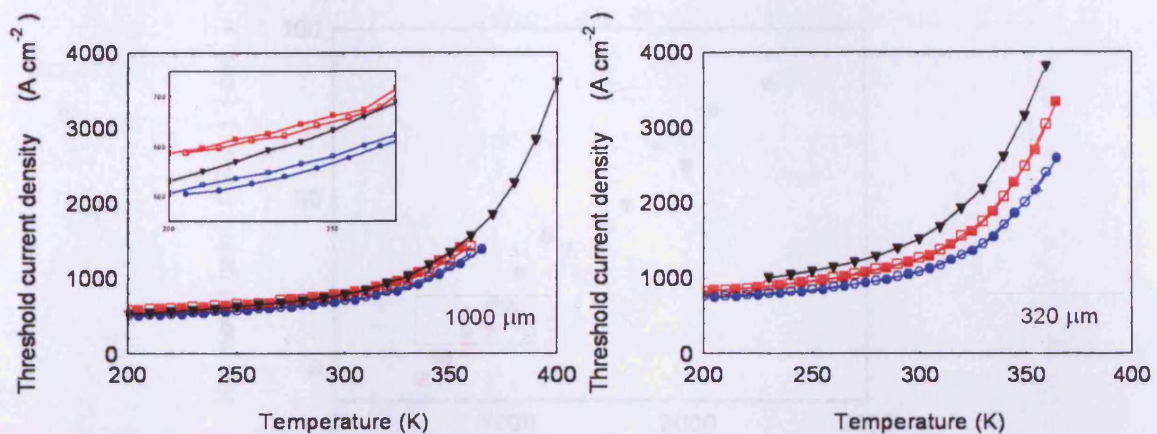


FIGURE 3.27: Threshold current density as a function of temperature for two lengths of device (a) $1000\ \mu\text{m}$ and (b) $320\ \mu\text{m}$ for the first growth (black triangles), second growth (blue circles) and C-doped cap (red squares). The second growth curve shows lower threshold current densities across the range. For longer devices the slope on the first growth curve is steeper for temperatures below 250 K so that it crosses the C-doped curve above room temperature (see detail)

There is a difference in the threshold current density at all temperatures for $320\ \mu\text{m}$ devices, which need to be pumped harder to reach threshold because of the increased mirror loss. This difference remains at longer lengths for the second growth of the wafer, including at low temperatures, when leakage of charge carriers out of the quantum well is less of a problem. For longer devices the slope on the first growth curve is steeper for temperatures below 250 K (see detail) so that it crosses the C-doped curve above room temperature. The second growth curve shows lower threshold current densities across the range. A larger confinement factor due to a wider well width could explain this difference. It is possible to obtain the same transition energy with a variety of combinations of well width and composition, and the specification controlling this, which is adjusted during growth of wafers, is the photoluminescence, which does not discriminate between combinations.

I measured net modal gain as a function of pumping current for the three wafers (figure 3.28), using the multisection method, as described in chapter 2.

The net modal gain was higher at all pump currents for the second growth, lowest for C-doped cap and intermediate, but following a different dependence on current density for the first growth. This could be the result of a composition change: the EPVS value of bandgap energy for the barrier material was higher for this wafer, if compensatory changes in composition were made during growth to maintain the same transition energy. (The measured photoluminescence (PL) peak was 647 nm for this wafer, compared to measured and specified PL of 648 nm for the other two.) The difference in the gain as a function of pump current could be due to a greater efficiency in the second growth wafer. Sources of current or carrier loss, lowering spontaneous emission, include current spreading away from the gain producing region under the

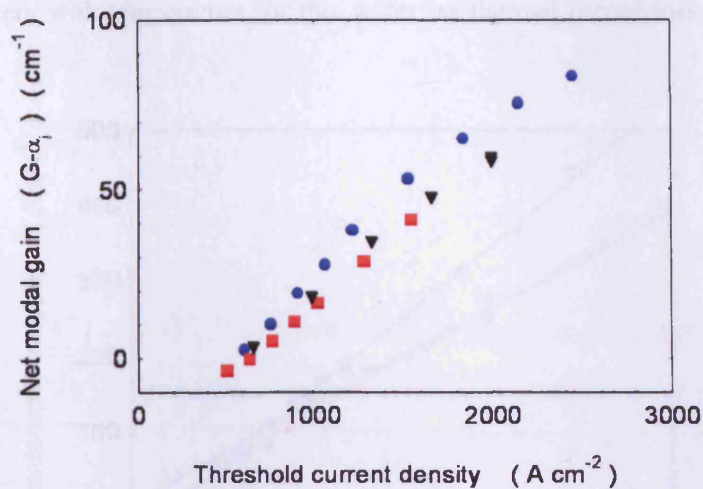


FIGURE 3.28: Net modal gain as a function of pumping current for the three wafers. The net modal gain is higher at all pump currents for the second growth (blue circles), lowest for C-doped cap (red squares) and intermediate, but following a different dependence on current density for the first growth (black triangles)

stripe, non-radiative recombination of carriers, population of indirect valleys and carrier leakage from the quantum wells, an important factor in red emitters. Measurements of modal gain as a function of the current converted into spontaneously emitted photons (J_{spont}) (figure 3.29) showed similar behaviour for all three wafers, supporting this hypothesis.

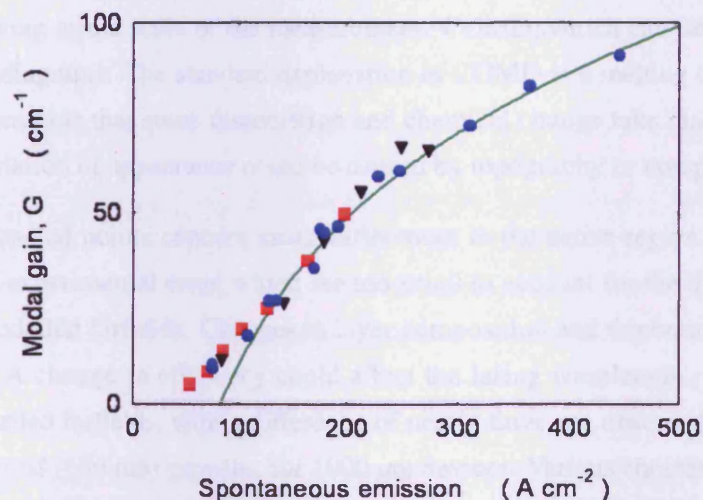


FIGURE 3.29: Modal gain as a function of pumping current for the three wafers (first growth: black triangles, second growth: blue circles and C-doped cap: red squares). The modal gain as a function of current converted into spontaneous emission was very similar for all three wafers, suggesting other results might be explained by differences in efficiency

In addition, measurements of J_{spont} as a function of pump current (figure 3.30), showed a greater efficiency for the second growth wafer, providing further support. This wafer also showed longer lasing wavelength at all lengths. Figure 3.28 shows the net modal gain increases more slowly as a function of pumping current than for the other two wafers, accounting for the faster increase

of threshold current with temperature for this wafer, as thermal carrier loss will be less well compensated for.

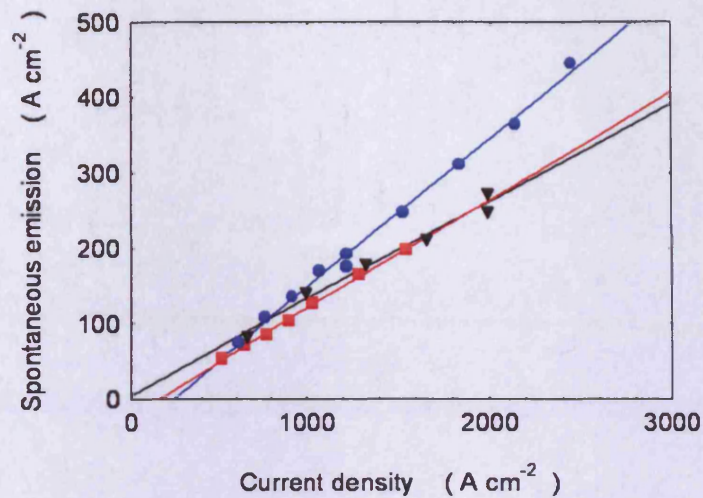


FIGURE 3.30: Spontaneous emission as a function of pump current density, showing a higher efficiency for the second growth wafer (blue circles) than the C-doped (red squares) or the first growth (black triangles), which shows the efficiency dropping off at higher pumping levels

A variation in quantum well thickness was measured by Dr U. Zeimer, on pulsed devices for COMD measurements from the first growth wafer (figure 3.31), showing wider values of quantum well and barrier width than specified, although the uncertainties in this determination might be quite high, owing to the scale of the measurement. COMD, which can be seen on the right hand side of the diagram). The standard explanation of COMD is a melting of a portion of the facet. It is also possible that some dissociation and chemical change take place. With the BSE technique the variation of appearance could be caused by topography or composition change.

The recently discussed points concern small differences in the active region of the wafers, on the borderline of experimental error, which are too small to account for the difference between measured and modelled farfields. Changes in layer composition and thickness were also found to be too small. A change in efficiency could affect the lasing wavelength, which does cause a change in modelled farfields, with a difference of nearly three nm observed between the first (656 nm) and second (659 nm) growths, for 1000 μm devices. Various choices and assumptions are made in the model: for example model solid theory and the MSEO to calculate bandgaps and refractive indices. The accuracy of these could have an effect on the results of modelling.

3.7 Susceptibility to catastrophic optical mirror damage

I modelled the sensitivity of the design to catastrophic optical mirror damage by calculating the area of the facet which would be exposed to laser radiation at a density above the measured

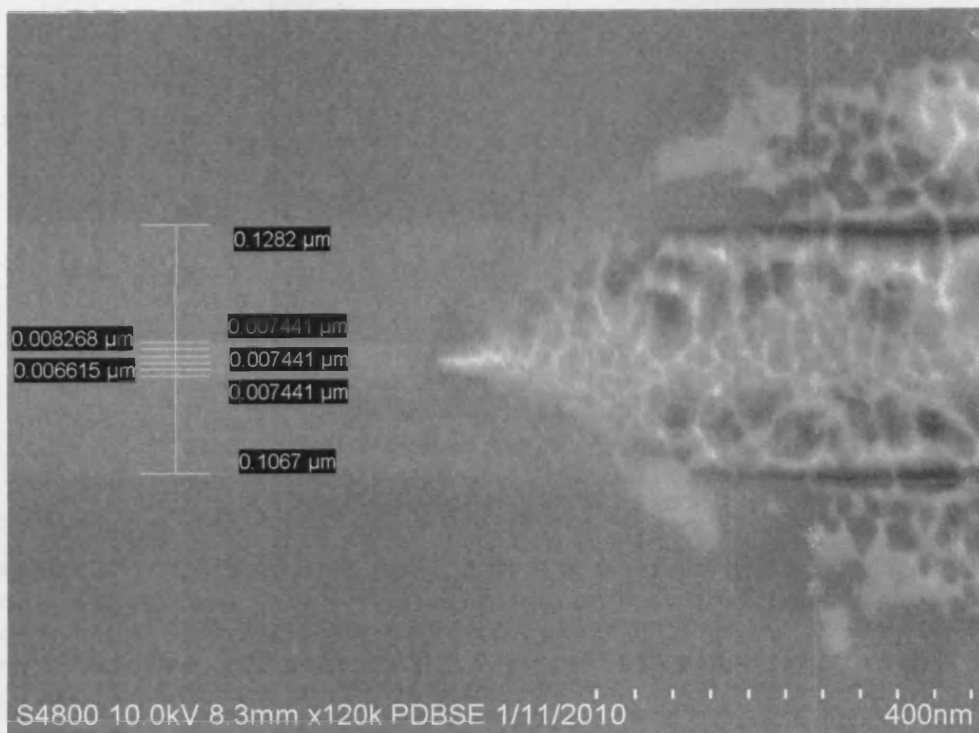


FIGURE 3.31: A SEM image with layer distances measured using a facility on the electron microscope. (The SEM image and measurements were produced by Dr U. Zeimer of Ferdinand-Braun-Institut using an undamaged region of a device I had subjected to a 100 ns 12 A current pulse to study COMD, which can be seen on the right hand side of the diagram).

COMD limit as a function of output power, and compared the measured area of facet damage to the calculated one. Further results of the measurements of COMD power density are presented in Chapter 4, and the results for facet area damaged at COMD are fully explored in Chapter 5.

To obtain an estimate of the power distribution across the total area of the beam I integrated with respect to distance across the transverse nearfield, and, assuming the profile was constant across the stripe width ($50 \mu\text{m}$), multiplied by 50. I then scaled this up for each current in turn so that the power for a given current was numerically equal to the measured power. I used linearly extrapolated powers, since power levels could not be measured at the high currents used (up to 40 A) for the short pulse experiment (discussed in chapters 4 and 5) as the laser was irreversibly damaged in a very short time. For lower powers (as in the COMD comparisons in chapter 4) the thermal effects, although not large, were difficult to fit, so as a first approximation I assumed the P-I characteristic, measured for repeated pulses in an integrating sphere, remained linear at all currents. The assumption of $50 \mu\text{m}$ width takes into account neither the current spreading, which could give a width of $60 \mu\text{m}$ or more, nor the narrowing of the beam as current and power increase. The results for the calculated power density profiles at the facet, as a function of pump current, for a range of currents from 3 A to 40 A in steps corresponding to the values used in single pulse measurements are plotted in figure 3.32. The horizontal line shows a power density ($0.1 \text{ W}/\mu\text{m}^2$ or $10 \text{ MW}/\text{cm}^2$) of the order of magnitude of the measured P_{COMD} as presented

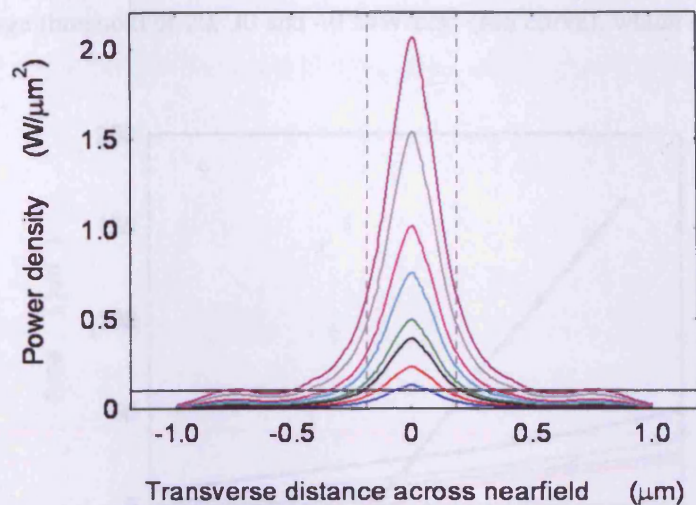


FIGURE 3.32: Calculated power density at the facet as a function of pump current, for a range of currents from 3 A to 40 A in steps corresponding to the values used in single pulse measurements. The horizontal line shows a power density ($0.1 \text{ W}/\mu\text{m}^2$ or $10 \text{ MW}/\text{cm}^2$) of the order of magnitude of the measured P_{COMD} as presented in Chapter 4. The dashed grey lines give the beam width as measured by the spot size, d/Γ

in Chapter 4. The dashed grey lines give the beam width as measured by the spot size, d/Γ (equation 3.1, [63]). The spot size contains the same proportion of total beam power at all power levels and was used to determine the average power density at the facet at COMD. A better measure of beam area might be the area exposed to power densities at levels above a given threshold, taken here as $10 \text{ MW}/\text{cm}^2$. The area of the beam above this power density is simply the width of the distribution multiplied by $50 \mu\text{m}$ and is plotted as a function of current in figure 3.33, together with the measured area of facet damage.

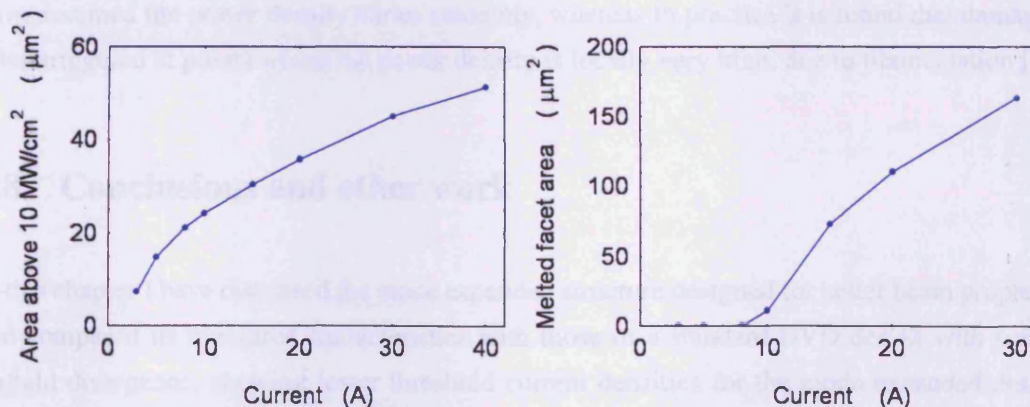


FIGURE 3.33: Modelled (left) and measured (right) areas of facet damage as a function of current. The two curves follow the same mathematical form, although the measured areas have an onset at higher currents and increase more rapidly as a function of current

As can be seen the two curves follow the same mathematical form, although the measured areas have an onset of damage at higher currents than the modelled onset, and the damaged area then increases more rapidly as a function of current. (Figure 3.34). Also shown are modelled lines

assuming a damage threshold of 20, 30 and 40 MW/cm² (red curve), which corresponds to the correct onset.

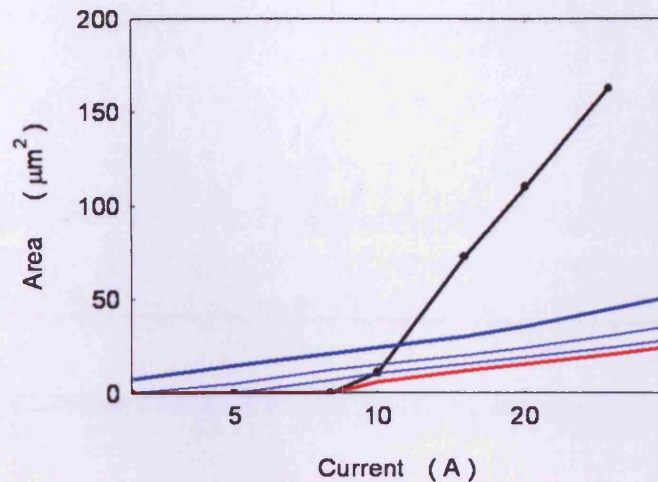


FIGURE 3.34: Modelled and measured (black line with points) areas of facet damage as a function of $\log(\text{current})$. All the lines follow approximately a logarithmic form. The measured areas have an onset of damage at higher currents and the damage area increases more rapidly as a function of current

One way of explaining the disagreement between the calculations and the measurements is if a higher power density was required to trigger damage, and after damage has started, heat generated by the beam in a small area is conducted across the facet to adjacent areas which then undergo thermal runaway and suffer damage, in an similar mechanism to the propagation of molten regions through the interior of the device. Measured power densities are averaged across the spot size area, with a peak power about three times that at the edges. In these calculations I have assumed the power density varies smoothly, whereas in practice it is found that damage is often triggered at points where the power density is locally very high, due to filamentation [50].

3.8 Conclusions and other work

In this chapter I have discussed the mode expanded structure designed for better beam properties and compared its measured characteristics with those of a standard DVD design with similar farfield divergence, showing lower threshold current densities for the mode expanded design. Modelling and measurements of repeated growths have shown the farfield is stable to the degree of variation in growth parameters encountered in a manufacturing environment. While stable, the measured farfield for each of the three wafers was smaller than the design value and an explanation for this was proposed and discussed. Finally I considered whether the design would be particularly susceptible to catastrophic optical mirror damage. I used devices of this design in COMD studies which I describe in later chapters. Operation at powers far in excess of

those necessary for the intended application was necessary before COMD occurred. I compared measured values of area of facet damage with those predicted by modelling of the design.

Chapter 4

Catastrophic degradation: power density limits and mechanisms in QD and QW based devices

4.1 Introduction

Catastrophic optical mirror damage remains the limiting factor to achieving high powers and as such continues to be the subject of research efforts into its causes and their mitigation. QD lasers have been predicted to be more resistant to COMD than those of QW based devices because of their lower surface recombination velocity [64], a reduced tendency to filamentation [65] [66] and the fact that there is less absorbing material at the facet, since there are only cross sections of islands rather than a complete layer of absorbing material as in quantum well based devices. Previous work has shown that COMD is caused by an initial temperature rise of the facet followed by thermal runaway, facet damage and propagation of a molten region which recrystallizes into highly defective, non-radiative material which eventually stops any lasing action. Several mechanisms have been suggested for facet heating, including optical reabsorption [17] and surface currents on the facet [25] [67]. The contribution of any particular process will depend on how far away from threshold the laser is being operated and the condition of the facet, as surface defect sites or oxidation, for example, will cause non-radiative recombination of injected or photo-generated carriers. Measures to raise the COMD power density threshold (P_{COMD}) involve preventing the facet heating and include passivation and coating of the facets, current blocking regions and use of non-absorbing mirrors. These processes add to the expense of manufacturing finished devices. Using a laser that is intrinsically less susceptible to COMD could prevent the need for their use or make these treatments more effective.

Factors thought to affect the likelihood of a laser undergoing COMD, including the QD or QW nature of the active region and pulse length [41] have been investigated for AlGaAs based lasers emitting in the infra-red [25], with structural analysis of the defects in QD based lasers [68], but not in red/NIR emitting AlGaInP based lasers. There is much evidence of propagation of molten regions in QW devices [14] [69] [32] at all wavelengths.

COMD takes place after thermal runaway at the facet so measurements of facet temperature rise can confirm a predisposition to COMD. Physical reasons for a different rate of facet temperature rise have been thought to include the QW or QD based nature of the active region and surface currents leading to non-radiative recombination and heating on the facet, which could be prevented by measures such as specially designed contacts. Facet temperature rises have been measured for such devices in the AlGaAs system, but not in AlGaInP, although a determination of the power density at COMD has been made in this material [32]. These investigations are all based on the assumption that the damage occurs at the facet and is catastrophic optical *mirror* damage (COMD).

In this chapter I describe my investigations to determine the factors that affect the power density at the facet at catastrophic damage, extending work done in other material systems to AlGaInP. Measurements of the power density are undertaken for a range of AlGaInP based lasers with QW and QD based active regions, at different pulse lengths and with the use of current blocking regions, and the most influential factors identified. I extend the facet temperature measurements to a comparison in this material system. However, optical and electron microscopy of the facets, intended to confirm the presence of COMD, revealed an unexpected difference in the nature of the damage observed between QW and QD, leading to further investigations of the exact nature of the physical process or processes. My power density results showed a higher damage limit for QD, but only at short pulse lengths. Previous studies of facet temperature rise in AlGaAs devices [25] observed the expected lower temperature rise in QD devices but, surprisingly, no significant improvement in COMD level. I will describe a proposal, based on the results I have measured, that could explain these unexpected results, in terms of a fundamental difference in the nature of the damage in QW and QD.

In this chapter I will now describe the results of measurement of power density at the facet, identifying the factors with the greatest influence in AlGaInP lasers. I will then describe the results of measurements of facet temperature. In view of my findings I increased the emphasis on microscopy work, and describe the results of my more detailed optical microscopy and SEM with a greater range of techniques, including cathodoluminescence of the active region, carried out in Berlin. Photocurrent and LBIC studies were then used to discover the spectral and physical location of the damage. Finally I discuss the results and propose an explanation of the difference in catastrophic damage between quantum well and quantum dot based devices.

4.2 The power density at the facet at catastrophic damage

I carried out measurements to establish the optical power density limit at COD for various QD and QW structures and devices, operated pulsed. This involved measuring three things: the average power emitted at failure, accurate values of pulse length and frequency to determine the peak power, and the area of intersection of the beam and the facet.

4.2.1 Structures and devices used

All the structures were fabricated in the InP/GaInP/AlGaInP material system and emitted in the red/NIR region, and have been described in Chapter 3, with only brief details repeated here. The two main QW structures used were commercial DVD laser designs, produced using a well developed process, chosen for their very different spot sizes. The small spot size structure ($0.373 \mu\text{m}$) was designed in this group, the large spot size ($0.541 \mu\text{m}$) is a standard commercially available structure. The structures have identical three QW active regions and waveguide material compositions (but not layer thicknesses). These structures are intended for medium power applications such as optical data storage and were being tested well beyond their intended operating limits with no precautions such as heat sinking or facet treatment that would normally be used with high power devices. The quantum dot structures are experimental structures, still in the process of development and consist of 5 layers of quantum dots with small variations in barrier width which change the spot size slightly.

The devices used to determine the power limit were oxide isolated stripe ($50 \mu\text{m}$) lasers. Before mounting the devices were subject to a thorough visual inspection using an optical microscope. Any devices with defects such as flaws in the metallisation or cleave steps on the facet were rejected. I mounted these selected devices p-side up on copper blocks on transistor headers. Electrical characterisation was then carried out as described in chapter 2. I found no correlation between power limit at failure and the results of the electrical characterisation and therefore used all mounted devices, selecting devices for inclusion in the study on the basis of the measured COMD P-I characteristics. Previous studies [10] have shown the rise in facet temperature is significantly lower in devices with the metallisation withdrawn from the edge of the facet, but the pulsed P_{COMD} increased only slightly. Comparison devices were specially fabricated (by Dr. G. Edwards) with normal metallization up to the cleaved edge of the device and metallization removed from a $30 \mu\text{m}$ region adjacent to the facet in both QW and QD structures. Dr G. Edwards also fabricated ridge lasers from one QW and one QD structure for facet temperature measurements. I characterised the devices before carrying out the COMD experiments. (Table 4.1).

	no of devices	device length (μm)	average threshold current (mA)	error error (mA)	lasing wavelength (nm)
QD 2321	12	1000	344	17	711
QD 2323 normal metal	8	2000	377	29	734
QD 2323 cut back metal	8	2000	331	4	734
QD 2522	6	1000	243	10	722
large spot size QW 12-60	12	750	523	6	657
small spot size QW 12-50	16	750	393	7	656
QW 12-50 normal metal	8	2000	816	17	661
QW 12-50 cut back metal	8	2000	803	4	660
pulse length QW 12-48	24	750	382	4	657

TABLE 4.1: Values for initial characterisation of wafers taken to COMD. The error is the standard error in the mean over the batch of devices

4.2.2 Details of measurements

4.2.2.1 Average power over cycle

I placed the devices in an integrating sphere and applied pulsed current with pulse lengths of between 400 ns and 1000 ns at a repetition rate of 1 kHz, increasing the current in steps until the device failed. Pulsed current was used in order to ensure I was testing the intrinsic laser properties and not the effects of heating. The integrating sphere (which had manufacturer's calibration for power) has a built in filter with a sensitivity that depends on the lasing wavelength of the device being measured. The wavelength was measured with an optical spectrum analyser (OSA) which had been compared with the spectrometer I used for gain measurements, the EPVS system and spectral line sources, for accuracy. I measured the average external power over the pulsed current cycle and the current, monitored on an oscilloscope (also with the manufacturer's calibration.) The experiment was stopped when the optical power dropped abruptly to a small fraction of its previous value. (Figure 4.1). As an additional check I examined the appearance of the facets with optical microscopy before current was applied and optical and scanning electron microscopy (SEM) to look for damage typical of COMD after the drop in power level. This gave additional confirmation that catastrophic damage and not merely thermal rollover had taken place.

I then selected a few well-performing devices to obtain the peak power for the structure. Out of each batch of devices tested power levels were widely distributed up to the highest levels seen. No pre-screening, apart from the requirement the device must lase, was used. Devices that would have been rejected, using a burn-in process, for example, did not follow the general P-I characteristic and could be identified. (Lowest three traces in figure 4.1). Flaws in the

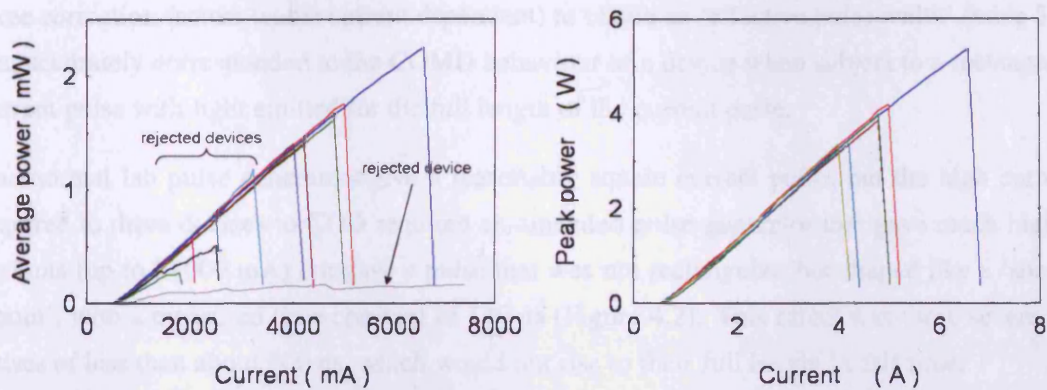


FIGURE 4.1: A typical set of P-I characteristics for a batch of devices showing the abrupt drop that signifies COD. Left: average power over the duty cycle for all devices in the batch. Devices that failed early or did not follow the same p-i characteristic as the others were rejected. The remaining small sample of devices was used to calculate the average peak power density at COMD. In this batch there was one device that performed exceptionally well. If this device alone had been selected the final COMD value for this particular wafer could have been overestimated. Right: The duty cycle was used to calculate peak power vs current for devices selected.

facets, mounting or processing can act as triggers for COMD and many devices failed at a low power level (next three traces). The next traces were used in determination of the power density. If only the highest trace, which should represent the limit the material could intrinsically achieve, was used, a comparison between wafers might compare an excellent device from one batch with a merely good device from another. For this reason I used a small set of the best performing devices and averaged the calculated power densities for the individual devices, using the variation to determine the error in the power density (standard error in the mean). In the literature the beam power is either a calculated value inside the output facet, which would have typically a 5% anti-reflection coating, with a 95% coating on the rear facet, or quoted as an external power density, as I have here.

4.2.2.2 Accurate measurement of duty cycle to determine peak power

I used the mean average power of the selected devices for each wafer (table 5.2) over the cycle to obtain the peak power during the pulse, by dividing the mean average power by the accurately determined duty cycle. This required accurate knowledge of frequency (measured using the oscilloscope) and pulse length. Three important factors affect determination of pulse length: the pulse generators give a pulse that widens slightly as current increases, the device does not achieve lasing levels at the very beginning of the current pulse and the pulse shape on the high current generator used in these measurements is not rectangular. To correct for these I used a photodiode to compare the light pulses obtained with different current pulses, varying current, pulse width, type of pulse generator and QW or QD device, calculating a correction factor for each. I multiplied the nominal pulse width (FWHM as measured on the oscilloscope) by these

three correction factors (some current dependent) to obtain an 'effective pulse width' (table 5.2) that accurately corresponded to the COMD behaviour of a device when subject to a rectangular current pulse with light emitted for the full length of the current pulse.

The normal lab pulse generators give a reasonably square current pulse, but the high current required to drive devices to COD required an amended pulse generator that gave much higher currents (up to 24000 mA) but gave a pulse that was not rectangular, but shaped like a 'shark-tooth', with a measured time constant of 140 ns (Figure 4.2). This effect was more severe for pulses of less than about 500 ns, which would not rise to their full height in this time.

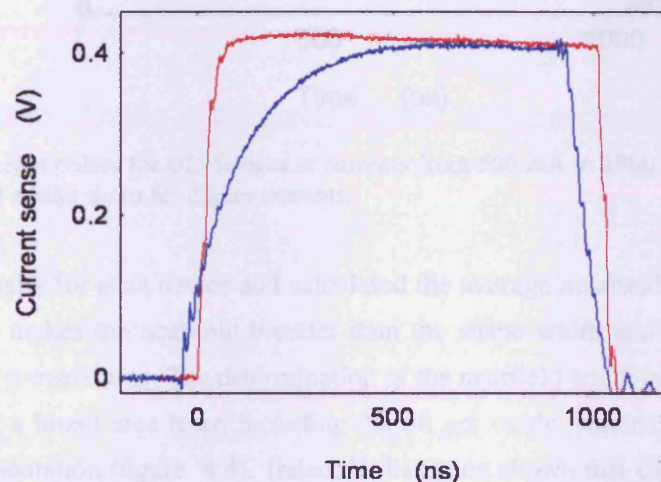


FIGURE 4.2: Current pulse shapes: 1 μ s flat topped pulse (red), sharktooth/capacitor shaped pulse (blue)

It has been observed that for QD devices from the wafers used the onset of lasing light occurs some time after the start of the current pulse (figure 4.3). This delayed onset decreases as current increases, levelling off at high currents. The effect is there, but smaller for QW devices.

The most important correction factor was the increase of pulse width with current, with increases of 5% to 20% depending on the current reached. The correction for pulse shape gave a decrease in effective pulse width of up to 5%, and the percentage of the current pulse time for which the light is on reached a limiting value of 98% in QW and 95% in QD devices at the highest current used. The corrections were individually calculated for each batch of devices. As well as being used in the duty cycle, if the wrong pulse width was used to compare devices the resulting error could give an apparent increase or decrease in the power density at COMD. In fact the correction was sufficiently small that it did not change any conclusions drawn.

4.2.2.3 Area of beam at facet

I multiplied the spot size, calculated using the method described in chapter 3, by the measured FWHM nearfield width to obtain the beam area at the facet and the power density. I measured the

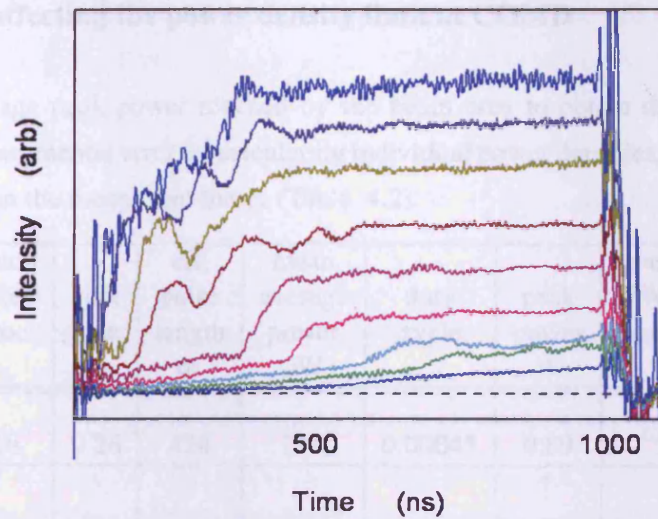


FIGURE 4.3: Light pulses for QD devices at currents from 500 mA to 1800 mA, showing the onset of light at earlier times for higher currents.

nearfields individually for each device and calculated the average nearfield for a set of devices. Current spreading makes the nearfield broader than the stripe width and can be different for different wafers or process runs. The determination of the nearfield width is not straightforward, as the nearfield of a broad area laser, including the $50\ \mu\text{m}$ oxide isolated stripe lasers I used, shows strong filamentation (figure 4.4). Indeed, it has been shown that COMD can take place at the nearfield peaks in a filamenting device [50], where the power density is greatest.

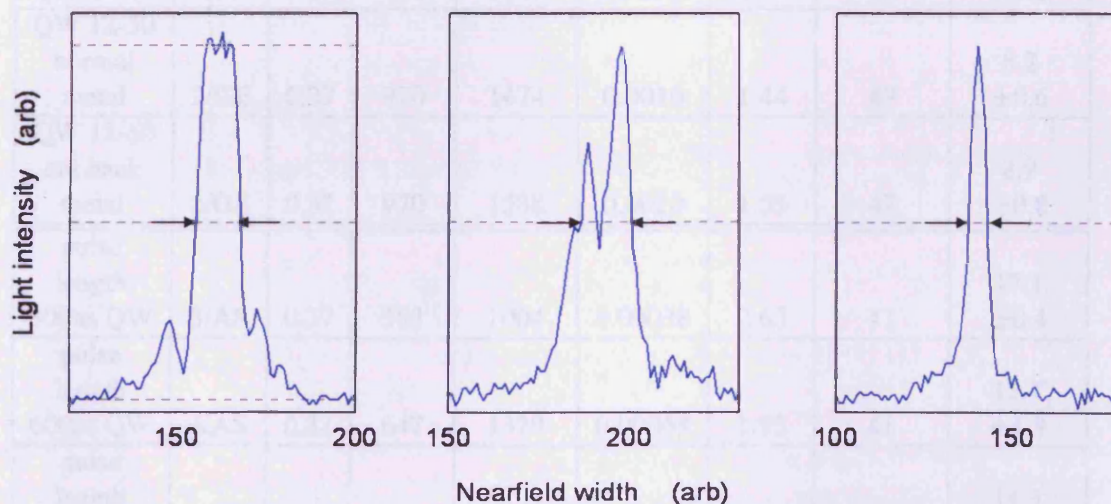


FIGURE 4.4: Nearfield profiles for three quantum dot devices from the same batch showing the uncertainty in nearfield width introduced by filamentation and showing how the FWHM nearfield width is measured

4.2.3 Factors affecting the power density limit at COMD

I divided the average peak power reached by the beam area to obtain the power density. I determined the experimental error by calculating individual power densities, and then calculated the standard error in the mean from these. (Table 4.2)

Wafer type, identifier	batch size / proc.	spot size μm	eff. pulse length ns	mean average power μW	duty cycle	peak power W	average FWHM nearfield μm	COMD power density MW/cm^2
QD 2321	3/s	0.26	424	397	0.00045	0.89	19	18.4 ± 0.9
QD 2323 normal metal	4/s	0.28	1029	1835	0.0011	1.69	66	9.2 ± 0.5
QD 2323 cut back metal	2/GE	0.28	993	1610	0.0010	1.54	65	8.5 ± 0.8
QD 2522	2/SS	0.28	434	2044	0.0022	0.95	20	16.5 ± 4.1
large spot size QW 12-60	4/s	0.54	500	1833	0.00053	3.48	54	11.9 ± 1.2
small spot size QW 12-50	5/s	0.37	461	1346	0.00049	2.77	52	14.3 ± 1.9
QW 12-50 normal metal	2/GE	0.37	970	1474	0.0010	1.44	47	8.2 ± 0.6
QW 12-50 cut back metal	2/GE	0.37	970	1588	0.0010	1.55	47	8.9 ± 0.8
pulse length 300ns QW	3/AS	0.37	363	1004	0.00038	2.63	41	17.1 ± 0.4
pulse length 600ns QW	4/AS	0.37	647	1329	0.00068	1.95	41	12.7 ± 1.3
pulse length 900ns QW	3/AS	0.37	921	1687	0.00097	1.74	41	11.3 ± 1.8

TABLE 4.2: Values of raw data used to calculate the beam area at the facet, the peak power and hence power density at COMD. The number of devices selected from the batch to include in the final value is indicated. Key to processing: standard processing: s (Karen Barnett) or Sam Shutts (SS), devices for the metal removed from the edge of the facet (cut back) and comparators (normal), and ridge lasers were produced by Dr Gareth Edwards (GE). Dr Angela Sobiesierski (AS) produced the devices used in the pulse length experiment.

The structures used enabled the following comparisons to be made. The comparison of two different spot size QW structures ($0.37\ \mu\text{m}$ and $0.54\ \mu\text{m}$) gave the same power density values (within error) of $14.3 (\pm 1.9)\ \text{MW}/\text{cm}^2$ and $11.9 (\pm 1.2)\ \text{MW}/\text{cm}^2$ respectively. The samples with normal metallization and metallization removed from a $30\ \mu\text{m}$ region adjacent to the facet showed no difference in the COMD limit in either QW or QD structures. (Table 5.2). It is known that pulse length affects the COMD limit [41]. If the length of the pulse is short any heat generated in the facet has time to dissipate before the next pulse. The heat from longer pulses or cw pumping causes a larger facet temperature rise due to the finite thermal conductivity of the epitaxial layers in the structure in addition to bulk Joule heating. As the heat builds up in the device a critical facet temperature [18] is reached beyond which COMD proceeds very rapidly. A simple 1-d analytical model [20], assuming a monolithic block of material, predicts $1/t^{1/2}$ dependence of the temperature rise at the facet, where t is the pulse length. It was thus also necessary to accurately know the pulse length when comparing different structures.

The facet damage occurs at a critical power density which varies with the material system used: in the GaInP/AlGaInP system values as low as $3.5\ \text{MW}/\text{cm}^2$ [32] cw are seen. The factors that had the greatest effect on the COMD power density limit were the QD or QW nature of the active region and the pulse length. At short pulse lengths I found the external power density limit at COMD was higher in QD, as shown in figure 4.5.

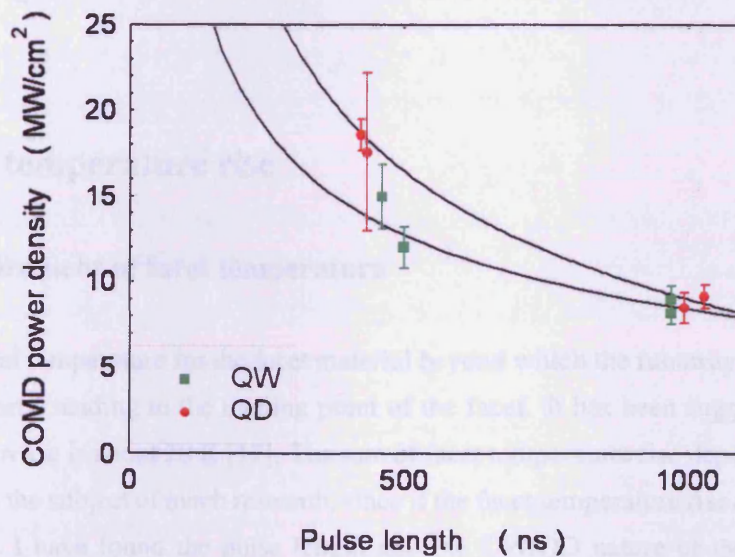


FIGURE 4.5: COMD power density limit for the QW and QD structures described above. The error bars are the standard error in the mean over a small number of well-performing devices, as indicated in table 4.2. The solid lines are a guide to the eye, based on $1/(\text{pulse length})^{0.5}$. The factors that had the greatest effect on the COMD power density limit were the QD or QW nature of the active region and the pulse length

Comparison of the power density limit at COMD for three sets of devices from the same wafer showed the limit decreased with pulse length approximately inversely proportional to the square root of the pulse length. (Figure 4.6)

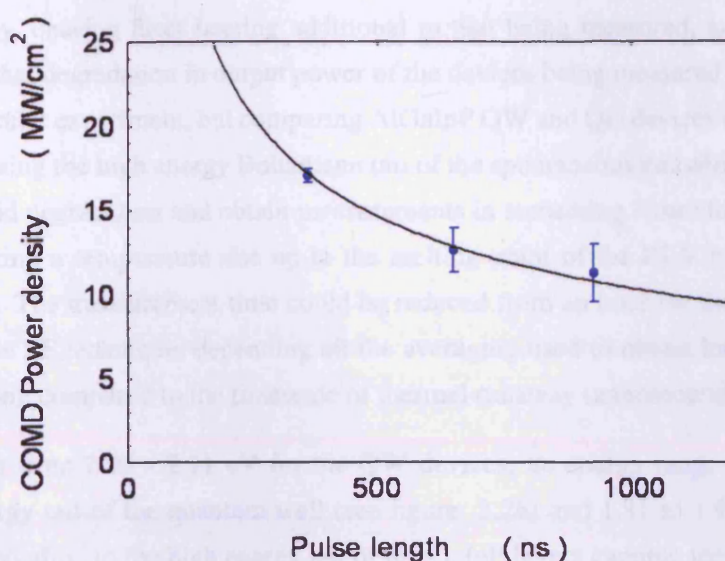


FIGURE 4.6: The COMD power density limit as a function of pulse length for a QW structure (small spot size QW). The solid line is proportional to the reciprocal of the pulse length raised to the power of 0.5. The error bars are given by the standard error in the mean

In summary, of all the factors compared, the pulse length and QD - QW nature of the active region most strongly affected the power density at COMD, with a higher limit in QD, but only at short pulse lengths. The differences due to other factors were of the order of the experimental error.

4.3 Facet temperature rise

4.3.1 Measurement of facet temperature

There is a critical temperature for the facet material beyond which the runaway spiral associated with COMD starts, leading to the melting point of the facet. It has been suggested the critical temperature increase is about 20 K [12]. The rate of facet temperature rise depends on a number of factors and is the subject of much research, since if the facet temperature rise can be prevented, so can COMD. I have found the pulse length and the QW/QD nature of the facet to be the factors with the greatest effect on the COMD limit and used these in comparison studies of facet temperature rise.

Previous work [25] has used microRaman measurements to establish a greater temperature rise in QW than QD structures, pumped to 8x threshold, for 1100 nm emitting devices specially grown to have no differences except in the active region, with almost identical P-I characteristics and threshold currents of about 250 mA. The Raman technique involves irradiating the facet with a probe laser and monitoring the shift in absorbed and re-emitted radiation. The probe laser is

of high intensity, causing facet heating additional to that being measured, and is applied for sufficient time that degradation in output power of the devices being measured is a possibility. I carried out a similar experiment, but comparing AlGaInP QW and QD devices emitting red/near infra-red, and using the high energy Boltzmann tail of the spontaneous emission (SE) [28] from the facet to avoid degradation and obtain measurements in something closer to real time, in the hope of measuring a temperature rise up to the melting point of the III-V compounds in the epitaxial layers. The measurement time could be reduced from an hour for the microRaman to minutes with the SE technique, depending on the averaging used to obtain low noise data, but was still very long compared to the timescale of thermal runaway (nanoseconds [12]).

I used emission from 2.05 - 2.11 eV for the QW devices, an energy range that corresponds to the high energy tail of the quantum well (see figure 3.26) and 1.91 to 1.97 eV for the QD devices, corresponding to the high energy tail of the GaInP layers capping the dots. The modal absorption is of the order of 200 cm^{-1} (figure 4.7), resulting in a distance of about $35 \mu\text{m}$ for the intensity of the radiation to halve, and remains constant once away from the exciton peaks, due to the QW nature of the density of states. This will result in a lower temperature rise averaged over material deeper than the surface of the facet. Ideally the increased absorption with temperature would mean the SE was only emitted from regions close to the surface of the facet. The method relies on the assumption the electron temperature and lattice temperature are the same. If the carrier concentration, monitored by quantity of spontaneous emission, pins at threshold the electron temperature should not increase with pumping above this point so even if they are not in equilibrium, above threshold any measured increase in temperature will be due to a change in lattice temperature.

Since the lasing wavelength shifts with the bulk temperature of the device, the facet temperature rise over and above the bulk temperature rise needs to be determined. I made measurements of the total facet temperature rise and of lasing wavelength as a function of temperature to determine the bulk temperature rise and hence the net facet temperature rise.

I used $4 \mu\text{m}$ wide, $2000 \mu\text{m}$ long shallow etched ridge lasers fabricated (by Dr G. Edwards) from the QD and QW wafers used for power density measurements in order to accurately define the facet area where the temperature rise occurred, mounted p-side up as previously described. Accurate location of areas experiencing the highest temperatures would not be possible in a broad area laser due to filamentation, but good beam quality was obtained with these devices (figure 4.8). The threshold currents were 180 mA for the QW devices and 25 mA for the QD devices.

The lining up procedure involved aligning the spectrometer with the laser beam, as for a normal measurement, and then rotating the device in small steps, realigning the device and spectrometer each time. During alignment I maximised the high energy part of the spectrum since the highest energy radiation would come from the hottest part of the facet. This enabled a check

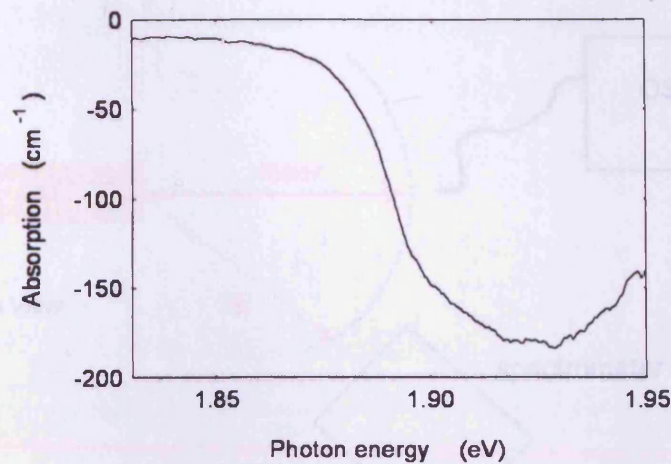


FIGURE 4.7: Modal absorption for the wafer used to fabricate QW ridge lasers, measured using the multisection method

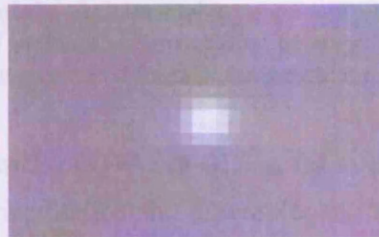


FIGURE 4.8: The nearfield of a QW ridge laser used for facet temperature measurements

that neither laser radiation nor amplified spontaneous emission was collected (figure 4.9), since as the angle of alignment increased, eventually, at angles of 45 degrees or more, the amplitude of the collected radiation no longer decreased with angle, showing the collected light was not guided by the waveguide (the ridge). I collected laser radiation with an optical fibre connected to a spectrum analyser (OSA) and monitored the lasing wavelength during facet temperature measurements to monitor any bulk temperature rise and thus find the temperature rise for the facet alone.

It can be shown (Chapter 2, [28]) that in the Boltzmann approximation the intensity of spontaneous emission, L , is proportional to $E^2 \exp(-E/kT)$. A plot of $\ln(L/E^2)$ vs E yields a straight line with slope $-(1/kT)$. An example of a spontaneous emission spectrum in the facet temperature measurements is given in figure 4.10, together with a plot of $\ln(L/E^2)$ vs photon energy, below. The cutoff is caused by the edges of the image intensifier in the spectrometer. The range used for temperature measurement is indicated by the vertical lines.

In a preliminary experiment I performed the facet temperature measurements on a broad area device pumped to 30x threshold. The log of the intensity obtained is shown in figure 4.11, (left). I used the straight line portion on the high energy, short wavelength side to find the facet temperature (right).

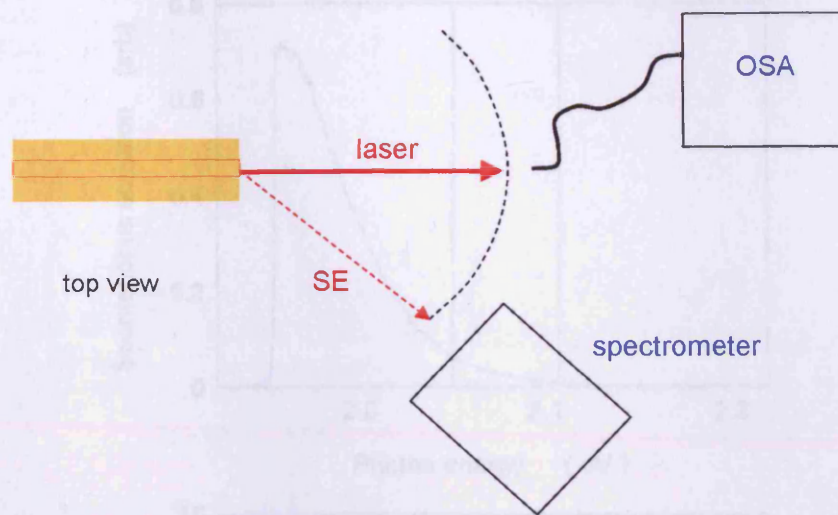


FIGURE 4.9: A schematic of the experimental arrangement used to measure facet temperature. The device was rotated so that no laser radiation or amplified spontaneous emission was collected. Laser radiation was monitored for bulk temperature rise

I then used ridge lasers (two each of QW and QD) at up to twice threshold to obtain sets of measurements at three different pulse lengths. Examples of these are given for QW (left) and QD (right) devices in figure 4.12. The black and blue points are measured using pulse lengths of 340 ns and 1000 ns respectively. A clear change of gradient can be seen at threshold for the QW devices, with a steeper gradient for the 1000 ns measurements, indicating more bulk heating. There was more scatter in the QD measurements due to lower signal levels. The open and closed symbols indicate measurements made as a function of increasing or decreasing current with good agreement between these sets, indicating the alignment of the device did not change during the measurement. There is a clear change of slope for the QW devices at threshold (180 mA, dotted grey line), but no obvious change for the QD devices. Room temperature was 294 K. As discussed in Chapter 2, the measured temperature is the result of contributions from several processes and a change of gradient is expected at threshold. If the contribution from reabsorption of radiation is particularly large the gradient of the measured temperature will increase at threshold, rather than decrease. This was seen for one device. (Figure 4.13)

The effect of change of alignment of the device (Figure 4.14) causes a vertical shift in apparent temperature. The alignment changed continuously during these measurements taken over a series of increasing followed by decreasing and then increasing currents, taken during preliminary alignment. Data was taken once the alignment had stabilised.

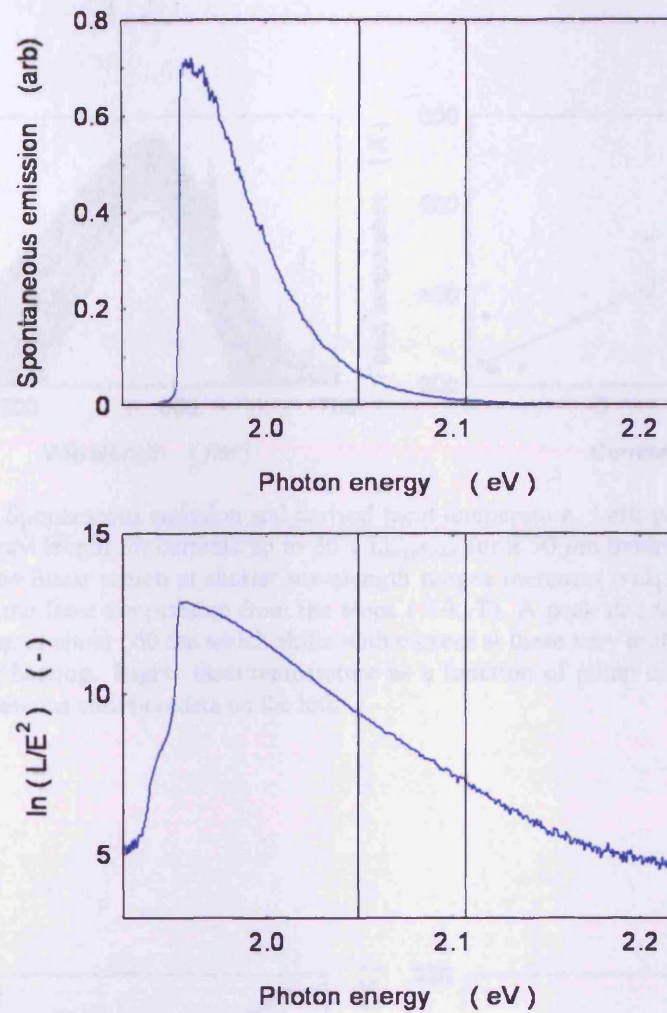


FIGURE 4.10: An example of a spontaneous emission spectrum for a QW ridge laser (top) together with a plot of $\ln(L/E^2)$ below. The cutoff is caused by the edges of the image intensifier in the spectrometer. The range used for temperature measurement is indicated by the vertical lines

4.3.2 Determination of bulk heating

The measured facet temperature is the sum of the facet temperature increase and any bulk temperature increase. I first estimated the likely size of any bulk heating. The main source of bulk heating is from electrical power ($P = IV$) that is not converted into optical power (P_{opt}) and is given by $P_{heat} = IV - P_{opt}$. I measured voltages across samples which showed the large majority of the voltage drop is internal to the device, not across electrical contacts and transistor header, thus I could use the measured optical power and i-v characteristics, both extrapolated linearly, to calculate an approximate value of the heat input and efficiency of the devices. By taking values of specific heat capacities for the III-V compounds in the layers and interpolating from the binaries where necessary, I estimated the bulk temperature rise would be between 0.3 K for a 300ns pulse if all the energy input during a pulse was retained within but distributed throughout

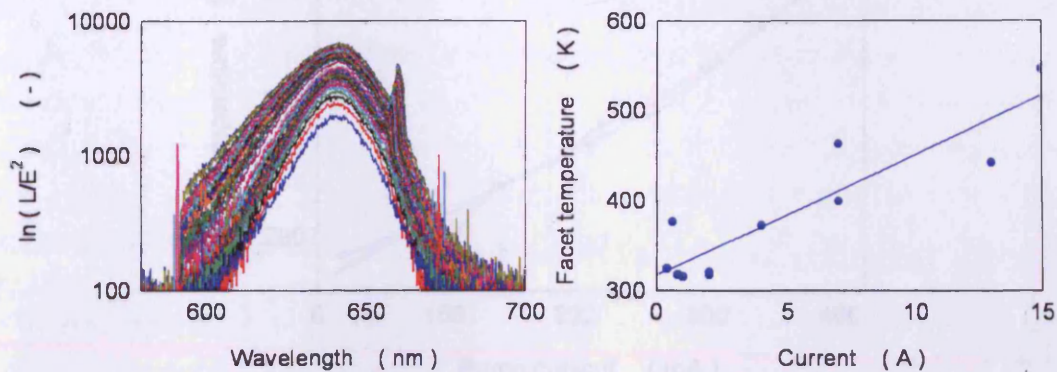


FIGURE 4.11: Spontaneous emission and derived facet temperature. Left: plot of $\ln(L/E^2)$ as a function of wavelength for currents up to $30 \times I_{threshold}$ for a $50 \mu\text{m}$ oxide stripe QW laser. The slope of the linear region at shorter wavelength ranges increases with current, and was used to obtain the facet temperature from the slope ($-1/k_B T$). A peak due to scattered lasing light can be seen at about 660 nm which shifts with current at these very high pumping levels, indicating bulk heating. Right: facet temperature as a function of pump current determined from the spontaneous emission data on the left.

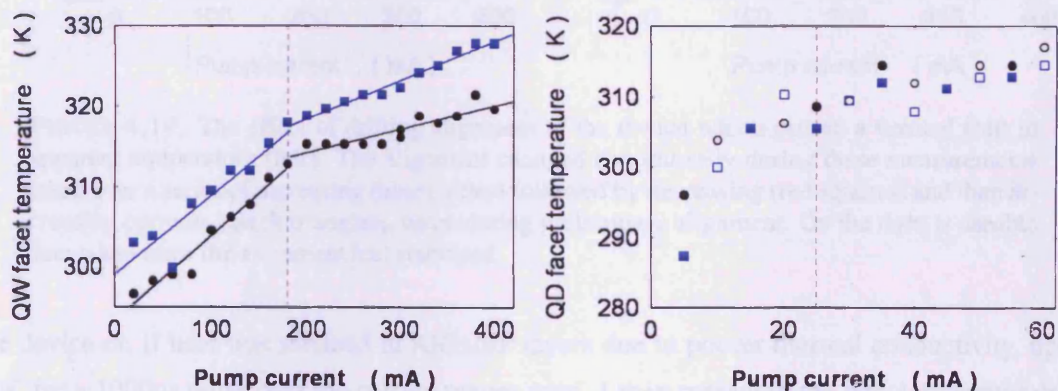


FIGURE 4.12: Examples of facet temperature determined using the high energy tail of the spontaneous emission from the facet of QW (left) and QD (right) ridge lasers. The black and blue points are measured using pulse lengths of 340 ns and 1000 ns respectively. A clear change of gradient is seen at threshold for the QW devices with a steeper gradient for the 1000 ns measurements, indicating more bulk heating. There was more scatter in the QD measurements due to lower signal levels, but no obvious change in slope to indicate heating by reabsorption. The open and closed symbols indicate measurements made as a function of increasing or decreasing current. The fact that the points lie on top of each other apart from scatter shows the alignment of the device did not change during the measurement. Threshold is indicated by the vertical dashed line

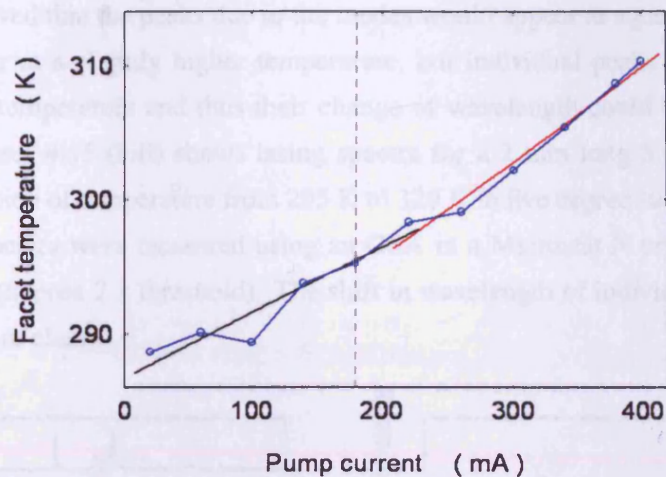


FIGURE 4.13: Measured facet temperature as a function of pump current for a QW device. If the contribution from reabsorption of radiation is particularly large the gradient of the measured temperature will increase at threshold, rather than decrease. This is seen in this device.

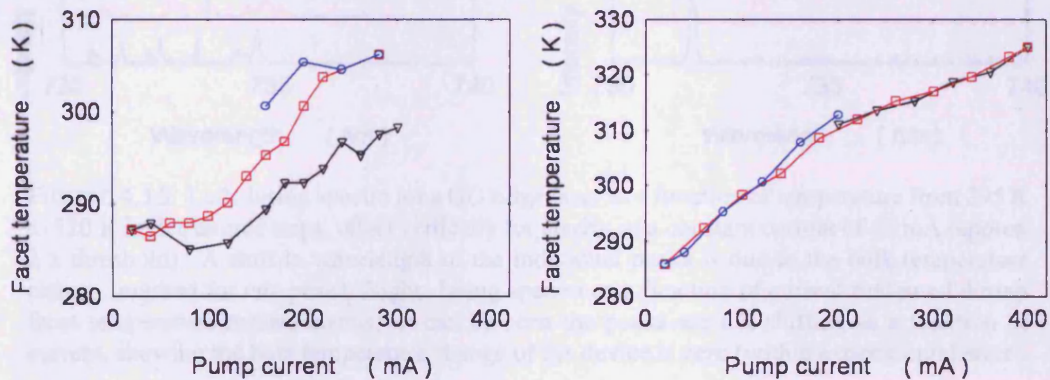


FIGURE 4.14: The effect of drifting alignment of the device which caused a vertical shift in apparent temperature (left). The alignment changed continuously during these measurements taken over a series of increasing (blue circles) followed by decreasing (red squares) and then increasing currents (black triangles), taken during preliminary alignment. On the right is useable data taken once the alignment had stabilised

the device or, if heat was retained in AlGaInP layers due to poorer thermal conductivity, up to 20K for a 1000ns pulse over the current ranges used. I then measured the bulk temperature rise from the change in lasing wavelengths.

Measurements of lasing wavelength for broad area devices shows the rate of change of lasing wavelength with temperature for quantum dot based devices is much smaller than for QW based devices [70]. The lasing spectrum of a ridge device as a function of pumping current is a convolution of the gain spectrum and the mode structure produced by the waveguiding (ridge and layers) that makes a determination of temperature for ridge devices complex, as the detection of lasing in a particular mode will depend on several things. If the device is pumped harder the gain envelope will shift to higher energies. Any bulk temperature rise will result in a shift of lasing wavelength to lower energies. I measured lasing wavelength as a function of temperature in a

cryostat and observed that the peaks due to the modes would appear at a particular temperature and then disappear at a slightly higher temperature, but individual peaks could be identified across a range of temperature and thus their change of wavelength could be used to measure temperature. Figure 4.15 (left) shows lasing spectra for a 2 mm long 5 μm wide ridge QD structure as a function of temperature from 295 K to 320 K in five degree steps, offset vertically for clarity. The spectra were measured using an OSA in a Microstat N cryostat at a constant current of 65 mA (approx 2 x threshold). The shift in wavelength of individual peaks is due to the bulk temperature change.

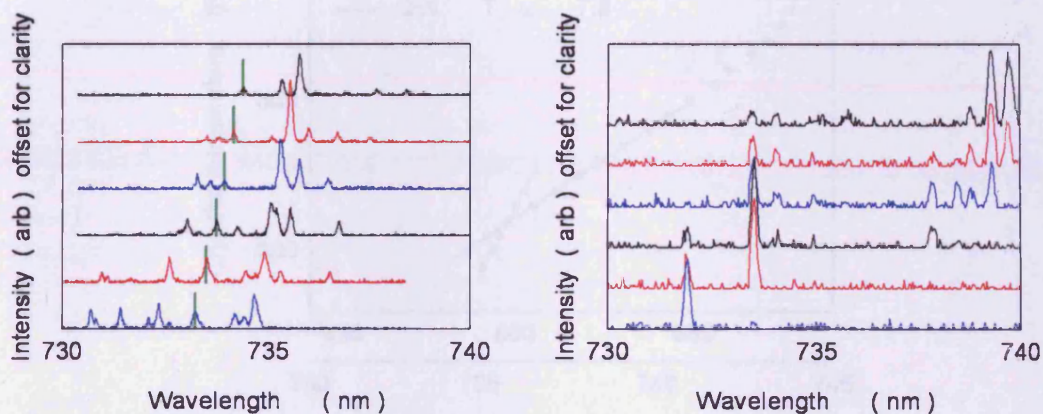


FIGURE 4.15: Left: lasing spectra for a QD ridge laser as a function of temperature from 295 K to 320 K in five degree steps, offset vertically for clarity, at a constant current of 65 mA (approx 2 x threshold). A shift in wavelength of the individual peaks is due to the bulk temperature change (marked for one peak). Right: lasing spectra as a function of current measured during facet temperature measurements. It can be seen the peaks are not shifting as a function of current, showing the bulk temperature change of the device is zero (within experimental error).

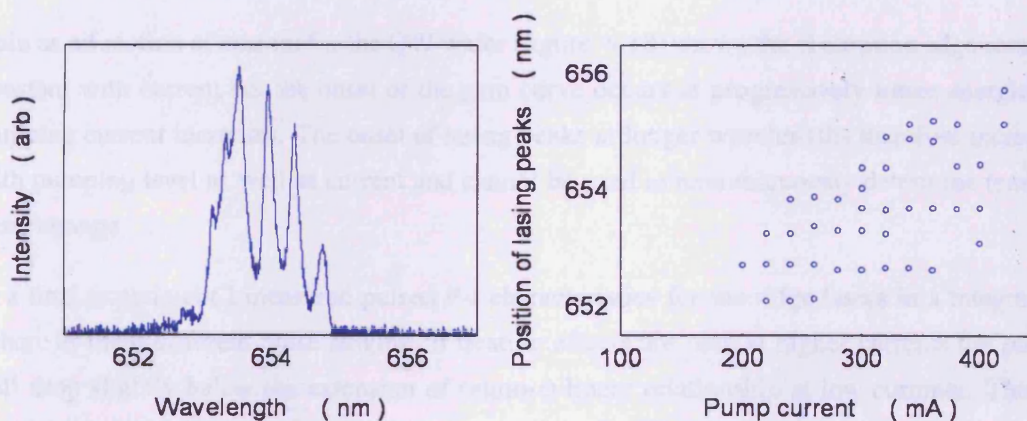


FIGURE 4.16: Left: Example of a typical lasing spectrum for one of the ridge waveguide quantum well lasers used in the facet temperature measurements. Right: the distribution of lasing peaks as a function of pumping current. Each circle represents the position of one peak at a particular current.

Figure 4.17 shows the results of using this technique to measure temperature as a function of lasing wavelength for QW and QD devices, from the shift of a single lasing peak with temperature. A least squares fit over a range of this data was used to provide calibration functions for

temperature shift in terms of wavelength shift for my devices over the small temperature changes expected. In fact, no real shift of lasing peaks could be seen during the measurements as shown in figure 4.15 and figure 4.16 for QD and QW devices, indicating a change in bulk temperature of less than the experimental error. I estimated the error in the determination of the wavelength of the peaks to be ± 0.1 nm, corresponding to an error in temperature of ± 2 K for QD and ± 0.8 K for QW.

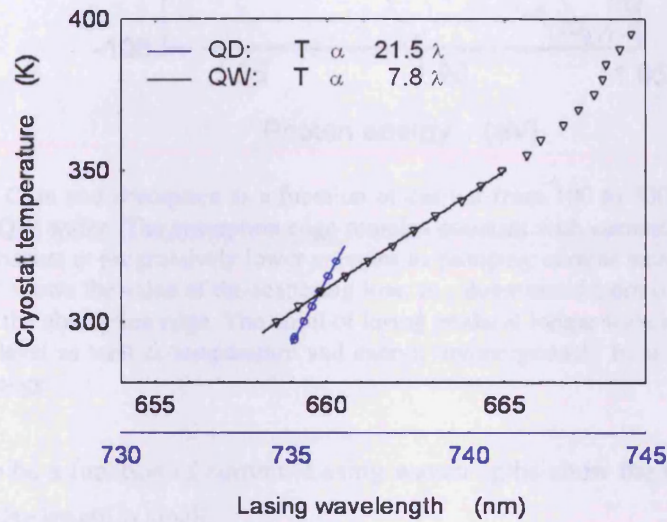


FIGURE 4.17: Temperature as a function of lasing wavelength for QW (blue circles) and QD (black triangles) determined from the shift of a single lasing peak with temperature, measured in a cryostat. This data was used to provide calibration functions (fitted lines, as shown) for temperature shift in terms of wavelength shift for my devices over the small temperature changes expected

Gain as a function of current for the QW wafer (figure 4.18) shows the absorption edge remains constant with current but the onset of the gain curve occurs at progressively lower energies as pumping current increases. The onset of lasing peaks at longer wavelengths therefore increases with pumping level as well as current and cannot be used to unambiguously determine temperature change.

In a final experiment I measured pulsed P-I characteristics for the ridge lasers in a integrating sphere at three different pulse lengths. If heating effects are seen at higher currents the power will drop slightly below the extension of (almost) linear relationship at low currents. The integrating sphere gave an average power over the cycle. Figure 4.19 shows examples of P-I characteristics for QD and QW ridge lasers, scaled up by the ratio of the pulse lengths. If bulk heating of the device occurs, thermal rollover will be seen as a droop in the P-I characteristic at higher currents and pulse lengths, if there is no heating effect the curves should superimpose exactly. As can be seen, at currents above about 350 mA for the QW devices there is a droop that increases with pulse length. It would not be possible to make similar measurements in a cryostat as a function of temperature, at constant pulse length, to calibrate this, as the temperature

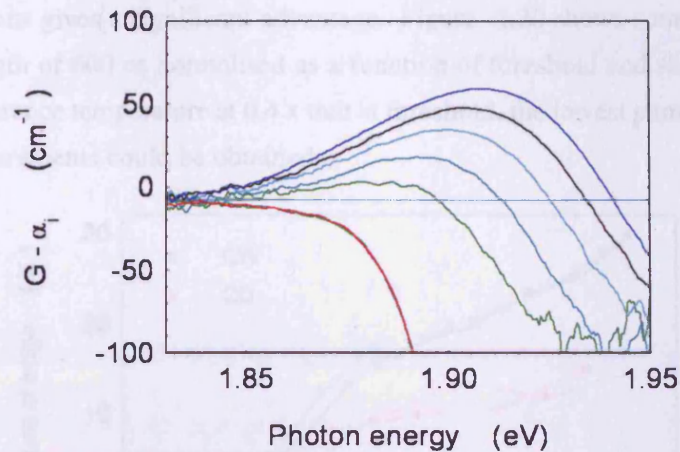


FIGURE 4.18: Gain and absorption as a function of current from 100 to 300 mA in steps of 50 mA for the QW wafer. The absorption edge remains constant with current but the onset of the gain curve occurs at progressively lower energies as pumping current increases. The horizontal blue line shows the value of the scattering loss, α_i , determined from the gain curves at energies below the absorption edge. The onset of lasing peaks at longer wavelengths increases with pumping level as well as temperature and cannot unambiguously be used to determine temperature change

change would also be a function of current. Lasing wavelengths show the temperature change as a function of pulse length is small.

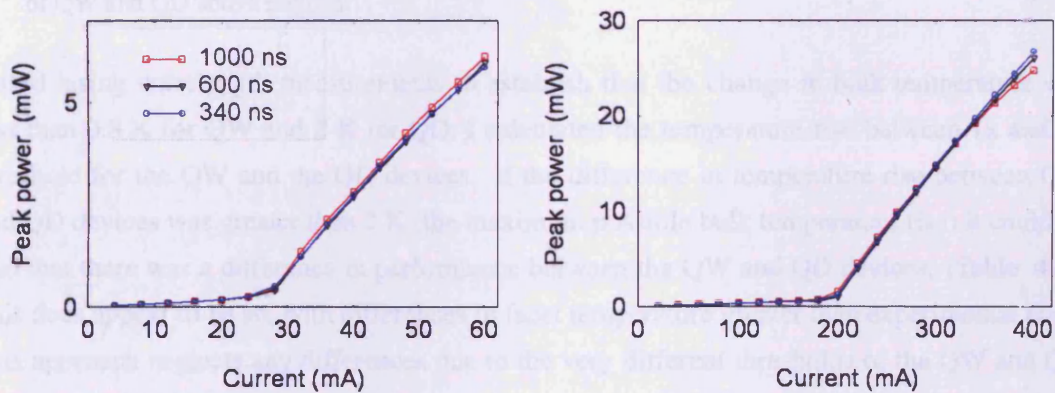


FIGURE 4.19: P-I characteristics for QD (left) and QW (right) ridge lasers for three different pulse lengths, scaled up by the ratio of the pulse lengths. If bulk heating of the device occurs, thermal rollover will be seen as a droop in the P-I characteristic at higher currents and pulse lengths, if there is no heating effect the curves should superimpose exactly. As can be seen, at currents above about 350 mA for the QW devices there is a droop that increases with pulse length.

I investigated the temperature rise at the facet in both QD and QW as a function of laser power at pump currents of up to twice threshold. This is the region of most interest, because in this range it should be possible to differentiate between the effects of non-radiative recombination of injected carriers, which saturates at threshold [71] and reabsorption of laser radiation leading to generation and non-radiative recombination of carriers at the facet, accompanied by heating [17], which starts at threshold and increases with laser power. This should confirm whether the use

of QD active regions gives a significant advantage. Figure 4.20 shows some data for QW and QD at a pulse length of 600 ns normalised as a function of threshold and showing temperature change from a reference temperature at $0.4 \times$ that at threshold, the lowest pumping level at which temperature measurements could be obtained.

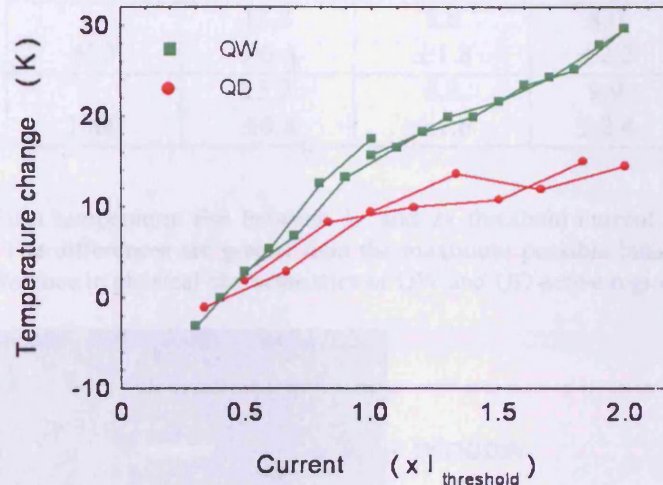


FIGURE 4.20: Facet temperature rise for QW and QD ridge devices at a pulse length of 600 ns (normalised to threshold current and facet temperature at threshold). The difference in temperature rise from $1x$ to $2x$ threshold current between QW and QD devices is greater than the maximum possible bulk temperature rise, indicating a real difference in physical characteristics of QW and QD active regions.

I used lasing wavelength measurements to establish that the change in bulk temperature was less than 0.8 K for QW and 2 K for QD. I calculated the temperature rise between $1x$ and $2x$ threshold for the QW and the QD devices. If the difference in temperature rise between QW and QD devices was greater than 2 K (the maximum possible bulk temperature rise) it could be said that there was a difference in performance between the QW and QD devices. (Table 4.3). This does appear to be so, with differences in facet temperature greater than experimental error. This approach neglects any differences due to the very different thresholds of the QW and QD devices, but this is probably justified as the difference is still greater than any bulk temperature rise, as measured by change of lasing wavelength.

4.3.3 Measurement of temperature from top window emission

Finally in order to confirm the temperature obtained from the tail of the spontaneous emission was a reliable measure of the material temperature, ie the temperature of the lattice as opposed to the temperature of the electron distribution, I obtained the temperature from the spontaneous emission from a top window (figure 4.21) in a laser, as a function of temperature and current (figure 4.22). An increase in temperature should be seen as the bulk temperature of the sample was controlled by the cryostat. An increase as a function of pumping level should not be seen,

pulse length ns	facet temperature rise QW K	facet temperature rise QD K	difference QW - QD K
340	12.3 ± 0.7	3.8 ± 3.8	8.5 ± 4.5
600	13.8 ± 0.4	5.8 ± 1.8	8.0 ± 2.2
1000	15.2 ± 0.8	5.3 ± 1.6	9.9 ± 2.4

TABLE 4.3: Facet temperature rise between 1x and 2x threshold current for QW and QD ridge devices. The differences are greater than the maximum possible bulk temperature rise indicating a difference in physical characteristics of QW and QD active regions

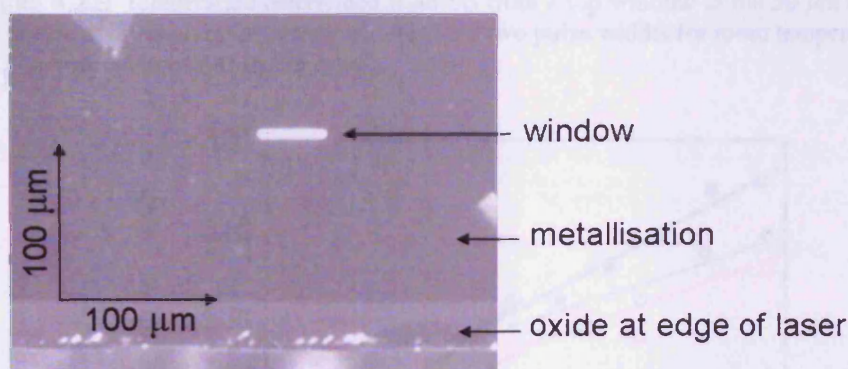


FIGURE 4.21: Part of the top surface of a device with a 50 μm top window in the metallisation over the stripe for measuring spontaneous emission from the cool interior

as I have shown bulk temperature does not increase significantly as a function of pumping level by lasing wavelength measurements, but increases were seen as both a function of cryostat temperature and pumping current, but not as a function of pulse length. I measured the integrated intensity of spontaneous emission as a function of pump current and found it did not entirely pin at threshold, although the rate of increase with current was much less above threshold. This could be due to current leakage increasing with current and producing SE outside the stripe or ridge [6, 72]. It is also possible the method I have used measures the temperature of the electron distribution only, and this is not in equilibrium with the lattice temperature. If this was the case, however, the temperature of the facet would not show the expected effects as discussed earlier, such as the effect of increased optical reabsorption in one quantum well device, and a pronounced change of slope at threshold in quantum well devices, unless this increased the electron temperature by optical pumping.

Comparison of the top window and facet temperature measurements (figure 4.23) shows that even with the scatter in the data, a larger temperature increase is seen at the facet. Thus there is some measured temperature rise in addition to any electron temperature rise. I saw the effects

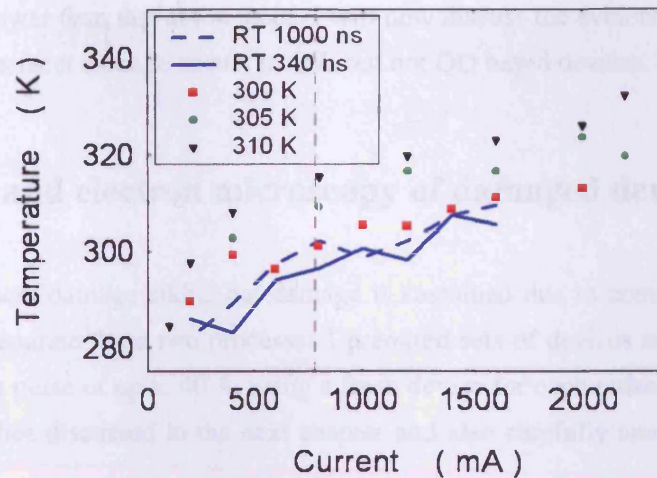


FIGURE 4.22: Temperature determined from SE from a top window in the $50\ \mu\text{m}$ stripe of a QW device at different cryostat temperatures (and two pulse widths for room temperature (296 K)). The vertical line indicates threshold.

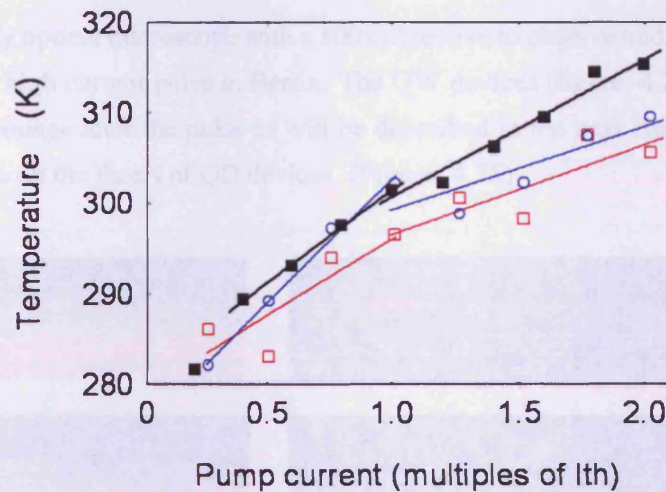


FIGURE 4.23: Comparison of the top window determinations at room temperature, for two pulse lengths, with fitted lines (red squares (340 ns) and blue circles (1000 ns)) with facet temperature of a ridge device for 1000 ns pulses (black points and lines). Even with scatter in the data, a larger temperature increase is seen at the facet

of increasing the pulse length, causing a slight bulk temperature increase, in both the facet temperature measurements and the P-I characteristics, but not in the top window temperatures.

There is thus some evidence to support a higher rate of temperature increase on a QW than a QD facet. I measured an increase in the QW facet temperature, with a change of slope at threshold (at the onset of reabsorption of high lasing light intensity) which was dependent on pulse length and on the degree of absorption for two different devices. The QD measurements showed no clear change at threshold. A measurement of temperature from spontaneous emission from a top window, where no facet temperature effects would be seen, showed an apparent increase in

temperature, but lower than that at the facet. I will now discuss the evidence from microscopic analysis that shows facet damage occurs in QW but not QD based devices.

4.4 Optical and electron microscopy of damaged devices

After the initial facet damage additional damage is sustained due to continued application of current [15]. To separate these two processes I prepared sets of devices and aged them with a single high current pulse of up to 40 A, using a fresh device for each pulse. I used these for the time resolved studies discussed in the next chapter and also carefully analysed the damage to the facets.

4.4.1 Optical microscopy of facets of devices taken to catastrophic optical damage

I used a high quality optical microscope with a 100x objective to observe and photograph devices aged with a single high current pulse in Berlin. The QW devices (figure 4.24) showed obvious and severe facet damage after the pulse as will be described in the next chapter. There was no observable damage on the facets of QD devices. (Figure 4.25).

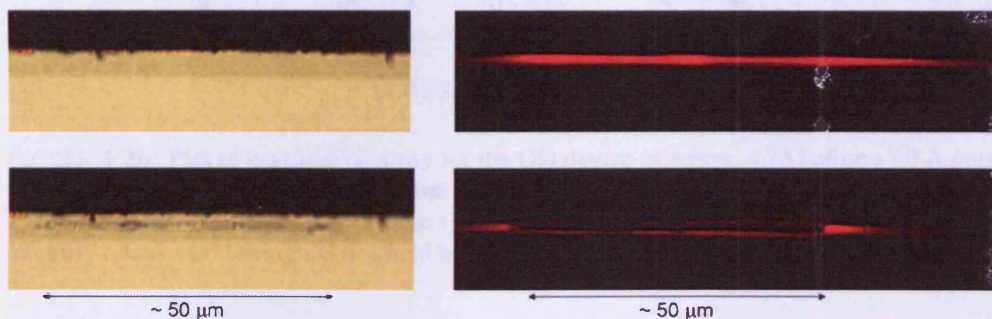


FIGURE 4.24: Images of the QW facets (left) and nearfields (right) taken before (above) and after (below) aging with a single high current pulse. The scale is the same in all images, which have been cropped to show the region of interest. The facet images are about $70 \mu\text{m}$ wide. The nearfields extend beyond the $50 \mu\text{m}$ stripe

The nearfields of the QD devices were analysed by being converted to greyscale and profiles taken of the resulting images. After the pulse I increased the current and pulse width to intensify the remaining spontaneous emission and used these values to estimate the factor by which the emission intensity had dropped. (Figure 4.26). A clear reduction is seen in the nearfield intensity showing that the quantum dot devices have significantly degraded even though no facet damage is observed.

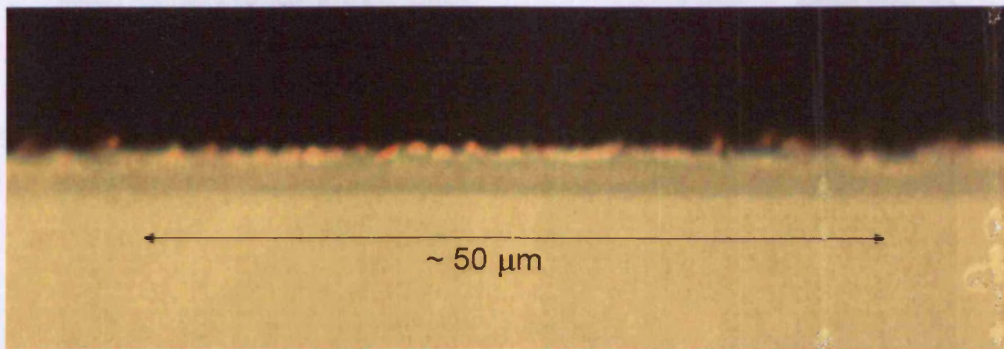


FIGURE 4.25: Image of the facet of a QD device after aging with a single 10 A pulse. No obvious damage can be seen

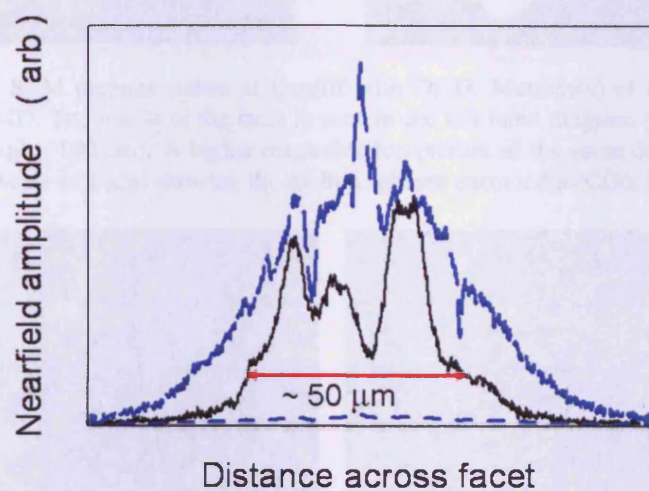


FIGURE 4.26: Plot of nearfield intensity for the QD device in figure 4.25 before a 10 A pulse (black solid) and after (blue dashed), but obtained by increasing the pumping conditions by a factor of 38.5. The blue dotted curve (blue dashed curve divided by 38.5) shows the true intensity relative to the original nearfield before pulsing

4.4.2 Electron microscopy

Scanning electron microscopy (SEM) on multiply pulsed broad area devices after COMD showed the facets of QW devices had sustained the severe damage typical of COMD, with voids and extruded molten spheres (figures 4.27 and 4.28, left). Damage to the QD facets (Figure 4.28, right), on the other hand, appeared relatively slight.

Detailed SEM examination was carried out on the facets of single pulse devices by Dr U. Zeimer at Ferdinand-Braun-Institut (FBH) using the back scattered electron (BSE) technique. This technique gives sharper, clearer images. The QD devices occasionally showed a small area of classic COMD under SEM, but not optical microscopy. Sometimes the damage originated at a cleave step (figure 4.29). The single pulse QW devices always showed substantial damage (figure 4.30) under both optical and electron microscopy. There was a tendency to see somewhat

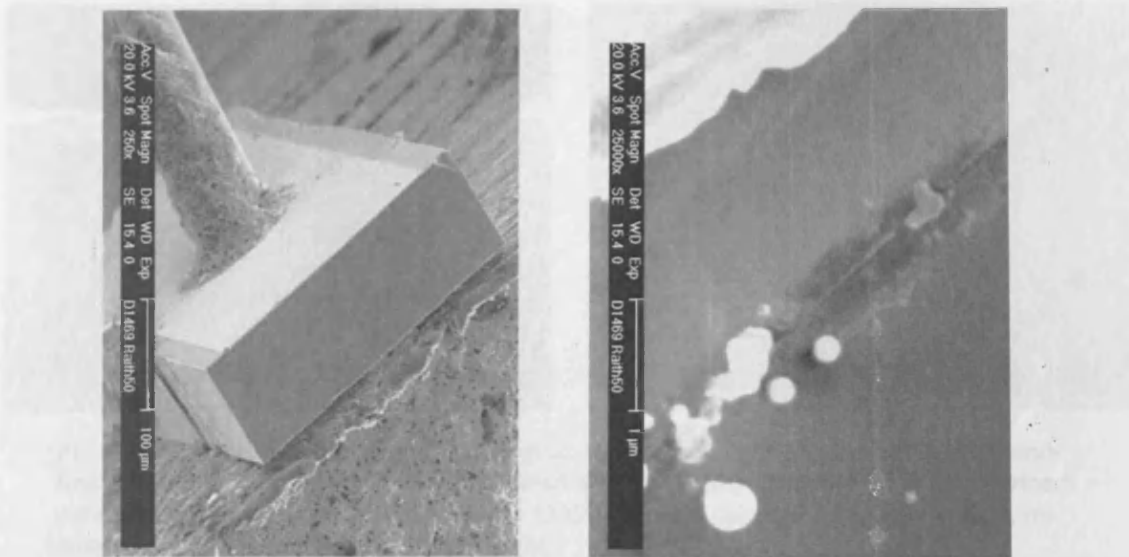


FIGURE 4.27: SEM pictures (taken at Cardiff with Dr D. Matthews) of a device that had undergone COMD. The whole of the facet is seen in the left hand diagram (the scale is given on the left hand diagram - 100 μm). A higher magnification picture of the same device is shown on the right hand (scale of 1 μm) showing the molten spheres extruded as COMD took place

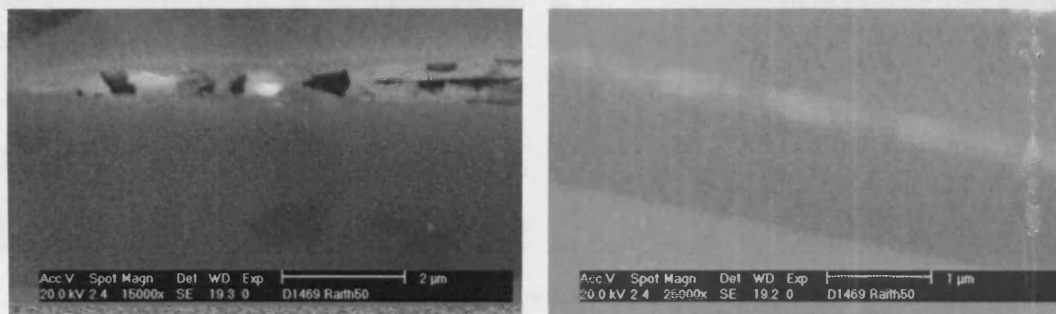


FIGURE 4.28: SEM pictures (taken at Cardiff with Dr G. Edwards) after catastrophic damage, showing the more extreme damage sustained under the oxide stripe in a QW device (left), with dark and light areas and linear regions that may indicate damage at the quantum wells themselves. The QD device (right) showing the more diffuse and less severe damage seen in all QD devices examined by SEM, possibly related to stacked dots

more damage on the p-side of QW devices, as has been previously observed in the literature [73] (indicated by an arrow).

Occasionally evidence of very large stacked dots (figure 4.31) could be seen and are possibly responsible for the structure seen in figure 4.28. Stacked dots InAs have been grown in GaAs [74] by using a narrow spacer layer.

It can be seen from these images the changes seen at the facet of QD lasers are of a different type to the classic COMD seen on QW facets, although this can sometimes occur. The facet damage often appears to be more severe than in QW, with large areas of very obvious damage (described and analysed in the next chapter). Microscopic examination of the facets of the devices showed equally good quality facets in the QW or the QD devices, with no obvious flaws which could

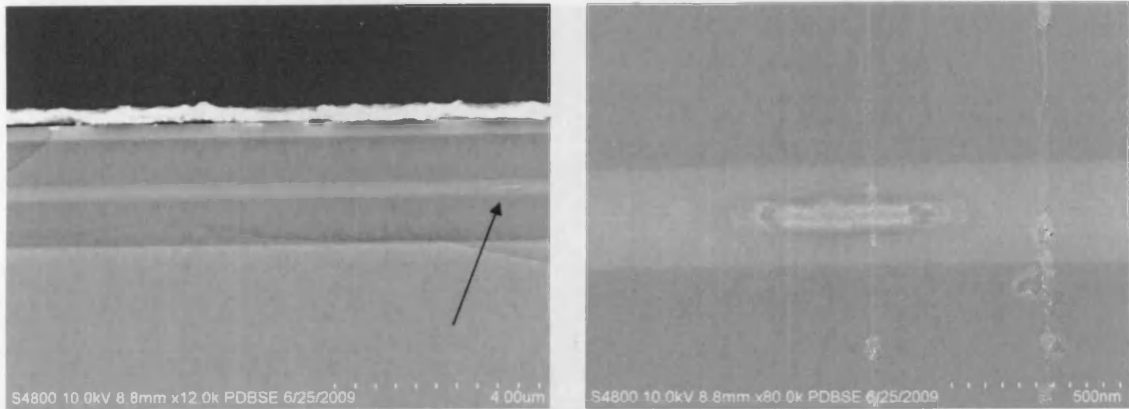


FIGURE 4.29: SEM of the facets of single pulse QD devices (by Dr U. Zeimer at Ferdinand-Braun-Institut (FBH)) using the back scattered electron (BSE) technique. The QD devices occasionally showed a small area of classic COMD (arrow) under SEM, but not optical, microscopy. The damaged area is enlarged (right).

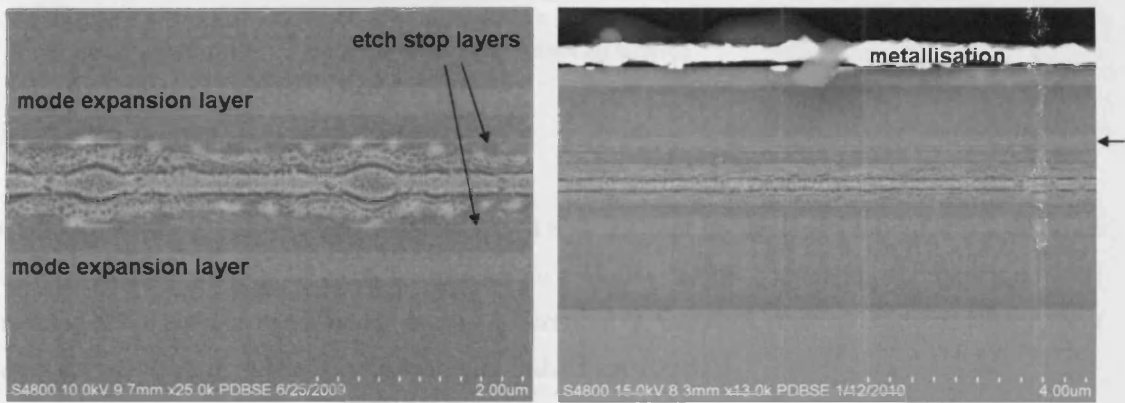


FIGURE 4.30: SEM of the facets of single pulse QW devices (by Dr U. Zeimer) using the BSE technique. The p-side is at the top of the image. The mode expansion layers and the etch stop layers, which show slightly more damage than the surrounding region, can be seen. More damage is visible on the p-side of the device, in the mode expansion layer (arrow).

trigger COMD. Figure 4.30 shows uniform damage over all of the active area. Previous studies have linked facet damage to filament peaks in the nearfield [50]. It was not possible to do this for QD devices using optical microscopy. In both optical microscopy and scanning electron microscope pictures (SEM) the QW structures showed much greater contrast between different spatial regions on the facet compared to QD, with regions varying from black to white through shades of grey at the quantum well area of the facet in the pumped area under the stripe. Multiply pulsed QW devices also showed the presence of ejected spheres of molten material, which were not seen in QD devices or singly pulsed QW devices. SEM images of the facet of QD devices that had undergone COMD showed more diffuse (the focus of these images is sharp) and less severe damage with less colour contrast than a QW structure.

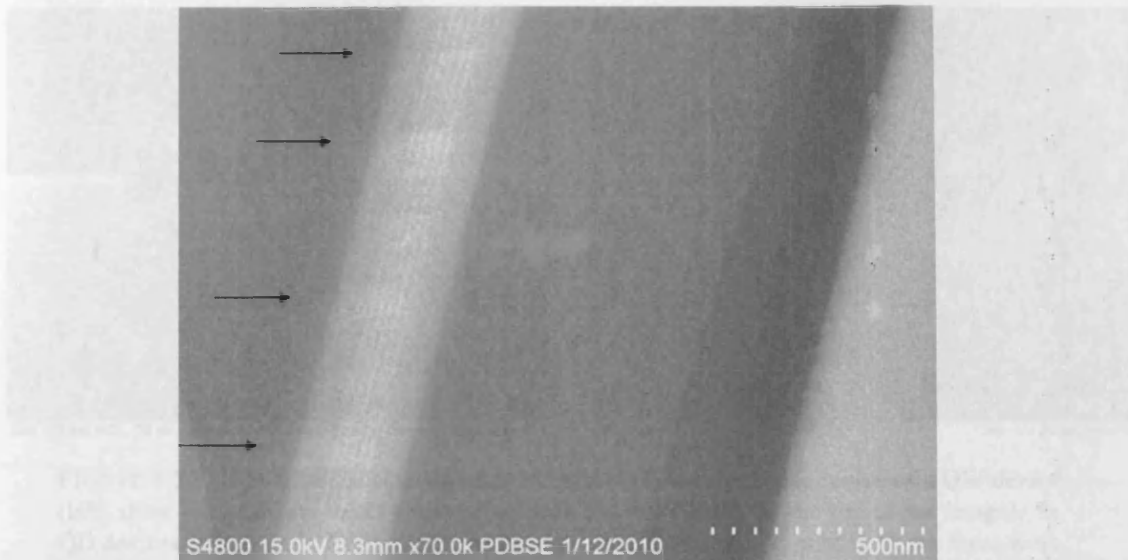


FIGURE 4.31: SEM of the facet of a QD device showing no damage, but evidence of very large stacked dots (arrows). (The image has been autobrightened.)

4.4.3 Cathodoluminescence

Cathodoluminescence was then performed by Dr U. Zeimer on devices I mounted p-side down and subjected to single 10 A pulses at a range of pulse lengths, revealing the damage to the interior of the devices to be fundamentally different in QW and QD devices. Severe classic facet damage was seen on one of the QD samples pulsed for 10 us.

Panchromatic cathodoluminescence (PCL) of the devices revealed the presence of a molten defect propagating back from the facet in a QW device (figure 4.32 (left)) as is widely reported in the literature on COMD [12, 32] and discussed in Chapter 2, but the QD devices showed a different type of effect that consisted of dark spots of varying size, uniformly distributed over the growth layer of dots, which became darker and larger under the stripe (figure 4.32 (right)) where the material is subject to both light and current. In QD devices neither increase in effect near the facet, nor any propagating molten regions were seen. I concluded, on the basis of the evidence from these three types of analysis: optical microscopy, SEM and PCL, that the damage to QW devices occurs at the facet and the damage to QD devices occurs in the interior of the device.

Dark non-radiative spots such as these have been observed in structural analysis of In(Ga)As self assembled quantum dots [68], where they have been associated with defects which grow during aging studies. It is this effect that I propose as the main mechanism for catastrophic damage in quantum dot based devices. I will now support this proposition with evidence from photocurrent (PC) and laser beam induced current (LBIC) studies.

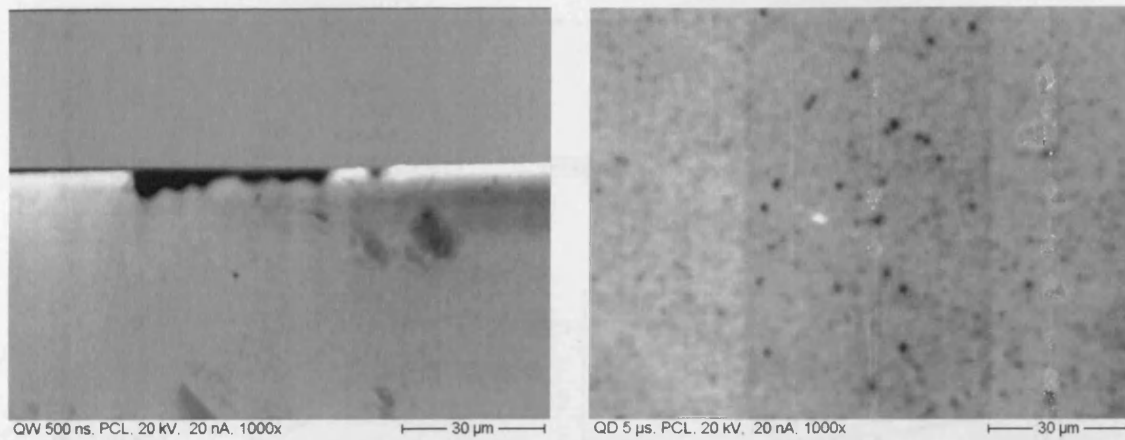


FIGURE 4.32: Panchromatic cathodoluminescence (PCL) of the active region of a QW device (left) showing a molten defect propagating back from the facet (at the top of the image). In QD devices (right) dark, non-radiative spots were seen across the layer of dots, but these were larger and darker under the stripe. The images are in the plane of the active region, looking from the n-doped side.

4.5 Photocurrent and LBIC measurements

Photocurrent (PC) measurements of my single pulse devices (carried out by Mr R. Giri at MBI) suggested damage might be occurring in the spectral region associated by measurements in Cardiff with very large dots [75]. Aging experiments and PC on more of my samples from the same structures (also at MBI, by S. Schwirzke-Schaaf and R. Giri) supported this idea. Photocurrent spectra of aged devices tend to show a decrease in amplitude in regions of interband transitions and an increase in spectral regions where the emission is due to defects, in the band-gap.

4.5.1 Photocurrent studies on 1000 ns, single pulse devices

Photocurrent spectra were taken of my single pulse QD devices (by Mr R. Giri, at MBI) (figure 4.33).

I normalised these spectra to the barrier region (2.15 eV). There is a reduction in the amplitude in the regions associated with large dots, at 1.7 eV (ground state) and 1.75 eV (excited state). There is a general trend towards the greatest reduction at the lowest current, which seems at first surprising, but at the lower currents the devices lased for a longer fraction of the 1000 ns pulse, subjecting the material to the action of intense light. Out of eight devices, two did not fit the trend. The alignment can differ from device to device, but random variations in positioning are unlikely to cause the trend of the majority of the devices in the appearance of the data, although it is possible.

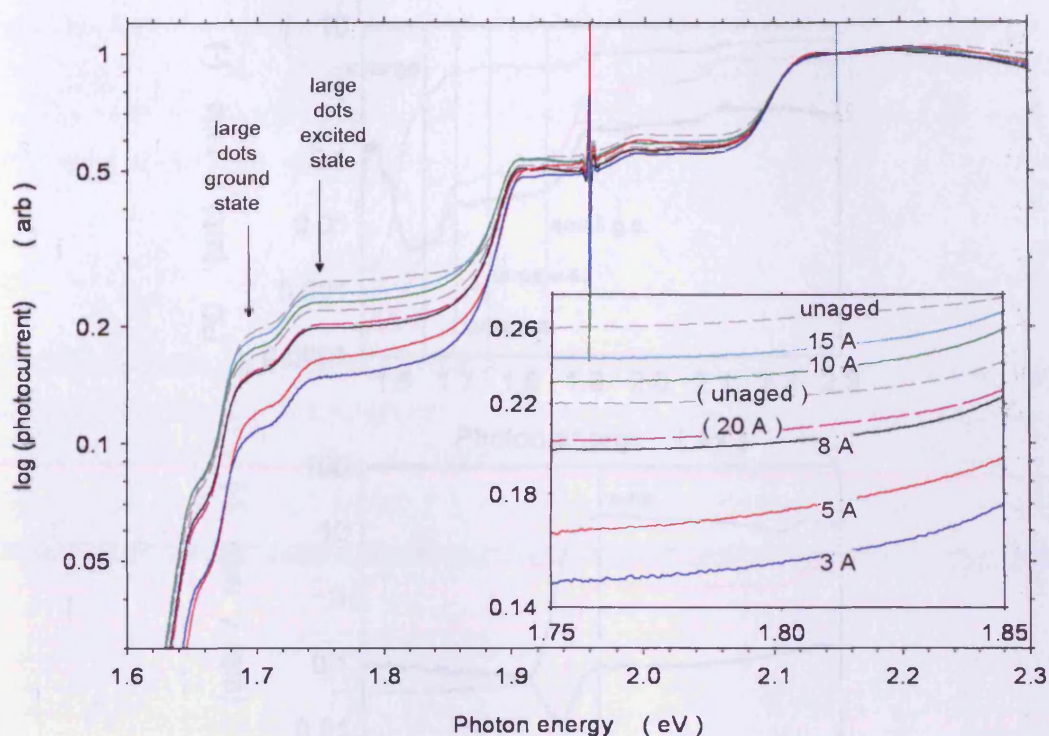


FIGURE 4.33: Photocurrent spectra of my single (1000 ns) pulse QD devices over a range of currents, plus two unaged devices (see detail). (Data taken by Mr R. Giri, at MBI). I normalised these spectra to the barrier region (2.15 eV). There is a reduction in the amplitude in the regions associated with large dots. There is a general trend towards the greatest reduction in amplitude at the lowest current. Out of eight devices, two did not fit the trend (20 A and one unaged device).

To investigate this further, a new set of devices was aged at a low light level for a longer time, and photocurrent measurements repeated.

4.5.2 Photocurrent studies on aged devices

The devices were aged for a total time of 2h 10m. The aging consisted of operating the devices just above threshold using short pulses (to minimise heating) of 600 ns at 300 mA, at 10 kHz. The aging took place in three sessions, interspersed with Raman measurements, (all carried out by Ms S. Schwirzke-Schaaf) which took about an hour, and also have an aging effect. PC spectra were taken before and after the aging (by Mr R. Giri). A similar, comparison experiment was carried out with QW devices, aged at 950 mA in 200 ns pulses, chosen to give the same energy per pulse as for the QD devices.

The photocurrent spectra for QD and QW devices are shown in figure 4.34. The ratios of after/before amplitudes are given in black. Interband transitions are given in green. Comparison of the spectra before and after aging showed a uniform reduction in PC intensity over all photon energies for both QW and QD devices, but also a particularly large reduction in PC intensity in

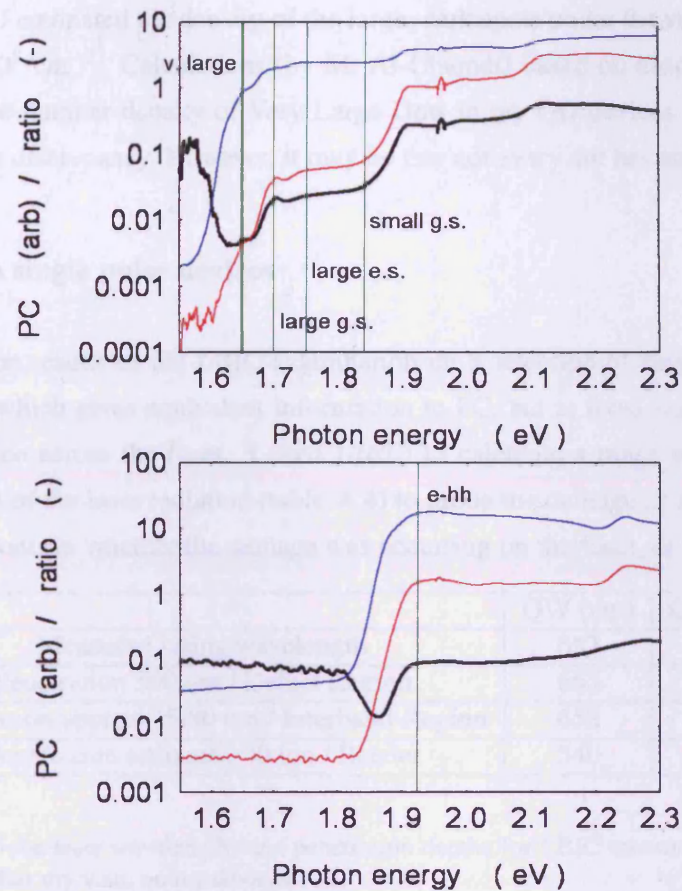


FIGURE 4.34: Photocurrent spectra for QD (top) and QW (bottom) devices, before (blue) and after (red) aging with low current repeated pulses for two hours. Additional aging was caused by a Raman probe laser. The ratios of after/before amplitudes are given in black. Interband transitions are given in green (very large dots: 1.66 eV, large dot ground state: 1.7 eV, large dot excited state: 1.75 eV and small dot ground state: 1.84 eV). Particularly severe aging occurred in the spectral region associated with very large dots in the QD devices

the region of the QD spectrum associated with very large dots [75, 76], (figure 4.34). (The QW devices showed a uniform decrease apart from a region centred on about 1.865 eV, which has sometimes been seen as a shoulder on the QW exciton peaks in EPVS measurements at Cardiff, but will not be discussed further here.) The reduction in the PC signal is due to the formation or exacerbation of defects [77]. A study of life-tested InAs:InGaAS dot-in-a-well structures [68] found that perhaps one in 500 dots had defects associated with them that arose during growth, which could grow during aging, and suggested the density of defective dots corresponded with the density of so-called large dots in their structure, and that it might be possible to eliminate the defects completely by varying the growth conditions. My data shows the presence of very large, stacked dots (figure 4.31), and evidence of more severe damage (figure 4.34) in the spectral region that has, in previous Cardiff work [75], been associated with Very Large Dots. It is possible the damage mechanism I observed in the QD devices is growth of pre-existing defects associated with dots, and the PC aging spectra suggest the defects are associated with

Very Large Dots. I estimated the density of the large, dark spots under the stripe in figure 4.32 to be about $4 \times 10^5 \text{ cm}^{-2}$. Calculations (by M. Al-Ghamdi) based on absorption curves [78] have suggested the number density of Very Large Dots in my QD devices are of the order of 10^{10} cm^{-2} , a large discrepancy. However, it may be that not every dot has an associated defect.

4.5.3 LBIC on single pulse devices

Lastly I present the results of the LBIC examination on a selection of single pulse aged QW and QD devices, which gives equivalent information to PC, but at fixed wavelengths and as a function of distance across the facet. I used $1/(\alpha\Gamma)$ to calculate a range of wavelengths and penetration depths of the laser radiation (table 4.4) to probe the damage as a function of depth. This would help confirm whether the damage was occurring on the facet, or inside the device.

	QW (nm)	QD (nm)
Measured lasing wavelength	657	720
Penetration 500 μm / Defect Region	663	740
Penetration approx 75-80 μm / Interband Region	652	710
Penetration estimated 30 μm / Barrier	540	540

TABLE 4.4: Probe laser wavelengths and penetration depths for LBIC measurements (carried out in Berlin after my visit, on my devices)

LBIC spectra at the three wavelengths and penetration depths are given in figures 4.35 and 4.36. I normalised the spectra to the amplitude outside the stripe at the front facet and looked for a dip in the centre, at the stripe, that changed as a function of penetration depth into the device.

The normalised LBIC scans across the facet of single 1000 ns pulsed QW devices give the smallest signal under the stripe for the 540 nm radiation, which is more strongly absorbed, showing the highest level of damage is at the facet. The QD devices, however, do not show any difference in signal with depth into the device. The conclusions I have drawn from this data agree with PCL evidence, which reveals damage originating at the facet in QW devices and uniform damage throughout in QD devices.

4.6 Discussion

4.6.1 Summary of evidence

To establish firstly whether the peak power density at catastrophic optical mirror damage (P_{COMD}) is higher in QD devices I subjected QW and QD devices to repeated current pulses at increasing values of current until they failed catastrophically (signalled by an abrupt and permanent drop

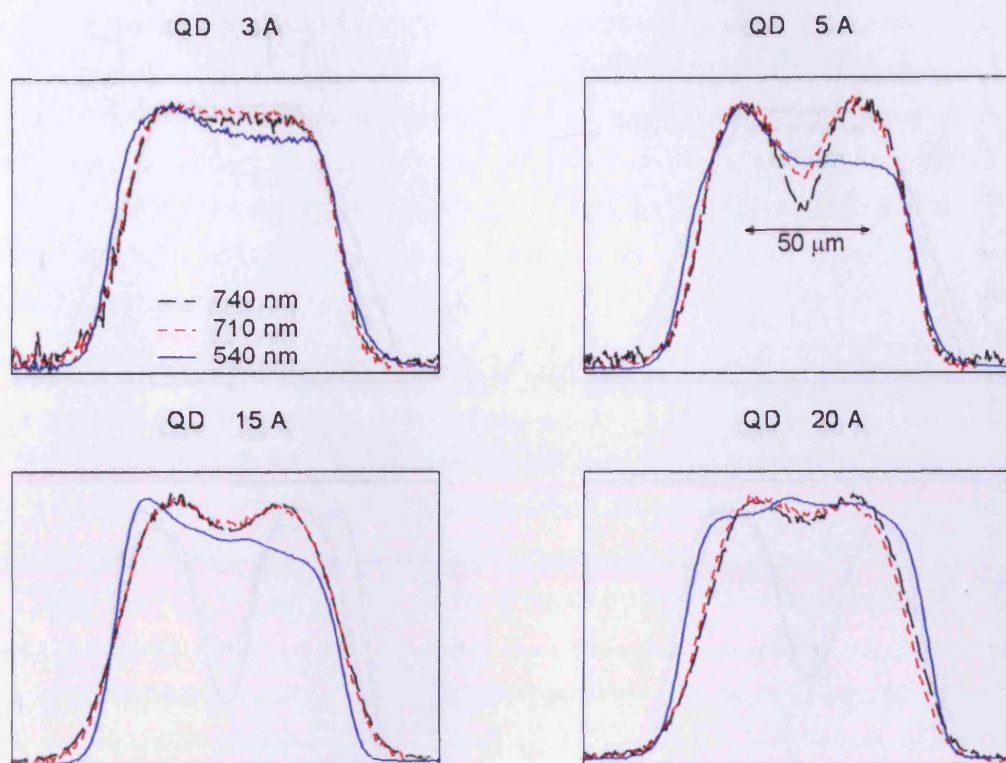


FIGURE 4.35: Normalised LBIC scans across the facet of single 1000 ns pulsed QD devices for a range of laser wavelengths and penetration depths. Apart from the 5 A device the damage level is similar at all depths

in power output). Comparing values of P_{COMD} I found that this limit was indeed higher in QD based devices, but only at the shorter end of the pulse length range used (about 400 ns). This could be due the effect of bulk sample heating: different thermal properties in the QD devices could mean they are more sensitive to the effects of heating, resulting in a relatively quicker loss of performance with pulse length than QW devices. However, lasing wavelength measurements at currents up to twice threshold appeared to confirm negligible (less 0.8 K and 2 K for QW and QD, respectively) temperature rise in both types of device, or at least no gross difference between QW and QD, although some effect on temperature was seen in measured P-I characteristics at different pulse lengths.

Microscopic examination revealed severe facet damage in QW devices, with evidence of clearly defined regions of different colour (the cause of which could be a difference in conductivity or topography) on the surface, and of extruded molten spheres, associated in the literature with melting of the facet. The QD devices, however, did not show the same degree or type of damage.

The non-appearance or reduced appearance of facet damage in QD devices should be accompanied by other evidence such as, for example, a reduced degree of facet temperature rise, an essential pre-condition to COMD. I measured the facet temperature by fitting to the high energy Boltzmann tail of the spectrum of spontaneous emission from the facet at an angle to the

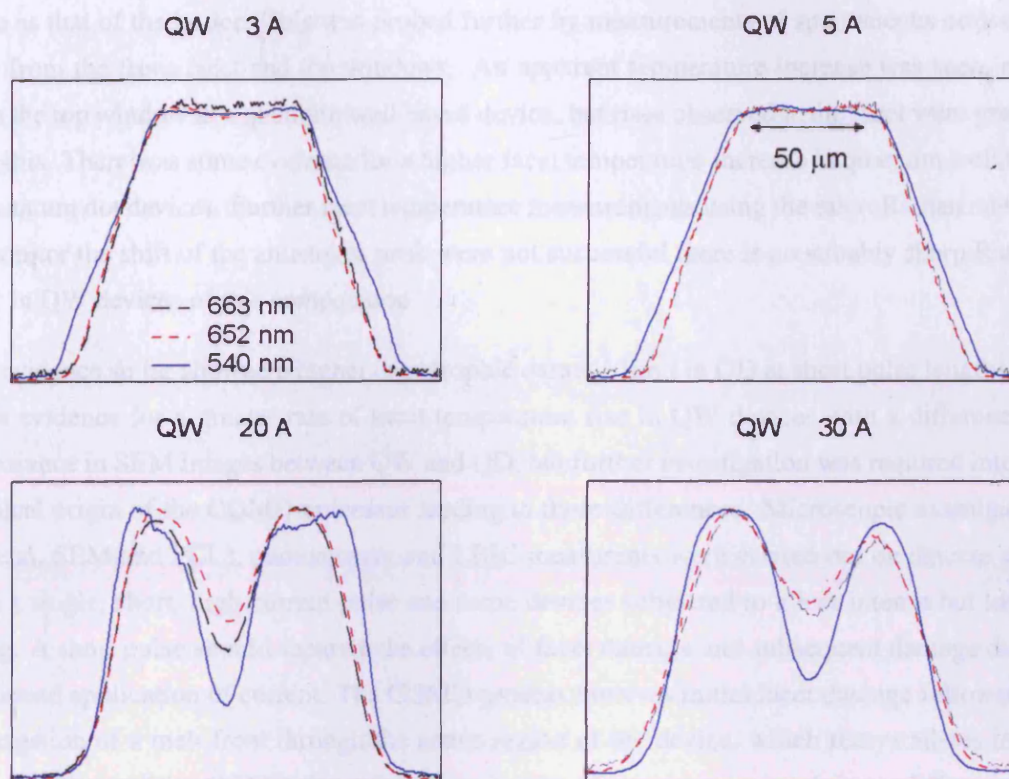


FIGURE 4.36: Normalised LBIC scans across the facet of single 1000 ns pulsed QW devices for a range of laser wavelengths and penetration depths. Where damage is seen (corresponding to 8 A and above, when facet damage was observed, as described previously), the signal is smallest under the stripe for the 540 nm radiation, which is more strongly absorbed, showing the highest level of damage is at the facet

main laser beam. Observations by this method of temperature rises up to the melting point of GaAs have been reported in the literature [28]. This is further discussed in section 4.6.3. The method has some advantages over the other methods commonly in use such as microRaman or thermoreflectance in that there is no requirement for a probe laser beam, which causes heating of the facet. This is then an artifact of the experiment, rather than the effect being observed. Previous studies using the microRaman method [25] have shown the rise in facet temperature is significantly lower in QD devices. I found a greater facet temperature rise in the QW devices measuring between 1x and 2x threshold current, using specially fabricated ridge lasers to ensure good beam shape with less of the non-uniformity due to lateral modes and filamentation that is found in broad area devices, and more precise knowledge of the location to be monitored. To obtain the net temperature rise at the facet I monitored the lasing wavelength, which showed the bulk temperature rise of the devices was small compared to the measured facet temperature rise, confirmed by temperature measurements of lasing wavelength shift as a function of temperature in a cryostat. Various uncertainties existed in these measurements. The threshold current of the devices differed between the QW and the QD which would therefore suffer a different degree of Joule heating. I assumed the electron temperature, which is measured by this method, was the

same as that of the lattice. This was probed further by measurements of spontaneous emission, both from the front facet and top windows. An apparent temperature increase was seen, even from the top window in a quantum well based device, but rises observed at the facet were greater than this. There was some evidence for a higher facet temperature increase in quantum well than in quantum dot devices. Further facet temperature measurements using the microRaman method to monitor the shift of the antistokes peak were not successful there is no suitably sharp Raman peak in QW devices of this composition.

The evidence so far showed a higher catastrophic damage limit in QD at short pulse lengths and some evidence for a greater rate of facet temperature rise in QW devices with a difference in appearance in SEM images between QW and QD, but further investigation was required into the physical origin of the COMD processes leading to these differences. Microscopic examination (optical, SEM and PCL), photocurrent and LBIC measurements were carried out on devices aged with a single, short, high current pulse and some devices subjected to a less intense but longer aging. A short pulse should separate the effects of facet damage and subsequent damage due to continued application of current. The COMD process involves initial facet damage followed by propagation of a melt front through the active region of the device, which recrystallizes into a non-radiative region. COMD thus takes place in several time stages, involving a different process at each stage. (I also monitored the light pulses emitted from these devices and discovered a difference in the temporal behaviour of the damage in QW and QD, which will be discussed in chapter 5.) Again, severe damage was sustained by the facets of the QW devices, with corresponding effects in the nearfield, but relatively little damage could be seen on those of the QD devices although the nearfield intensity decreased greatly after the pulse. These findings were confirmed by SEM of the facets. Some damage seen in QD devices originated at a flaw such as a cleave step. Dr Zeimer's images also revealed the presence of some large, stacked dots in the QD wafers, which could be implicated in the damage processes.

Many factors affect the amplitude of a measured photocurrent signal including the effects of aging. The spectra of aged devices can reveal a reduction in photocurrent signal in the region of interband transitions and a growth in signal in the bandgap, a region associated with aging related defects. Photocurrent spectra can thus be used to study the effects of aging or degradation in a device. It has been shown that the ratio of aged to unaged signal, at a fixed photon energy, decreases steadily with time, to a value of the order of 0.15 at an aging time of 10 hours, for example [49]. My devices, of a different structure and aged less than this, gave a signal decreased to about 0.1 in QW, consistent with what was expected, but some regions of the spectra showed a greater decrease. In QW a previously unidentified shoulder on the absorption edge showed a slightly larger drop, but in QD the regions between 1.6 and 1.85 eV decreased by nearly another order of magnitude. These regions have been identified from absorption spectra as being associated with dot states from a trimodal size distribution [75], with a small spectral component from Very Large Dots, which showed the largest decrease to 0.004 of the unaged signal size.



It seemed the degradation processes had a bigger effect on quantum dots than quantum wells, which showed a similar decrease in both the QW and the QD structures, with the greatest effect seen in the Very Large Dots. Could these be the large, stacked dots identified in the SEM images of the facets? PC carried out on the devices aged with a single pulse revealed only small, if any change. PCL of pulsed devices showed dark spots which were larger and darker under the stripe. Similar spots have been seen in 1.3 μm emitting InGaAs quantum dot structures after accelerated life testing [68]. These were found to be caused by defects associated with the quantum dots which grew during the life test. It seems possible a similar mechanism is operating here. In contrast PCL of QW devices showed the classic COMD damage originating at the facet and propagating back along the active region.

LBIC evidence gave support to the idea that damage originated at the facet in QW and in the interior in QD. An LBIC measurement gives similar evidence to PC, but is scanned across the device at fixed wavelength giving the spatial distribution of damage. Two wavelengths were chosen to give two different penetration depths into the device. Comparison of normalised data showed damage in all devices was evident under the stripe above the threshold for catastrophic degradation, and in the QW was much more evident on the facet but in QD the damage was uniform throughout.

4.6.2 The proposed explanation

A potential explanation for the difference in catastrophic degradation properties in QD and QW consistent with the evidence I have presented, is that QW degrade by COMD and that QD degrade by growth of defects associated with the dots themselves. The evidence suggests the damage to the QD devices occurred in the interior, and could be associated with very large dots. Evidence for this type of degradation has been found in 1.3 μm InAs dots [68] and attributed to growth of defects. The presence of the very large dots is affected by the growth temperature, thus a change in growth conditions could prevent this damage mechanism [68]. The power density limit obtained in the original catastrophic damage measurements is the COMD limit for QW devices. The QD facets rarely showed evidence of COMD but degraded by another mechanism and do thus appear to have more resistance than QW facets to catastrophic optical mirror damage. The power density I measured in the original multiple pulse experiments, described earlier in this chapter, was thus below the COMD limit, which therefore has a higher value than that measured here.

4.6.3 Discussion

There is clearly a need, in general, to carefully examine the nature of the damage to facets, rather than merely observing an abrupt power drop in the P-I characteristic and attributing this to

COMD as is sometimes done in the literature. A previous study of COMD in QD, but in different material systems [79], found COMD, confirmed by optical interference contrast microscopy, at high levels, comparable with those for QW, but their devices were operated cw or quasi-cw. I found my repetitively pulsed measurements at longer pulse lengths gave similar damage limits for QW and QD, with SEM evidence of mirror damage for a 10 μ s pulse. It is possible that damage due to internal heating is a contributing factor to the device failure, as well as absorption of light, when all but the shortest single pulses are used. In addition, optical microscopy is obviously less sensitive than SEM for determining the exact nature of the damage: I could not see damage to the facets of QD devices with the optical microscope for single pulse measurements, but could occasionally see small amounts with SEM.

It has been suggested the critical temperature increase is about 20 K [12] or 120-140K [18]. Once this temperature is reached thermal runaway takes place, with a temperature rise to the melting point of over 1000 ° C on the timescale of nanoseconds [12], followed by catastrophic damage at a timescale of tens or hundreds of nanoseconds, which has been previously inferred from thermocamera facet temperature measurements [19] and has now been measured directly, as will be discussed in the next chapter. Real time temperature measurement would need to take place on this timescale. How is it possible for temperature rises up to hundreds of degrees to be measured, as reported in the literature? An average temperature can be measured using a thermal camera which monitors the thermal radiation, averaged over the data collection time (2 ms) and over the dimensions of the whole of the laser cavity. If these and the duration of the thermal flash [54] are known the peak temperature can be inferred. Temperatures of 260-320°C, assuming a timescale of 100 - 200 ns for the duration of the high temperature, have been obtained this way [19]. Using a measured timescale of 30 - 400 ns, temperatures of 1000 - 2000 (\pm 200) °C have been measured [80]. Methods such as microRaman, or the use of the high energy Boltzmann tail of the spontaneous emission are more precise, but require the temperature to remain constant throughout the measurement and, as such, are suitable for measurements of facet temperature rise at low pumping currents, when the temperature is likely to remain stable.

Chapter 5

Time resolved studies of COMD in quantum well based devices

5.1 Introduction

Much research effort continues to be invested to lead to technological improvements that will not only raise the power levels attainable but detect the imminence of COMD before it actually occurs, thus making damage preventable. The time taken for the power level to drop to non lasing levels has been inferred to be of the order of hundreds of nanoseconds in previous studies that have been carried out at microsecond resolution [19, 34, 81]. In order to confirm these estimates and provide information that could be used to prevent permanent destruction of a device by COMD better time resolution is needed. By using a fast photodiode I was able to measure these times, and to monitor the changing light intensity during COMD on the timescale of tens of nanoseconds. This resolution would be necessary for protective measures to be effective. A description of the experiment and results follows. I carried out these measurements as part of a collaboration with Dr. Jens Tamm's group in Max-Born-Institut.

Using devices from the same structures used for COMD studies described earlier, with as-cleaved facets, so that the COMD process was not affected by any facet treatment, and the AlGaInP material system, which is susceptible to COMD, I applied single, high current pulses, which should be long enough to cause COMD, but little or no subsequent collateral damage. I obtained the time for the drop in light intensity from the photodiode signal and measured the area of damage to the facet using images from high quality microscope, both as a function of current. In the current range up to 40 A, the total COMD process up to the drop of light intensity to non-lasing levels took place on a timescale of hundreds of nanoseconds, gradually shortening as the optical power increased but remaining finite even at very high powers, with a limiting value of 200 ns. The measured area of facet damage showed a clear increase with drive current.

Using a straightforward thermal model based on melting point curves I explain the limiting time at high currents and the relationship between the time to COMD and the area of damaged facet material in the following way.

The total time to COMD consists of the time to raise the facet temperature, which shortens as power increases, plus the time to cause the damage. Since the area, and hence volume, of damaged material increase with current, the amount of energy used to cause the damage also increases. The time taken to absorb this increasing amount of energy does not increase, however, but remains constant, since the power and hence rate of absorption also increase with current. The total time thus tends to this constant value at high powers.

5.2 Sample and experimental details

5.2.1 Choice of wafer

Many facet treatment processes exist to protect facets and increase the power density a laser can sustain before COMD occurs. In order to investigate the physics of COMD itself, I used red-emitting AlGaInP based lasers, which are known to be susceptible to COMD, with as-cleaved facets. Thus any effects seen were due to the intrinsic properties of the facets themselves with no change due to passivation, non-absorbing mirrors or coatings, which would improve the performance but obscure the physics. Large regions of damage and thus very clear results were obtained. The devices, red emitters originally designed for medium power optical storage use, consisted of three compressively strained GaInP quantum wells in an AlGaInP waveguide and used mode expansion layers to decrease the beam divergence. They have been fully described in Chapters 3 and 4.

5.2.2 Device mounting and initial characterisation

I mounted identical 50 μm oxide isolated stripe devices (300 μm wide and 120 μm deep with a cavity length of 1000 μm) p-side up on copper heat sinks on transistor headers as described in Chapter 2. For these high power experiments, where there was a danger of the electrical contacts failing before COMD, I used multiple gold wires for the p contact with the normal copper heatsink for the n side attached with conductive epoxy. This mounting was adequate heatsinking for the short times of the current pulses used. A characteristic length for conduction of heat for this material, given by $\sqrt{(\kappa t)}$, where κ is the thermal diffusivity and t is the pulse length, is of the order of 1-2 μm and is thus much smaller than the sample dimensions. Initial characterisation gave a mean threshold current of 521 (± 17) mA averaged over 26 devices (using the standard deviation as the error.) The lasing wavelength of a sample of devices was

656.6 (± 0.4) nm. I recorded images of the nearfields and facets both before and after making the single pulse measurements of time to COMD. I mounted some devices p-side down, but with similar technique, to obtain a device for cathodoluminescence imaging of the damage to the interior.

5.2.3 Experimental setup for time resolved measurements

The standard setup in Berlin can be used to apply single, square, high current (35 A) pulses, with simultaneous thermal and nearfield imaging of the facet. COMD is detected by the presence of *thermal flashes* or temperature spikes [19, 54]. I amended this setup to increase the time resolution from the 7 μs used in thermal imaging to a measured 18 (± 2) ns in this investigation (figure 5.1), by using a fast photodiode in place of the thermal imaging and nearfield cameras and detecting COMD by the drop in light level. The setup and experimental details are described in Chapter 2.

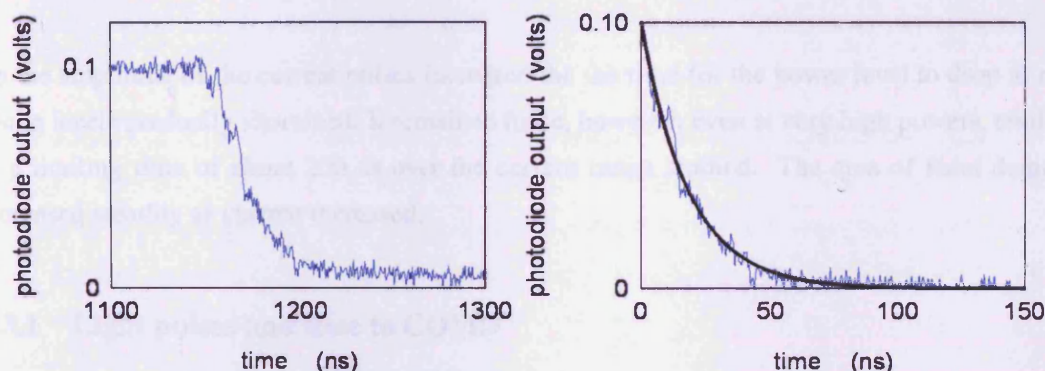


FIGURE 5.1: Left: the end of a raw photodiode trace for a 5 A, 1000 ns current pulse, showing the end of the light pulse with the exponential decay in signal after the current was switched off. Right: the exponential drop at the end, shifted down and fitted with an exponential of the form $\exp(-t/\tau)$. The value of τ was 18 ns

I subjected the lasers to single current pulses of 1000 ns length, at increasing currents of up to 40 A, using a fresh device for each pulse and recording the current and light pulse traces. This should be long enough at most currents used for COMD to occur, while keeping collateral damage (the internal propagation of the melt front) to a minimum. Before applying the current pulse I imaged the nearfields using electroluminescence at pulsed (12 ns), very low currents (about 1 A) at a very low repetition rate in order not to age the device in any significant way. I did this with the microscope illumination both off, which enabled the nearfield to be clearly seen for analysis of area, and on, so that darkened areas in a visible image and areas of reduced nearfield intensity could be correlated. After the devices were damaged it was necessary to increase the pulse length or repetition rate to get a visible nearfield. The amount of the increase gave an indication of the degree of damage. From the oscilloscope traces and images I was able

to obtain the time taken for the optical power from the device to drop, and the area of damage sustained by the facet.

The occurrence of COMD was confirmed by the permanent drop in light level sensed by the photodiode, the extreme reduction in nearfield intensity and the visible damage on the facets. In a supplementary investigation I subjected one device to repeated identical 10 A 1000 ns pulses to provide additional confirmation of the permanent nature of the damage to the device after the first pulse.

Selected devices were sent to the Ferdinand-Braun-Institut where SEM of the facets was carried out by Ute Zeimer, who also carried out panchromatic cathodoluminescence (PCL) of the damage to the interior, in the plane of the active region, on a p-side down device pulsed 12 A for 500 ns.

5.3 Experimental results - time to COMD and facet damage

As the amplitude of the current pulses increased the the time for the power level to drop to non lasing levels gradually shortened. It remained finite, however, even at very high powers, tending to a limiting time of about 200 ns over the current range studied. The area of facet damage increased steadily as current increased.

5.3.1 Light pulses and time to COMD

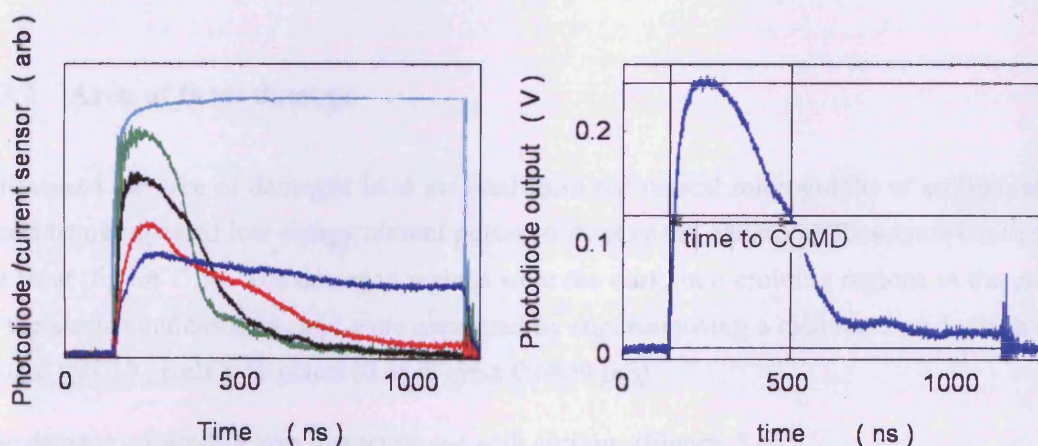


FIGURE 5.2: Left: examples of photodiode traces of increasing amplitude as a function of current for 5 A, 10 A, 20 A and 40 A, showing the drop in light intensity for the higher currents, together with an example of a current trace (top trace). Right: the trace for 15 A, showing how the time to COMD is measured at half the peak height.

For currents of 8 A and above the photodiode signal showed a drop in light intensity to non-lasing levels during the pulse (figure 5.2). I obtained the time to COMD from the photodiode

traces, measuring from the start of the current pulse to the time for the power to drop to half its peak value. Values of time-to-COMD for all currents are given in figure 5.3.

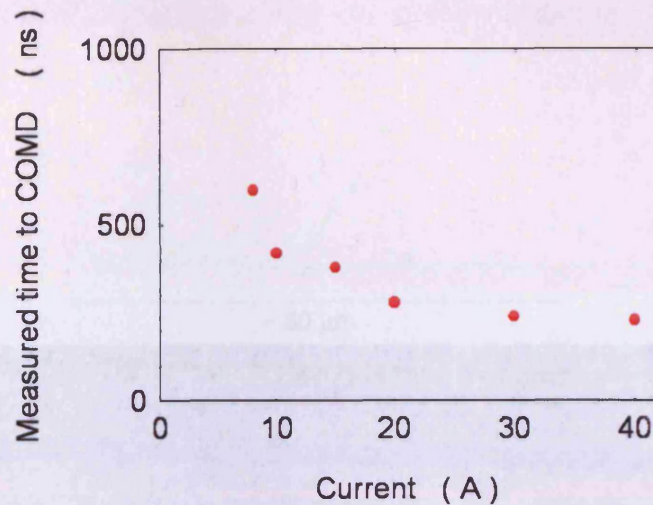


FIGURE 5.3: Measured time to COMD (from start of current pulse to half power) for the devices as a function of pulse current. The time approaches a constant, limiting value of about 200 ns, asymptotically, as current increases

Facet damage was clearly visible in optical micrographs (illuminated with white light) of the facets as a darkened, non-uniform area of the active region in the pumped area beneath the stripe. If I then applied low current, short pulses to the damaged device, the damaged region could be seen as a non-luminescent area in the centre of the red, nearfield electroluminescence. These darkened areas were not observed in images taken of fresh devices before the current pulse was applied, in which the nearfield electroluminescence was uniformly distributed. (Figure 5.4).

5.3.2 Area of facet damage

I measured the area of damaged facet material from the optical micrographs of unilluminated facets using repeated low energy current pulses to display the electroluminescence emitted by the facet (figure 5.5). The damaged regions were the dark, non-emitting regions in the centre of the electroluminescence, and were measured by superimposing a calibrated grid. Each grid square was 10 pixels x 10 pixels ($0.6839 \mu\text{m} \times 0.6839 \mu\text{m}$).

The damage covered an area that increased with current. (Figure 5.6).

The permanent nature of the damage was confirmed by the reduction in the intensity of the nearfield electroluminescence after a single pulse. In a separate experiment in which the same laser diode was subject to repeated identical current pulses, a large drop in light intensity was observed between the first and second current pulses, followed by much smaller changes in subsequent pulses.

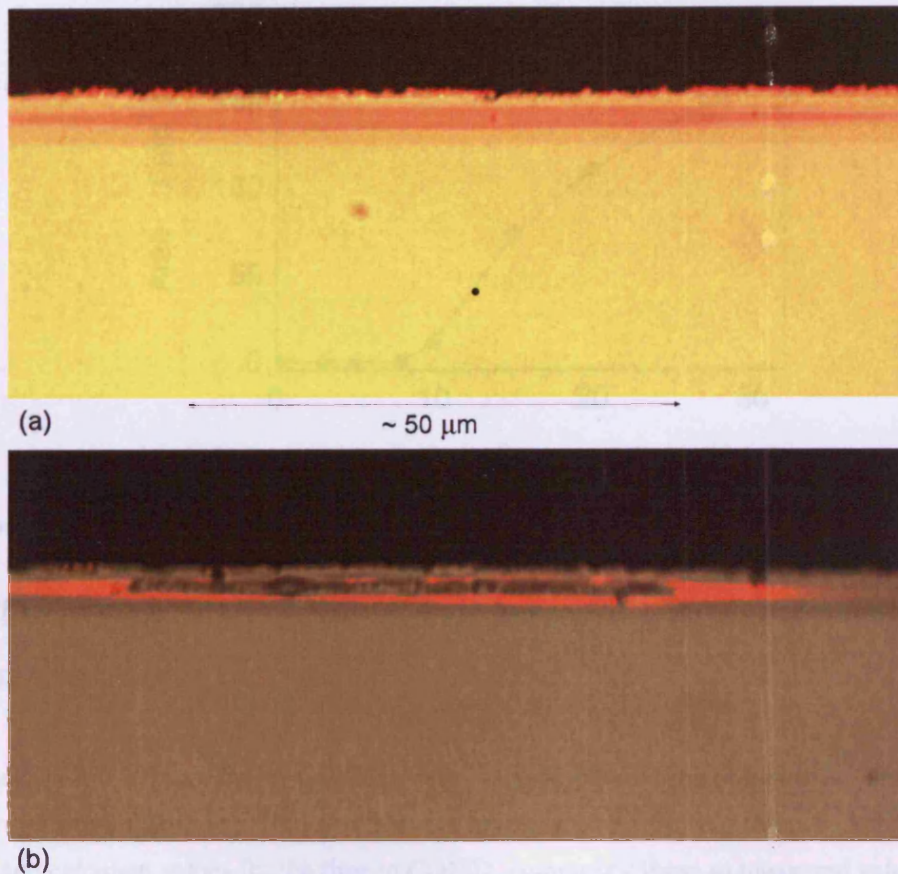


FIGURE 5.4: Optical micrographs (to the same scale) of the central, pumped sections of a facet under the stripe. The active region is at the top of this p-side up mounted device and is shown emitting red electroluminescence. The condition of the facet is shown in two ways: the facet is illuminated with white light and red electroluminescence is produced by low level current pulses. (a) A pristine facet characterised by uniform appearance and electroluminescence. (b) Facet damage was clearly visible in this device after a $1 \mu\text{s}$, 15 A current pulse. Electroluminescence is seen in the area surrounding the damage, which is the darkened, non-radiative area in the centre of the active region

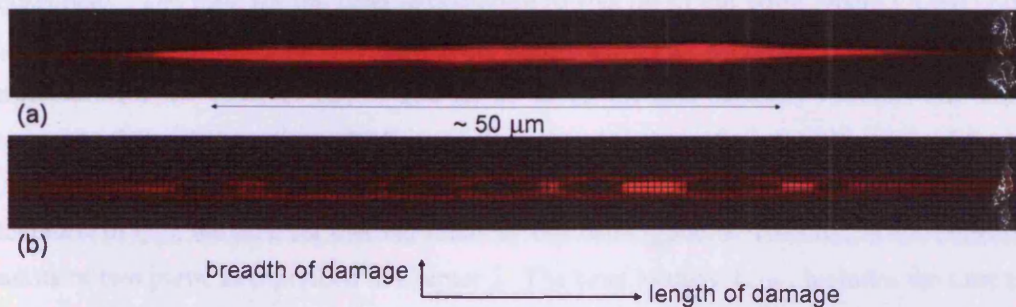


FIGURE 5.5: (a) Image of the nearfield emission from the facet of a device before aging with a 30 A, 1000 ns current pulse (b) Image of the same device after application of the pulse. The damage can be seen as the dark regions surrounded by electroluminescence. I brightened the image using software because of the low remaining light levels. The superimposed grid enabled measurement of facet area damaged at COMD. The facet was not illuminated by the microscope and cannot be seen

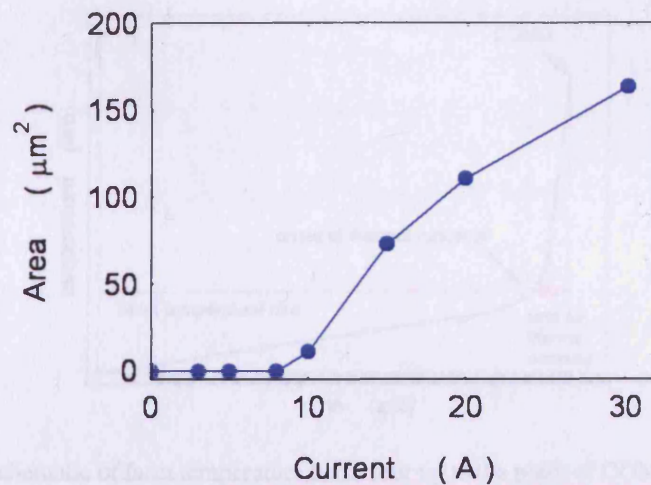


FIGURE 5.6: Measured area of damage on facet

5.4 Time to COMD: explanation in terms of a straightforward thermal model

In this section I will compare the COMD process to a simple melting point curve. I will use the energy arguments from the melting point curve to explain the limiting time to COMD at high powers and calculate values for the time to COMD, comparing these to measured values.

5.4.1 The COMD process

The total COMD process, as previously described in Chapter 2, consists of an initial facet temperature rise, followed by thermal runaway, facet melting, propagation of melt front leading to dark lines and drop of lasing power and takes place on a timescale of the order of hundreds of nanoseconds. The time for the facet temperature to rise up to the point where COMD occurs, t_{rise} is dominated by the relatively slow facet temperature rise up to the relatively low critical temperature (of the order of 100 or 200 K) at which thermal runaway occurs. The time for runaway to the melting point, which is much higher (of the order of 1500 K) is of the order of nanoseconds, and negligible in comparison [12, 18]. (Figure 5.7). For this reason, in the calculation of t_{rise} , the time for thermal runaway has been ignored. Thus t_{rise} is not uniform but consists of two parts, as described in chapter 2. The time to melt, t_{melt} , includes the time taken for facet damage and propagation of molten regions, until so much damage has occurred in the active region that further lasing is prevented.

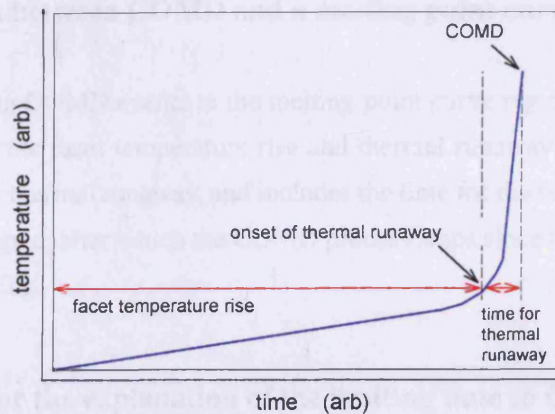


FIGURE 5.7: Schematic of facet temperature behaviour up to the point of COMD (not to scale). There is an initial slow facet temperature rise, which takes most of the time to COMD, followed by a very short (1 or 2 ns) thermal runaway

5.4.2 Melting point curve

In a simple melting point curve such as is used to determine the melting point of a substance, shown schematically in figure 5.8 (left), the temperature (T) of the material rises through ΔT until melting starts, absorbing a quantity of heat $mc\Delta T$ (mass \times specific heat \times temperature rise), remains constant while material melts, absorbing heat mL (mass \times latent heat of fusion), and then continues to rise. I will now compare COMD with such a curve, although there are differences between the two situations, as I will describe. The detailed form of the temperature rise is more complex than shown here, for example, but does not affect the arguments that follow.

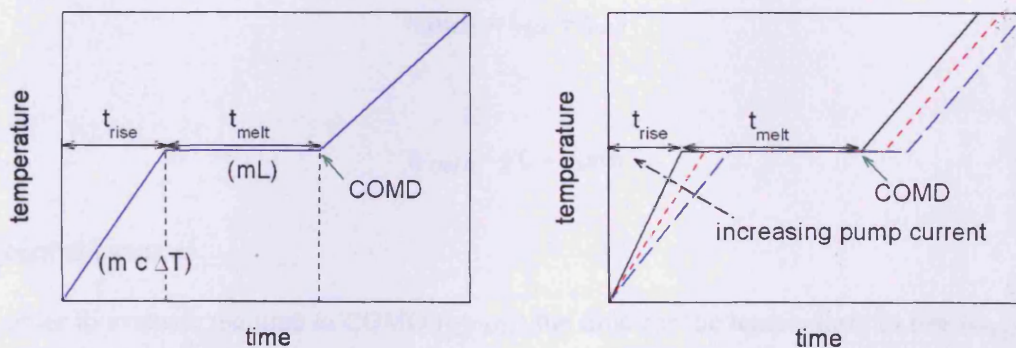


FIGURE 5.8: Schematic melting point curve showing an initial temperature rise to the melting point (ΔT) in time t_{rise} , with heat absorbed $mc\Delta T$, a portion at constant temperature for a time t_{melt} , with heat absorbed mL , followed by some further temperature rise. The thermal arguments do not depend on the detailed form of the temperature rise, which is complex, and has not been shown here. (b) As current increases t_{rise} shortens but t_{melt} remains constant. Thus t_{COMD} approaches a limiting value

5.4.3 Comparison between COMD and a melting point curve

I attribute the following COMD events to the melting point curve regions: the temperature rise region (t_{rise}) includes the facet temperature rise and thermal runaway. The flat portion, t_{melt} , begins at the end of the thermal runaway, and includes the time for the facet damage to occur and the melt front to propagate, after which the COMD process stops since there no longer sufficient intensity to cause melting.

5.4.4 The model for the explanation of the limiting time to COMD

In this section I will explain the finite limit of the time to COMD as follows. The total time to COMD (t_{COMD}) is the sum of the time for the temperature to rise (t_{rise}) and the time to melt (t_{melt}). The initial rate of facet temperature rise is proportional to the optical power, giving t_{rise} approximately inversely proportional to current and tending to zero at high currents.

Both t_{melt} and the absorbed optical energy required for melting are proportional to the mass of melted material. The mass melted and energy required both increase with current, and would tend to increase t_{melt} , but the power available for absorption also rises, which tends to decrease t_{melt} . These effects cancel over the current range used, leading to a constant t_{melt} . (Figure 5.8 (right)). Thus as current increases the total time, t_{COMD} , tends to a constant value.

In summary:

$$t_{COMD} = t_{rise} + t_{melt} \quad (5.1)$$

$$t_{COMD} \rightarrow 0 + const \quad (5.2)$$

as current increases.

In order to evaluate the time to COMD (t_{COMD}) the time for the temperature to rise (t_{rise}) and the time for the facet to melt and defect regions to form in the interior of the device (t_{melt}) must be determined.

5.4.5 Calculation of time to COMD and comparison of calculated and measured values

The initial nearfield distribution across the facet, at low currents and short times, is uniform (Figure 5.4(a)) leading to a uniform temperature rise. As current or time, and hence temperature

increase, the degree of filamentation of the laser beam will increase, leading to hotspots on the facet, at which COMD can occur. Thus the mass of material to be considered during the initial temperature rise, m_{rise} , is different to the mass which undergoes thermal runaway and melting, m_{melt} .

I assumed an average volume of $50 \mu\text{m}^3$ to obtain the mass, m_{rise} , of heated facet material. (The width of the stripe and a typical breadth of nearfield region and identical depth.) The energy required to increase the temperature of this facet material can be written as

$$P_{opt}t_{rise} = m_{rise}c\Delta T \quad (5.3)$$

where the specific heat and material density were obtained from linear interpolation of values for the binaries from the literature, which are given in Table 5.1. P_{opt} is the absorbed optical power, taken to be a fraction of the total beam power. I measured the total beam power for a large number of devices, operated pulsed at low duty cycle to avoid bulk sample heating, up to COMD, and found very consistent P-I characteristic between devices. To obtain an estimate of the beam power at the high currents used here I extrapolated the low power characteristics up to the high currents used here. (Ideally an estimate of thermal rollover would be included.)

The major contribution to t_{rise} is the time taken for the facet temperature to rise to the start of thermal runaway, which occurs at a much lower temperature than the actual melting point. I used a value for the temperature rise, ΔT , of 200 K, based on the measurement, documented in the literature, of a critical facet temperature at which thermal runaway commences, measured using the Raman effect [18]. In this work Raman probe beam was focussed to a diameter $1.5 \mu\text{m}$, over which an average temperature rise of 120 - 140 K was measured, the peak temperature being higher. Henry et alia [12] calculated the fraction of power absorbed at thermal runaway to be two thirds, with an absorption coefficient of $2 \times 10^4 \text{ cm}^{-1}$. The measured absorption coefficient was 140 cm^{-1} at room temperature. Taking the ratio of the absorption coefficients and scaling the absorbed power linearly gives an absorbed power of 0.5%. Thus taking the facet temperature rise, ΔT , as 200 K, and assuming 0.5% of the optical power (P_{opt}) is absorbed I obtained values for t_{rise} . These are plotted in Figure 5.9 as a function of the magnitude of the current pulse.

In order to obtain t_{melt} I needed to know the melted volume as a function of current. I measured the areas of facet damage for each device after the current pulse was applied, which showed a clear increase with current (Figure 5.6). I took the molten volume to be proportional to the measured area of damage raised to 3/2 power (ie scaled dimensionally from area to volume). I discuss this choice in section 5.5. Even so, I found that provided the molten volume increased with current (regardless of the exact relationship), I obtained a limiting, approximately constant, total time for t_{COMD} over the current range used. Having obtained values for the melted volume and mass, m_{melt} , I calculated t_{melt} as follows:

The energy required to obtain melting of the material is given by

$$P_{opt}t_{melt} = m_{melt}L \quad (5.4)$$

where the latent heat of fusion was obtained from linear interpolation of values for the binaries from the literature, given in Table 5.1.

Finally t_{rise} and t_{melt} were added to give the total time to COMD. (Figure 5.9).

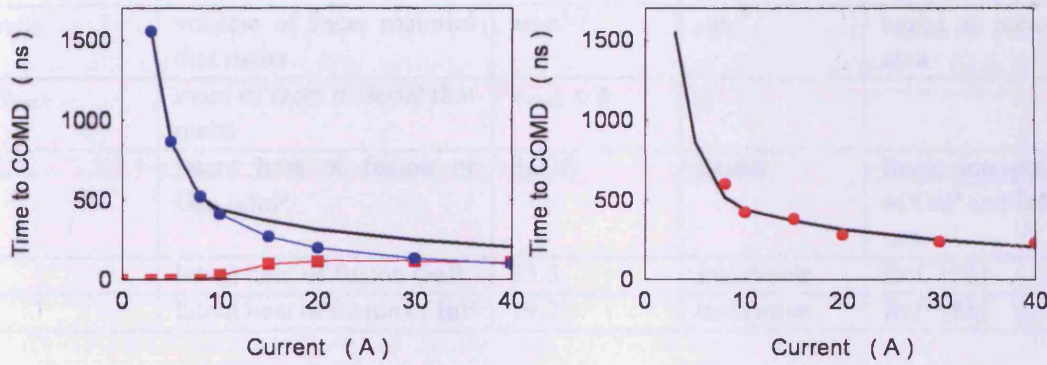


FIGURE 5.9: Left: calculated time for temperature of the facet to rise to thermal runaway (blue circles) and time for the quantity of damaged material, based on measured areas of facet damage, to melt (red squares). The total time to COMD, the sum of these, is shown by the black line. Right: measured time to COMD for the devices as a function of pulse current (red points). This time approaches a constant, limiting value of about 200 ns, asymptotically, as current increases, compared with the calculated total time to COMD (black line) obtained using the thermal model

5.5 Discussion of results and wider applicability

I have presented a simple model which quantitatively relates t_{COMD} , the observed time to COMD, to the measured area of facet damage and explains the limiting time of 200 ns at high powers. The model gives a reasonable result independently of the exact form of the assumptions made. Of the two components that comprise t_{COMD} , t_{rise} will always decrease as current and power increase and, provided the amount of facet damage increases with power, t_{melt} will remain approximately constant, thus resulting in a non-zero time to COMD at these high powers. Various factors have affected the choice of values used in the model and could affect the value of the limiting time obtained and will be discussed in this section.

The value of using single pulses (an existing technique [19]) as opposed to continuing repeated pulses, together with the adaptation to measure light levels (newly introduced as part of the work for this thesis) is clear, having increased the time resolution and reduced the amount of damage that occurs after the initial COMD at the facet, in order to move closer to the ideal of separating

Quantity	Description	Value	Unit	Note
m_{rise}	mass of facet material raised to temperature of thermal runaway	$v_{rise} \times \rho$	g	$v_{rise} = 50 \mu\text{m}^3$ ($\text{Al}_{0.5}\text{GaInP}$)
c	specific heat capacity for lattice matched $\text{Al}_{0.5}\text{GaInP}$	0.421	J/(gK)	linear interpolation from binaries [82]
ΔT	facet temperature rise to start of thermal runaway	200	K	
ρ	density of lattice matched $\text{Al}_{0.5}\text{GaInP}$	4.018	g/cm^3	linear interpolation from binaries [82]
v_{melt}	volume of facet material that melts	$\text{area}^{3/2}$	μm^3	based on measured area
m_{melt}	mass of facet material that melts	$v_{melt} \times \rho$	g	
L	latent heat of fusion of $\text{Ga}_{0.48}\text{InP}$	3.276	kJ/cm^3	linear interpolation of GaP and InP values
	latent heat of fusion GaP	23.3	kcal/mole	Ref. [83]
	latent heat of fusion of InP	19.7	kcal/mole	Ref. [83]

TABLE 5.1: Values of data used in calculating the time to COMD

the effects of damage by light from the subsequent effects of damage by generation of heat or the continued passage of electrical current.

5.5.1 The COMD process

The exact process a facet undergoes during catastrophic optical damage is more complex than simple melting. For the purposes of the numerical calculation melting has been assumed, as is generally accepted in the literature of COMD.

5.5.2 The thermal model

The form and the values of the calculated time to COMD, t_{COMD} , agree well with measured values as plotted in Figure 5.9, although there are uncertainties, which I will now discuss, in some of the parameters used.

5.5.2.1 Estimate of volume

There were several possible ways to obtain an estimate of the volume. The first two of these depend on the measured area of facet damage. One possibility was to assume the melted region

travelled as far into the interior of the device as it did across the active region, as would happen if the melting occurred because of conduction of heat. If the area of facet damage was $l \times b$ on the facet, with l being the distance under the stripe and b being the distance across the layers from the active region, the melted volume would be $l \times b \times b$. (Figure 5.10)

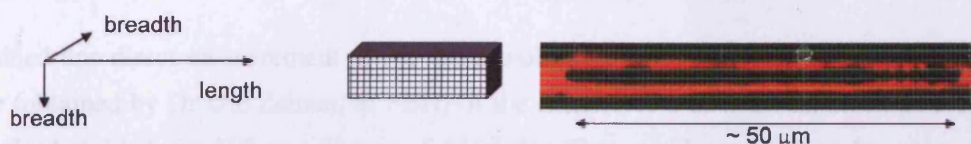


FIGURE 5.10: Estimation of volume of damage from facet area using $lxbxb$ method. The calibrated grid enabled the damaged facet area or areas to be estimated as approximately rectangular areas (lxb). The depth was taken as b also, as indicated by the arrows, giving a volume $lxbxb$

The method I used consisted of taking the molten volume to be proportional to the measured area of damage raised to $3/2$ power (scaled dimensionally from area to volume), and is more appropriate if the propagation of the molten area back from the facet increases by a different mechanism to the increase of area on the facet itself, which is likely to be the case. For example the area of damage on the facet might increase by conduction of heat from the hotspots where the COMD was seeded and the area of damage in the interior of the device by reabsorption of laser radiation. I will now compare these two methods mathematically.

If the smallest dimension, the breadth, is taken to be r , the length across the facet, ar and the depth into the device br , where a and b are constants, the volume is abr^3 (using the conventions of figure 5.11 for length, breadth and depth.) The facet damage area is ar^2 . Scaling this dimensionally gives $(ar^2)^{3/2} = a^{3/2}r^3$, whereas the actual volume is abr^3 . This still does not give the correct relationship between area and volume, since ab is being estimated by $a^{3/2}$, but is a better estimate than $area=ar^3$, which is obtained from $lxbxb$, which assumes effectively a linear configuration of damage.

Another way of obtaining the volume of damage depends on the generation of dark line defects. It is found that the damage to the interior of the device, after facet damage, is caused by the region next to the hot, melted material being raised in temperature and hence absorption coefficient, absorbing light and melting. In this way a molten region progresses through the interior of device, along the active region. When resolidified this region is highly defective and non-radiative and can be seen in specially prepared samples as a dark line in the scattered electroluminescence from the active region, which may split into several branches [32], or by cathodoluminescence (CL) [84]. Measurements of the speed of propagation (which varies with distance along the cavity and time through the pulse) of these lines vary from $1 - 5 \text{ ms}^{-1}$ [19], to 20 ms^{-1} [34]. Thus the number and speed of the dark lines, and hence the damaged volume, cannot be predicted from the measured area of damaged facet. The device would stop lasing

when so much of the active region volume had been damaged that threshold could no longer be reached. The time to COMD measurements from the light pulses would include the time for the facet temperature to rise, the time for the initial facet melting and the time for propagation of the dark line. Thus the time of propagation of the dark line and hence damage volume could not be unambiguously determined.

I obtained one direct measurement of the actual volume using detailed measurements of a CL image (obtained by Dr Ute Zeimer, at FBH) of the interior of a device I mounted p-side down and pulsed at 12 A for 500 ns. (Figure 5.11(top)). This could not be done for every device as the techniques, sample preparation and imaging facilities required are highly specialised. Figure 5.11(bottom, left) shows a microscope image of the facet of the device. The COMD can be clearly seen. This device was prepared for CL by etching away the substrate and n-cladding layers. The dark line defect caused by the molten region propagating back into the device can be seen as the black regions.

Since the pulse length was 500 ns a speed of propagation could be estimated, but this was either different at each position along the facet, or the propagation started at a different time, since the dark line defects have travelled different distances. From this image I measured values of speed ranging from 3.5 to 8.8 ms⁻¹ (± 0.8 ms⁻¹), in agreement with values in the literature, but causing large uncertainties in estimated volume. I therefore determined the damaged volume directly, superimposing calibrated grids on the facet and CL images, measuring the area of damage in the CL image and multiplying this by the average breadth of the damage across the active region. Figure 5.12 shows both estimates obtained from the facet area (lxbxb: lower line and area raised to three halves power: upper line). The direct measurement at a single current for this device gave a value of 136 (± 19.5) μm^3 at a pulse length of 500 ns. Assuming the propagation velocity was constant over a change of pulse length from 500 ns to 1000 ns, I doubled the value of volume obtained giving a value of 271 (± 39) μm^3 (black triangle), for comparison with the 1000 ns devices. The error bar on this value was the size of the symbol. It can be seen that the final value for the measured volume (scaled for the correct pulse length) lies on the curve of damaged volume as a function of current used in the numerical estimate of the time to COMD.

In summary, I have measured the time to COMD and the area of facet damage as a function of current. To explain these I have made arguments based on the amounts of energy required to produce the damage and the time taken to absorb these as a function of optical power. The link between the time to COMD and the area of facet damage is the volume of damage, estimated by a method which is confirmed by the cathodoluminescence measurement.

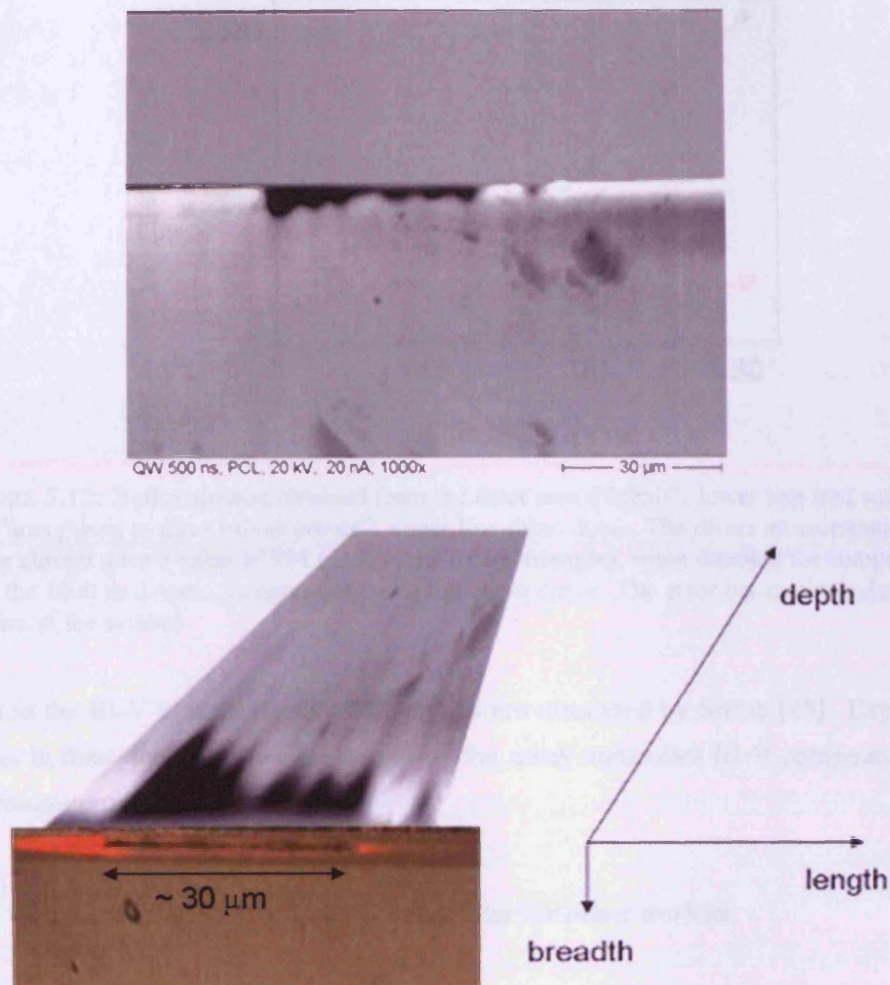


FIGURE 5.11: Top: cathodoluminescence (CL) image of the plane of the active region of a p-side down mounted QW device (single pulsed at 12 A for 500 ns), after the n-type layers had been etched away. Bottom: Microscope image of facet damage to the same device with a manipulated version of the CL image (no longer to scale) to show the orientation of the two images with respect to one another. (The terminology used for measuring distances to get volume is also shown)

5.5.2.2 Values of specific heat and latent heat

Values for quantities such as the specific heat capacity used in the calculation of the facet temperature rise, the latent heat of fusion for the thermal model, and other values such as material density, required for conversion of units, were obtained from the literature, given in Table 5.1. In some cases no measured values exist (for example the latent heat of fusion of GaInP) and linear interpolations of measured values for binaries have been used. There are few measurements for specific heats of III-V ternary and quaternary compounds as a function of composition. Measurements of specific heat exist for $\text{InP}_x\text{As}_{1-x}$ and $(\text{GaAs})_x(\text{InP})_{1-x}$ [82], for which linear interpolation is a good approximation. The specific heat and material density were obtained from linear interpolation of values for the binaries from the literature, given in Table 5.1. Heats

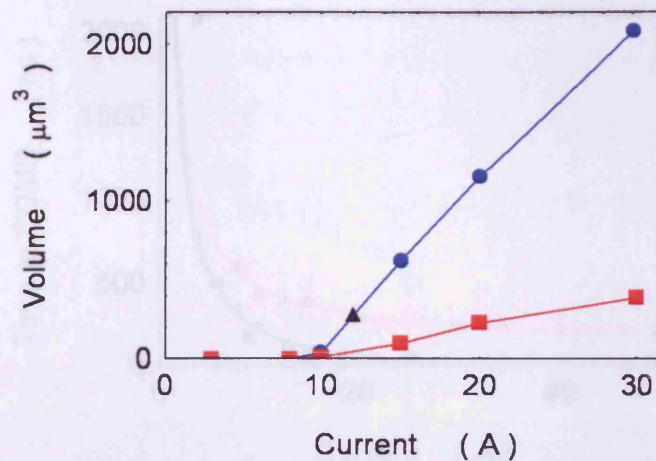


FIGURE 5.12: Both estimates obtained from the facet area (“ $l \times b \times h$ ”: lower line (red squares) and “area raised to three halves power”: upper line (blue dots). The direct measurement at a single current gave a value of $271 (\pm 39) \mu\text{m}^3$ (black triangle), when doubled for comparison with the 1000 ns devices, in agreement with the upper curve. The error bar on this value was the size of the symbol

of fusion in the III-V semiconducting compounds are discussed by Sirota [83]. Experimental difficulties in their determination are caused by the many anomalies III-V compounds exhibit and few measurements exist.

5.5.2.3 Comparison of time to COMD behaviour for other devices

Figure 5.13 shows the results of measuring the time to COMD for different types of device. The QW devices showed large amounts of facet damage and a time to failure that remained high at high currents and powers. The QD devices, in contrast, showed a time that tended to zero at high powers, as did a set of commercial QW devices with passivated and coated facets. These two sets of devices showed comparatively little area of damaged facet, thus strengthening the link between facet damage and the time to COMD.

5.5.3 Wider applicability: other device dimensions, material systems

The measurements were performed on a set of 1 mm long devices with $50 \mu\text{m}$ stripes from the AlGaInP material system. The continued ability of the device to lase depends on there being enough gain producing medium left after damage to achieve threshold, which will be dependent on device length. A broad area device will be less sensitive to a given volume of destroyed active region material. The AlGaInP material system has low values of thermal conductivity which will be likely to have a strong influence on temperature rise. However, the values obtained for the limiting time to COMD would be expected to be similar in lasers fabricated from material systems such as GaAs, with similar values of latent heats of fusion and density.

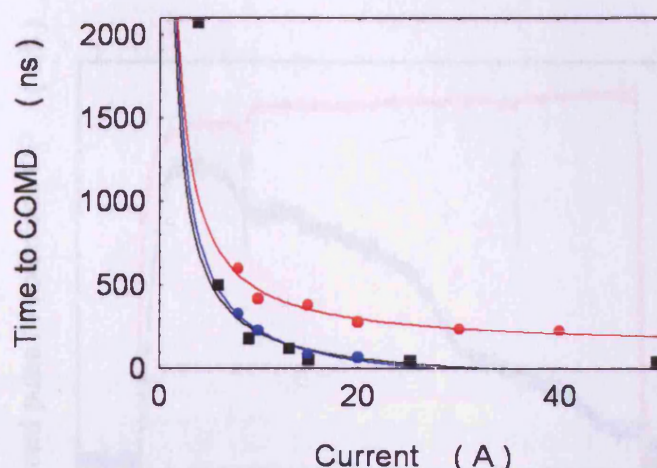


FIGURE 5.13: The time to COMD for three types of device: the unprotected QW devices used in this chapter (red points) the QD devices used in other parts of this work (blue points) and fully passivated and coated commercial QW devices (black points: data provided by Dr J. W. Tomm). The unprotected QW devices showed large amounts of facet damage and a finite time to COMD

5.5.4 Increase of time resolution

The increase in time resolution afforded by the adaptations to the standard Berlin setup, from 7 μ s, at which a time to COMD of 100-200 ns was inferred [19], to tens of nanoseconds enabled this time to be confirmed. In addition, in many of the current traces kinks followed closely after the drop in light power. Such kinks have previously been suggested as a possible signal to instigate a damage limitation process [34], by using circuitry that cuts the power supply to the laser diode at the time at which the kink occurs, preventing damage. From the nanosecond timescale of these measurements I was able to observe that the kink in the current trace followed *after* the drop in light level. (Figure 5.14). Turning off the current at this point would not prevent the initial COMD, but would prevent further propagation of the dark line defect and prolong the life of the laser. These results indicate the timescale on which this must be achieved to obtain the maximum possible extension of laser life. In some traces there appeared to be more than one drop in the light level, which was often followed by a second current kink.

5.6 Summary and conclusions

To summarise, I have observed the light intensity during COMD on the timescale of tens of nanoseconds using single, high current pulses applied to red emitting AlGaInP QW based laser diodes. Using as-cleaved facets and this material system, which is susceptible to COMD, I was able to clearly observe and investigate the damage to the facet. I discovered that in the current range up to 40 A, the total COMD process up to the drop of light intensity to non-lasing levels

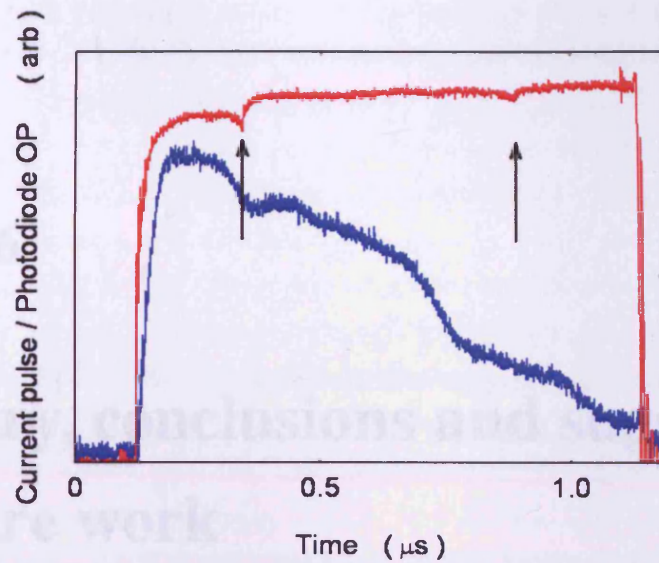


FIGURE 5.14: Traces for photodiode output (lower, blue trace) and current (upper, red trace) for a device pulsed at 8 A. The kinks in the current traces (marked with arrows) always occurred after a drop in light level

5.1 Summary of main conclusions

takes place on a timescale of hundreds of nanoseconds, approaching a limiting value of 200 ns, and that there was a clear relationship between the measured area of facet damage and the drive current. Using a straightforward thermal model I proposed an explanation the limiting time at high currents and the relationship between the time to COMD and the area of damaged facet material.

The main experimental design aimed at reducing the thermal conductivity of the beam to a value that gives an optimal beam quality and at the same time allowing for easy access and optical inspection of the undulator. Both these objectives were achieved by using a special geometry for the undulator poles, which allowed for a large range of pole shapes. I proposed a special design for the undulator poles, which allowed for a large range of pole shapes. This was achieved by using a special geometry for the undulator poles, which allowed for a large range of pole shapes. This was achieved by using a special geometry for the undulator poles, which allowed for a large range of pole shapes.

Facet damage occurs at a rate that is high for high power devices, with local increases along specific regions of the undulator. The main reason for this is the high power density at the facet of COMD because of the lower filamentation, the higher filamentation velocity and the use of interacting or absorbing material with the beam. A higher COMD

Chapter 6

Summary, conclusions and suggestions for future work

6.1 Summary of main conclusions

Improving the power available from low cost, light and portable semiconductor laser diodes still presents challenges, among them improving the efficiency of coupling the beam into applications, and reducing the likelihood of catastrophic optical damage.

The mode expanded design offers a means of reducing the vertical divergence of the beam to a value that gives an output beam much closer to circular, by adding only two extra layers, and without increasing the threshold current, both disadvantages of some other reduced farfield designs. I measured a threshold current density of 0.9 kA/cm^2 compared to 1.49 A/cm^2 for a standard structure, both designed for medium power optical storage applications with a farfield of 18° . This was achieved by use of a waveguide that simultaneously maintained a high intensity at the quantum wells and increased the width of the optical mode inside the cavity, narrowing the farfield. Wafers were grown with farfield divergences of 18° and 13° . Consistency of performance over successive growths is important in a commercial design and modelling of variability suggested the design could be reproducible within standard manufacturing tolerances, and measurements of repeated growths over a period of a year confirmed this.

Catastrophic mirror damage remains an issue for high power devices, with facet treatments adding expense to manufacturing a finished product. Quantum dot based devices have promised a range of potential advantages over quantum well based devices, including an increased power density at the facet at COMD because of the lower filamentation, lower surface recombination velocity and reduced area of intersection of absorbing material with the beam. A higher COMD

power density limit has been demonstrated in 900 nm band emitting devices and my measurements showed, for the first time in red/NIR emitting (Al)GaInP based devices, that the measured power density at failure is higher in QD based devices at 17 MW/cm^2 for short pulse lengths compared to 14 MW/cm^2 for QW structures, even when comparing research QD wafers, still under development, with high quality commercially manufactured quantum well based wafers. Careful investigation of the nature of the damage revealed that the QD devices had not only surpassed the performance of the QW devices, but had not yet reached catastrophic *mirror* damage levels and were degrading by a different process, involving the interior of the active region, that had the potential for improvement as the growth of these experimental structures was refined and improved. These differences, suggested by facet temperature measurements, were confirmed by scanning electron microscopy, including cathodoluminescence of the active region, and photocurrent and laser beam induced current studies. The damage to QW devices followed the classic pattern, starting at the facet and propagating into the interior through the active region, whereas the damage to the QD devices occurred uniformly throughout the portion of the active region under the stripe, as a function of depth into the device. The spectroscopic information gained from PC and LBIC implicated Very Large Dots, identified in other work, in the degradation process and SEM images confirmed the presence of some very large, stacked dots within the structure.

The COMD process has not been previously observed in real time, with the time resolution of previous measurements being on the scale of microseconds. An adaptation of a technique using single, microsecond long, very high current pulses to monitor the facet with a fast photodiode, measuring the time taken for the output power to drop, revealed further differences in QD and QW based devices. The QW devices showed a time to COMD that decreased to a finite value of about 200 ns as operating power increased, concomitant with an increase in the area of damage measured on the facet, whereas the QD devices showed little facet damage and a time to catastrophic damage that tended to zero as the power increased. The classic COMD process involves a volume of material that melts and resolidifies, with a molten front propagating through the active region. The energy required to melt this material is absorbed from the optical mode within the cavity, and can be calculated if the volume of molten material and value of the latent heat are known, in a new approach. The areas of such large amounts of damage and such precise times have not previously been measured. A proportion only of the laser power is absorbed while the process continues, and this, together with the energy required to melt the material, gave a modelled value for the time to COMD that was consistent with the measured values, clearly associated the amount of damage with the time taken. The QD devices, in contrast, showed little facet damage and much shorter times.

6.2 Suggestions for future work

The time-resolved measurements and energy calculations, involving both latent heat of fusion and specific heat capacity during temperature rise, promise further insights into the nature of the classic COMD process, and indeed are already being extended to greater time resolution with further energy calculations. The COMD process in QW devices involves two spatial locations within the laser: the facet and the interior. In both of these energy is required to raise the temperature and also to melt the material, if that is what is taking place. It is known from work in growth that the group V element in a III-V compound shows a strong tendency to dissociate and evaporate, leaving a group III rich mixture behind. The melting point of this mixture would be far lower than the melting point of the original III-V material, which is an alloy of two III-V compounds (GaP and InP in this work). Studies of the temperature rise at the facet have not been carried out with sufficient precision and spatial and temporal resolution to determine the precise melting point of the facet material at the locations of the damage, as techniques are still being developed to achieve this. SEM of the facets after COMD showed unexplained structure. An EDSX examination of the facet of one of my damaged QW devices showed a decrease in the concentration of phosphorus, suggesting dissociation does occur (and also some concentrations of oxygen in certain regions of damage). Early work on the nature of the molten tracks showed a dissociation of the molten material in the interior of the active region. As well as the lack of previous energy calculations, there is scope for a full thermodynamic analysis of the COMD process, including the thermodynamic quantities associated with temperature rise, change of state, dissociation and disordering, with consideration of the combinations of III-V elements that are stable at the temperatures of the material during COMD, in other words, the phase diagram.

The work on COMD commenced many years ago and has been studied ever since. It is a field that is not only commercially extremely important but full of incredibly interesting physics and chemistry, with scope for much future work.

Bibliography

- [1] N. A. Pikhtin, S. O. Slipchenko, Z. N. Sokolova, A. L. Stankevich, D. A. Vinokurov, I. S. Tarasov and Zh. I. Alferov “16 W continuous-wave output power from 100 μm -aperture laser with quantum well asymmetric heterostructure” *Elec Lett* **40** (2004), 1413 – 1414
- [2] A. R. Kovsh, A. E. Zhukov, N. A. Maleev, S. S. Mikhrin, D. A. Livshits, Y. M. Shernyakova, M. V. Maximova, N. A. Pihtin, I. S. Tarasov, V. M. Ustinov, Z. Alferov, J. Wang, L. Weib, G. Lin, J. Chi, N. N. Ledentsov and D. Bimberg “High power lasers based on sub-monolayer InAsGaAs quantum dots and InGaAs quantum wells” *Microelectronics Journal* **34** (2003), 491–493
- [3] D. G. Deppe, K. Shavritranuruk, G. Ozgur, H. Chen and S. Freisem “Quantum dot laser diode with low threshold and low internal loss” *Elec Lett* **45** (2009), 54–55
- [4] M. Kanskar, T. Earles, T. J. Goodnough, E. Stiers, D. Botez and L. J. Mawst “73% CW power conversion efficiency at 50W from 970nm diode laser bars” *Elec Lett* **41** (2005), 245–246
- [5] B. Kohler, J. Biesenbach, T. Brand, M. Haag, S. Huke, A. Noeske, G. Seibold, M. Behringer and J. Luft “High-brightness high-power kW-system with tapered diode laser bars” *Proc SPIE* **5711** (2005), 73–84
- [6] P. M. Snowton and P. Blood “The differential efficiency of quantum-well lasers” *IEEE J Sel Top Q E* **3** (1997), 491–498
- [7] P. Ressel, G. Erbert, U. Zeimer, K. Hausler, G. Beister, B. Sumpf, A. Klehr and G. Trankle “Novel passivation process for the mirror facets of Al-free active-region high-power semiconductor diode lasers” *IEEE Phot Tech Lett* **17** (2005), 962–964
- [8] M. Gasser and E. E. Latta “Method for mirror passivation of semiconductor laser diodes” *US Patent* (1992), 5144634
- [9] J. H. Marsh “The role of monolithic integration in advanced laser products” *J Crystal Growth* **288** (2006), 2–6

- [10] F. Rinner, J. Rogg, M. T. Kelemen, M. Mikulla, G. Weimann, J. W. Tomm, E. Thamm and R. Poprawe “Facet temperature reduction by a current blocking layer at the front facets of high-power InGaAs/AlGaAs lasers” *J Appl Phys* **93** (2003), 1848–1850
- [11] M. Fukuda *Reliability and Degradation of Semiconductor Lasers and LEDs* (Artech House, 1991)
- [12] C. H. Henry, P. M. Petroff, R. A. Logan and F. R. Merritt “Catastrophic damage of $Al_xGa_{1-x}As$ double-heterostructure laser material” *J Appl Phys* **50** (1979), 3721–3732
- [13] M. B. Sanayeh, P. Brick, W. Schmid, B. Mayer, M. Mueller, M. Reufer, K. Streubel, S. Schwirzke-Schaaf, J. W. Tomm, A. Danilewsky and G. Bacher “Defect investigation and temperature analysis of high-power AlGaInP laser diodes during catastrophic optical damage” *J Mater Sci: Mater Electron* **19** (2008), S155–S159 12th International Conference on Defects-Recognition, Imaging and Physics in Semiconductors, Berlin, GERMANY, SEP 09-13, 2007
- [14] O. Ueda, K. Wakao, S. Komiya, A. Yamaguchi, S. Isozumi and I. Umebu “Catastrophic degradation of InGaAsP/InGaP double-heterostructure lasers grown on (001) GaAs substrates by liquid-phase epitaxy” *J Appl Phys* **58** (1985), 3996–4002
- [15] R. E. Mallard, R. Clayton, D. Mayer and L. Hobbs “Failure analysis of high power GaAs-based lasers using electron beam induced current analysis and transmission electron microscopy” *J Vac Sci Tech A* **16** (1998), 825–829
- [16] G. Chen and C. L. Tien “Facet heating of quantum well lasers” *J Appl Phys* **74** (1993), 4, 2167–2174
- [17] M. Ziegler, V. Talalaev, J. W. Tomm, T. Elsaesser, P. Ressel, B. Sumpf and G. Erbert “Surface recombination and facet heating in high-power diode lasers” *Appl Phys Lett* **92** (2008), 203506
- [18] W. C. Tang, H. J. Rosen, P. Vettiger and D. J. Webb “Raman microprobe study of the time development of AlGaAs single quantum well laser facet temperature on route to catastrophic breakdown” *App Phys Lett* **58** (1991), 6, 557–559
- [19] M. Ziegler, J. W. Tomm, D. Reeber, T. Elsaesser, U. Zeimer, H. E. Larsen, P. M. Petersen and P. E. Andersen “Catastrophic optical mirror damage in diode lasers monitored during single-pulse operation” *Appl Phys Lett* **94** (2009), 191101
- [20] H. S. Carslaw and J. C. Jaeger *Conduction of Heat in Solids* (Oxford University Press, 1959)
- [21] W. Nakwaski “Thermal analysis of the catastrophic mirror damage in laser diodes” *J Appl Phys* **57** (1985), 2424–2430

- [22] R. Schatz and C. G. Bethea “Steady state model for facet heating leading to thermal runaway in semiconductor lasers” *J Appl Phys* **76** (1994), 2509–2521
- [23] J. Mukherjee and J. G. McInerny “Electrothermal analysis of cw high-power broad-area laser diodes: a comparison between 2-D and 3-D modeling” *IEEE J Sel Top Q E* **13** (2007), 1180–1187
- [24] L. A. Coldren and S. W. Corzine *Diode lasers and photonic integrated circuits* page 148 (John Wiley & Sons, 1995)
- [25] J. W. Tomm, F. Rinner, E. Thamm, C. Ribbat, R. Sellin and D. Bimberg “Analysis of heat flows and their impact on the reliability of high-power diode lasers” *SPIE Proc* **4993** (2003), 91–99
- [26] S. N. G. Chu, S. Nakahara, M. E. Twigg, L. A. Koszi, E. J. Flynn, A. K. Chin, B. P. Segner and W. D. Johnston “Defect mechanisms in degradation of 1.3- μm wavelength channeled-substrate buried heterostructure lasers” *J Appl Phys* **63** (1988), 611–623
- [27] O. Ueda “Degradation of III-V opto-electronic devices” *J Electrochem Soc* **135** (1988), 11C–22C
- [28] S. J. Sweeney, L. J. Lyons, A. A. Adams and D. A. Lock “Direct measurement of facet temperature up to melting point and COD in high-power 980-nm semiconductor diode lasers” *IEEE J Sel Top Q E* **9** (2003), 1325–1332
- [29] S. N. Elliott, P. M. Smowton, G. T. Edwards, G. Berry and A. B. Krysa “Higher power density limit at COMD in GaInP/AlGaInP in quantum dots than in wells” *Proc SPIE* **7230** (2009), 7230–32
- [30] C. W. Snyder, J. W. Lee, R. Hull and R. A. Logan “Catastrophic degradation lines at the facet of InGaAsP/InP lasers investigated by transmission electron-microscopy” *Appl Phys Lett* **67** (1995), 488–490
- [31] K. H. Park, J. K. Lee, D. H. Jang, H. S. Cho, C. S. Park, K. E. Pyun, J. Y. Jeong, S. Nahm and J. Jeong “Characterization of catastrophic optical damage in Al-free InGaAs/InGaP 0.98 μm high-power lasers” *Appl Phys Lett* **73** (1998), 2567
- [32] M. B. Sanayeh, A. Jaeger, W. Schmid, S. Tautz, P. Brick, K. Streubel and G. Bacher “Investigation of dark line defects induced by catastrophic optical damage in broad-area AlGaInP laser diodes” *App Phys Lett* **89** (2006), 101111
- [33] B. W. Hakki and F. R. Nash “Catastrophic failure in GaAs double-heterostructure injection lasers” *J Appl Phys* **45** (1974), 3907–3912

- [34] J. H. Jacob, R. Petr, M. A. Jaspán, S. D. Swartz, M. T. Knapczyk, A. M. Flusberg, A. K. Chin and I. Smilanski "Fault protection of broad-area laser diodes" *Proc SPIE* **7198** (2009), 719815
- [35] A. Moser, E. E. Latta and D. J. Webb "Thermodynamics approach to catastrophic optical mirror damage of AlGaAs single quantum well lasers" *Appl Phys Lett* **55** (1989), 1152–1154
- [36] A. Moser "Thermodynamics of facet damage in cleaved AlGaAs lasers" *Appl Phys Lett* **59** (1991), 522–524
- [37] S. K. K. Lam, R. E. Mallard and D. T. Cassidy "Analytical model for saturable aging in semiconductor lasers" *J Appl Phys* **94** (2003), 1803–1809
- [38] Y. Ohba, M. Ishikawa, H. Sugawara, M. Yamamoto and T. Nakanisi "Growth of high-quality InGaAlP epilayers by MOCVD using methyl metalorganics and their application to visible semiconductor lasers" *J Crystal Growth* **77** (1986), 374–379
- [39] C. M. Wolfe, N. Holonyak and G. E. Stillman *Physical properties of semiconductors* (Prentice Hall, 1989)
- [40] S. Adachi "Lattice thermal conductivity of group-IV and III-V semiconductor alloys" *J Appl Phys* **102** (2007), 063502
- [41] H. Fujii, Y. Ueno and K. Endo "Effect of thermal resistivity on the catastrophic optical damage power density of AlGaInP laser diodes" *Appl Phys Lett* **62** (1993), 2114–2115
- [42] J. W. Tomm, T. Q. Tien, M. Ziegler, F. Weik, B. Sumpf, M. Zorn, U. Zeimer and G. Erbert "Degradation behaviour and thermal properties of red (650 nm) high-power diode single emitters and laser bars" *Proc SPIE* (2007), 645606
- [43] M. Ziegler, F. Weik, J. W. Tomm, T. Elsaesser, W. Nakwaski, R. P. Sarzala, D. Lorenzen, J. Meusel and A. Kozłowska "Transient thermal properties of high-power diode laser bars" *App Phys Lett* **89** (2006), 263506
- [44] W. Pittroff, G. Erbert, G. Beister, F. Bugge, A. Klein, A. Knauer, J. Maege, P. Ressel, J. Sebastian, R. Staske and G. Traenkle "Mounting of high power laser diodes on boron nitride heat sinks using an optimized Au/Sn metallurgy" *IEEE Trans Adv Packaging* **24** (2001), 434–441
- [45] S. W. Corzine, R. H. Yan and L. A. Coldren *Quantum well lasers* chapter 1 (Academic Press, 1993)
- [46] P. Blood, G. M. Lewis, P. M. Smowton, H. Summers, J. Thomson and J. Lutti "Characterization of semiconductor laser gain media by the segmented contact method" *IEEE J Sel Top Q E* **9** (2003), 1275–1282

- [47] C. G. V. de Walle “Band lineups and deformation potentials in the model-solid theory” *Phys Rev B* **39** (1989), 1871–1883
- [48] M. Moser, C. Geng, E. Lach, I. Queisser, F. Scholz, H. Schweizer and A. Dornen “Optical characterization of MOVPE grown GaInP layers” *J Crystal Growth* **124** (1992), 333–338
- [49] J. W. Tomm, A. Barwolff, U. Menzel, C. Lier, T. Elsaesser, F. X. Daiminger and S. Heinemann “Aging behavior of high-power laser arrays monitored by photocurrent spectroscopy” *Proc SPIE* **3004** (1997), 134–144
- [50] D. Pierscinska, A. Kozłowska, K. Pierscinski, M. Bugajski, J. W. Tomm, M. Ziegler and F. Weik “Thermal processes in high-power laser bars investigated by spatially resolved thermorefectance” *J Mater Sci: Mater Electron* **19** (2008), S150–S154 12th International Conference on Defects-Recognition, Imaging and Physics in Semiconductors, Berlin, GERMANY, SEP 09-13, 2007
- [51] S. L. Chuang *Physics of optoelectronic devices* (Wiley, 1995)
- [52] G. Berry *Doctoral Thesis* (Cardiff University: School of Physics and Astronomy, 1996)
- [53] A. Yariv and P. Yeh *Optical waves in crystals* (John Wiley & Sons, 1984)
- [54] M. Ziegler, J. W. Tomm, T. Elsaesser, C. Matthiesen, M. B. Sanayeh and P. Brick “Real-time thermal imaging of catastrophic optical damage in red-emitting high-power diode lasers” *Appl Phys Lett* **92** (2008), 103514
- [55] P. M. Snowton, G. M. Lewis, M. Yin, H. D. Summers, G. Berry and C. C. Button “650-nm lasers with narrow far-field divergence with integrated optical mode expansion layers” *IEEE J Sel Top Q E* **5** (1999), 735–739
- [56] S. Elliott, P. Snowton and G. Berry “Optimisation of high power AlGaInP laser diodes for optical storage applications” *IEE Proc-Optoelectron* **153** (2006), 321–325
- [57] P. M. Snowton and P. Blood *Optoelectronic Properties of Semiconductors and Superlattices, vol. 4 - Strained-Layer Quantum Wells and Their Applications* chapter 9: “Visible Emitting (AlGa)InP Laser Diodes”, pages 431–487 (Gordon and Breach, 1997)
- [58] Y. Kaneko and K. Kishino “Refractive indices measurement of $(\text{GaInP})_m/(\text{AlInP})_n$ quaternaries and GaInP/AlInP multiple quantum wells” *J Appl Phys* **76** (1994), 1809–1818
- [59] H. F. Lockwood, H. Kressel, H. S. Sommers and F. Z. Hawrylo “An efficient large optical cavity injection laser” *Appl Phys Lett* **17** (1970), 499–502
- [60] G. H. B. Thompson and P. A. Kirby “(GaAl)As lasers with a heterostructure for optical confinement and additional heterojunctions for extreme carrier confinement” *IEEE J Quantum Electron* **QE-9** (1973), 311–318

- [61] N. Lichtenstein, R. Winterhoff, F. Scholz, H. Schweizer, S. Weiss, M. Hutter and H. Reichl "The impact of LOC structures on 670-nm (Al)GaInP high-power lasers" *IEEE J Sel Topics Quantum Electron* **6** (2000), 564–570
- [62] P. M. Snowton, J. D. Thomson, M. Yin, S. V. Dewar, P. Blood, A. C. Bryce, J. H. Marsh, C. J. Hamilton and C. C. Button "Optical loss in large optical cavity 650nm lasers" *Semicond Sci Technol* **16** (2001), L72–L75
- [63] D. Botez "Design considerations and analytical approximations for high continuous-wave power, broad-waveguide diode lasers" *App Phys Lett* **74** (1999), 3102–3104
- [64] S. A. Moore, L. OFaolain, M. A. Cataluna, M. B. Flynn, M. V. Kotlyar and T. F. Krauss "Reduced surface sidewall recombination and diffusion in quantum-dot lasers" *IEEE Phot Tech Lett* **18** (2006), 1861–1863
- [65] P. M. Snowton, E. J. Pearce, H. C. Schneider, W. W. Chow and M. Hopkinson "Filamentation and linewidth enhancement factor in InGaAs quantum dot lasers" *Appl Phys Lett* **81** (2002), 3251–3253
- [66] C. Ribbat, R. L. Sellin, I. Kaiander, F. Hopfer, N. N. Ledentsov, D. Bimberg, A. R. Kovsh, V. M. Ustinov, A. E. Zhukov and M. V. Maximov "Complete suppression of filamentation and superior beam quality in quantum-dot lasers" *Appl Phys Lett* **82** (2003), 952–954
- [67] W. C. Tang, H. J. Rosen, P. Vettiger and D. J. Webb "Evidence for current-density-induced heating of AlGaAs single-quantum-well laser facets" *Appl Phys Lett* **59** (1991), 1005–1007
- [68] R. Beanland, A. M. Sanchez, D. Childs, K. M. Groom, H. Y. Liu, D. J. Mowbray and M. Hopkinson "Structural analysis of life tested 1.3 μm quantum dot lasers" *J Appl Phys* **103** (2008), 014913
- [69] W. Both, G. Erbert, A. Klehr, R. Rimpler, G. Stadermann and U. Zeimer "Catastrophic optical-damage in GaAlAs GaAs-laser diodes" *IEE Proc-J Optoelectron* **134** (1987), 95–103
- [70] J. D. Thomson, H. D. Summers, P. M. Snowton, E. Herrmann, P. Blood and M. Hopkinson "Temperature dependence of the lasing wavelength of InGaAs quantum dot lasers" *J Appl Phys* **90** (2001), 4859–61
- [71] V. Malyarchuk, J. W. Tomm, V. Talalaev, C. Lienau, F. Rinner and M. Baeumler "Nanoscopic measurements of surface recombination velocity and diffusion length in a semiconductor quantum well" *App Phys Lett* **81** (2002), 346–348
- [72] P. M. Snowton and P. Blood "Fermi level pinning and differential efficiency in GaInP quantum well laser diodes" *Appl Phys Lett* **70** (1997), 1073–1075

- [73] R. J. Cobley, K. S. Teng, M. R. Brown, S. P. Wilks and P. Rees “Direct real-time observation of catastrophic optical degradation in operating semiconductor lasers using scanning tunneling microscopy” *Appl Phys Lett* **91** (2007), 081119
- [74] G. S. Solomon, J. A. Trezza, A. F. Marshall and J. S. H. Jr. “Vertically aligned and electronically coupled growth induced InAs islands in GaAs” *Phys Rev Lett* **76** (1996), 952–955
- [75] P. M. Snowton, M. S. Al-Ghamdi, S. Shutts, G. Edwards, M. Hutchings and A. B. Krysa “Effect of growth temperature on InP QD lasers” *IEEE Phot Tech Lett* **22** (2010), 88–90
- [76] M. S. Al-Ghamdi, P. M. Snowton, S. Shutts, M. Hutchings, P. Blood and A. B. Krysa “InP/AlGaInP 730nm emission quantum dot lasers” 2009 Conference on Lasers and Electro-Optics and Quantum Electronics and Laser Science Conference (CLEO/QELS 2009) **1-5** (2009), 736–739
- [77] J. W. Tomm, A. Barwolff, A. C. Lier, T. Elsaesser, F. X. Daiminger and S. Heinemann “Laser based facet inspection system” *Proc SPIE* **3000** (1997), 90–98
- [78] M. Al-Ghamdi *Doctoral Thesis* (Cardiff University: School of Physics and Astronomy, 2010)
- [79] R. Sellin, C. Ribbat, D. Bimberg, F. Rinner, H. Konstanrer, M. Kelemen and M. Mikulla “High-reliability MOCVD-grown quantum dot laser” *Elec Lett* **38** (2002), 883–884
- [80] M. Ziegler, M. Hempel, H. E. Larsen, J. W. Tomm, P. E. Andersen, S. Clausen, S. N. Elliott and T. Elsaesser “Physical limits of semiconductor laser operation: A time-resolved analysis of catastrophic optical damage” *App Phys Lett* **97** (2010), 021110
- [81] D. R. Miftakhutdinov, I. V. Akimova, A. P. Bogatov, T. I. Gushchik, A. E. Drakin, N. V. D’yachkov, V. V. Popovichev and A. P. Nekrasov “Radiation parameters of ridge lasers at high pump currents” *QUANTUM ELECTRONICS* **38** (2008), 993–1000
- [82] S. Adachi *Properties of Semiconductor Alloys: Group-IV, III-V and II-VI Semiconductors* (John Wiley and Sons, 2009)
- [83] N. N. Sirota *Semiconductors and semimetals Vol 4* chapter Chapter 2 Heats of formation and temperature and heats of fusion of compounds $A^{III}B^V$ (Academic Press, 1968)
- [84] T. Q. Tien, F. Weik, J. W. Tomm, B. Sumpf, M. Zorn, U. Zeimer and G. Erbert “Thermal properties and degradation behavior of red-emitting high-power diode lasers” *Appl Phys Lett* **89** (2006), 181112

